# ABSTRACT


Title of Thesis: RUPTURE MECHANISMS OF PORCINE AND HUMAN ASCENDING AORTIC TISSUE UNDER DYNAMIC TRANSLATIONAL SHEAR DEFORMATION

Jason Harwerth, M.S. Mechanical Engineering, 2021

Directed By: Dr. Henry W. Haslach, Jr., Mechanical Engineering

Tissue Engineered Vascular Grafts (TEVGs) may be grown in living pigs to further their development towards use in humans to repair damaged aorta. To explore whether porcine grown TEVGs are good models for human grown TEVGs, normal human and porcine aortic tissues are loaded in shear deformation to compare the differences in the dissection response of these viscoelastic tissues. Shear is strongly related to aortic dissection. Translational constant rate and sinusoidal shear deformation tests characterize dynamic mechanical properties of aortic tissue. Knowledge of the tissue microstructure helps determine the effect of interstitial fluid-solid interaction on the shear response of the specimens. Transient and quasi-periodic response characteristics provide baseline material properties of normal porcine aortic tissue to compare its dissection resistance with TEVG porcine aortic tissue. The results show that normal porcine aortic tissue is sufficiently similar to human aortic tissue to justify the continued development of porcine grown TEVG models.


# RUPTURE MECHANISMS OF PORCINE AND HUMAN ASCENDING AORTIC TISSUE UNDER DYNAMIC TRANSLATIONAL SHEAR DEFORMATION

By

Jason Harwerth

Thesis submitted to the Faculty of the Graduate School of the
University of Maryland, College Park in partial fulfillment
of the requirements for the degree of
Masters of Science
2021

Advisory Committee:
Dr. Henry W. Haslach, Jr., Chair
Dr. Amr M. Baz
Dr. Eleanora Tubaldi

# Contents

# List of Tables

# List of Figures

# 1 Introduction

Aortic tissue is a complex material that researchers have attempted to model for decades, without success. Prediction of aortic dissection or rupture is particularly challenging and when dissection or rupture occurs, the results are often fatal. Degenerative aortic diseases, such as aortic aneurysm, greatly increase the risk of aortic dissection and rupture. The risk for aneurysm increases with age and the Centers for Disease Control and Prevention lists aortic aneurysm and dissection as the 15th leading cause of death in males aged 40-44 (Centers for Disease Control, 2015). In the worst-case scenario of rupture, mortality rates are estimated to be between 30-50% (Treska et al., 2006). Therefore, it is critical that the mechanisms of rupture are fully understood to be able to predict ruptures before they occur. Because the aorta is a hydrated, non-linear, viscoelastic, and anisotropic body, it has proven to be a challenge to accurately model and predict the mechanics of the aorta. Lacking a dependable model, clinicians attempt a repair if the diameter of the aneurysm exceeds 5.0 cm due to a correlation in aneurysm size and rupture (Powell et al., 2008). However, rupture can still occur in 0 to 23% of small aneurysms (<5.0 cm in diameter) (Phillippi et al., 2011) so using aneurysm diameter size as a deciding factor for operation is unreliable. Some have proposed that wall thickness may be a factor in rupture, but recent studies have found that there is no correlation between aneurysmal wall thickness and rupture pressure (Cavinato et al., 2019). Before an accurate predictive model can be made, a better understanding of the mechanics of rupture within the aortic wall must be developed to produce treatments that prevent rupture *in vivo*.

When a patient is determined to be at high risk of aneurysmal rupture, clinicians often graft a replacement material to replace the aneurysmal tissue. Rigid grafts are commonly made from synthetic polymers, such as Dacron, that have good

material properties but do not always have bio-compatibility with patients. Synthetic graft incompatibility can cause aneurysm formation (Bogaert et al., 2001), rupture (Ali et al., 2016), and thrombosis in smaller (<6 mm) arteries (Sarkar et al., 2007). However, recent developments in Tissue Engineered Vascular Grafts (TEVGs) have provided significant potential for improvement in scaffold materials that could allow the graft to grow, remodel, and repair in vivo (Pashneh-Tala et al., 2016). Currently, TEVGs are experimental and most trials are conducted on animals using various techniques for TEVG implementation. It is widely thought that of all the animal species, the porcine aorta is the most like human aorta (Lelovas et al., 2014). Because of this similarity, porcine grown grafts are used in experimental trials of TEVGs (Yeung et al., 2020). However, no studies have currently analyzed the dynamic and dissection-related properties of porcine aortic tissue. Consequently, it is vital to characterize any similarities between porcine and human aorta biomechanics related to rupture susceptibility to better understand whether TEVGs grown in pigs translates to success in human implantation. Because the main use for porcine tissue in medicine has traditionally been as a replacement heart valve (Sim et al., 2003), there has been limited biomechanical testing of the porcine arterial wall.

In typical biomechanical tests of human aortic specimens, the aortic tissue is loaded in the circumferential-longitudinal plane in either uniaxial or biaxial tension and material properties of the aorta are analyzed (e.g. Mattson and Zhang (2017)). While these tests can partially predict the response of the aorta wall to internal pressure, they primarily measure the response of collagen fibers in the aortic wall (Luo et al., 2016). Because aortic tissue is highly heterogeneous, more factors that impact crack initiation and propagation must be analyzed. Crack propagation within the arterial wall involves shearing mechanisms between medial layers (Haslach et al., 2011; Haslach et al., 2015; Haslach et al., 2018b). Using deformation controlled translational shear tests in the circumferential-longitudinal plane, the interaction between layers

in the media and their connections is measured. Specifically, characterization of the elastin network within the medial layer is sought because elastin degeneration is commonly found in aneurysmal tissue (Tang et al., 2005; Tong et al., 2013; Rabkin, 2015; Shen et al., 2019) which could indicate the critical role that elastin has in rupture mechanisms. Shear testing is used in place of tensile testing because collagen fiber dominates the response of the aortic wall in the tensile loading mode (Sommer et al., 2016), making it difficult to examine other microstructural components. With shear testing, the circumferentially-oriented collage fibers have little influence over the shear response of the arterial wall (Haslach et al., 2015; Sommer et al., 2016). In addition to contributions of the elastic network, most studies of arterial wall mechanics neglect any contributions due to interstitial fluid flow within the tissue. Proteoglycans, which bond water, have been found to accumulate near rupture and dissection sites in aneurysmal tissue (Humphrey, 2013; Shen et al., 2019). This accumulation, which may restrict fluid flow around the site, could indicate the importance of interstitial fluid-solid interaction in rupture mechanisms.

As it specifically relates to the porcine thoracic aorta, previous biomechanical studies focus on the tensile properties of the arterial wall (eg. Purslow (1983), White et al. (2014), Mattson and Zhang (2017), and Peña et al. (2019)). To date, the author is not aware of any studies analyzing the shear properties of the arterial wall for porcine aorta. The medial microstructure of the porcine aortic wall is structurally more organized than in humans and has not been observed to contain free floating deposits of protein units, such as proteoglycans, that appear in humans (Dingemans et al., 1981; Clark and Glagov, 1985; Dingemans et al., 2000). Tests in this thesis will focus on comparing the shear stress response of both human and porcine thoracic aorta. Characterization of the porcine arterial wall shear properties in comparison to the human arterial wall is critical for analysis of new TEVGs. In the future, an understanding of the shear properties of the porcine arterial wall and TEVGs is critical

to predict possible mechanical failures of the TEVG material.

Constant rate shear deformation tests measure the deformation rate dependence and the stress relaxation to prove viscoelasticity of aortic tissue specimens (Haslach et al., 2018a). Tests applying a cyclical sinusoidal shear deformation may allow the viscoelastic arterial wall to reach an approximately periodic shear response. By reaching a quasi-periodic response, a state of stress response comparable to the *in vivo* response is found and accurate analyses on the arterial wall can be performed. Previous work by Haslach et al. (2020) to investigate fluid-solid interaction properties found that the Interaction Ratio ($IR$), which is the ratio of the 1 Hz and 3 Hz Fourier decomposition amplitudes, is greater in magnitude for aneurysmal human aortic tissue compared to non-pathological human aortic tissue in the circumferential direction at 25% deformation. The same study found that the Roughness Ratio ($RR$), which is the ratio of the 1 Hz and 5 Hz Fourier decomposition amplitudes, is on average greater in magnitude for aneurysmal human aortic tissue compared to non-pathological human aortic tissue, although not statistically different. To build on this work, thoracic ascending aorta specimens obtained from human and porcine fresh tissue are used for comparative analysis. Shear tests in the circumferential and longitudinal directions estimate the influence of collagen fibers on the shear response.

To justify growing TEVGs in pigs, dynamic and dissection-related properties of porcine aortic tissue must be investigated to determine if the porcine aorta is similar enough to the human aorta to obtain relevant data from pig-grown TEVG trials. It is hypothesized that porcine aortic specimens exhibit dynamic shear properties that are similar to human aortic specimens. Similarity of specimen types is determined by several mechanical properties including the time response, resistance to shear, and fluid-solid interaction. To test this hypothesis, specimens are deformed at different deformation rates and magnitudes in the circumferential-longitudinal plane using both constant rate deformation and sinusoidal deformation tests.

# 2 Background

## 2.1 Aortic Wall Morphology

Distally from the heart, the aorta can be divided into four sections; the ascending aorta, the aortic arch, the descending thoracic aorta, and the abdominal aorta segments (Fig. 1a). From the beginning of the aortic valve, the diameter of the aorta tapers until its distal end at the aorta-iliac junction where the aorta splits into the abdominal iliac arteries. In this study, aortic specimens are taken exclusively from the ascending and descending thoracic aorta. Therefore, the morphological structure detailed in this section focuses on these regions.

### 2.1.1 Overall Structure

The aortic wall has three large scale layers: the tunica intima, the tunica media, and the tunica adventitia (Fig. 1b). The intima layer is the innermost layer

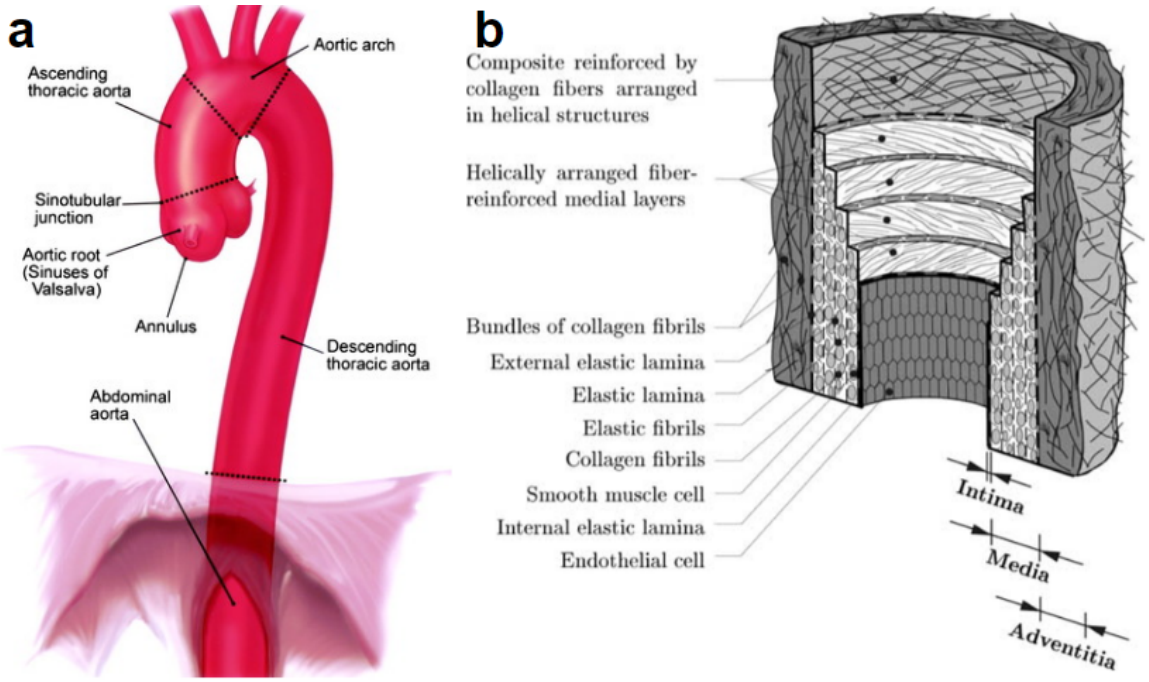


Figure 1: (a) Anatomy of the human thoracic and proximal abdominal aorta (Isselbacher, 2005). (b) Intimal, medial, and adventitial layers of a healthy elastic artery (Holzapfel et al., 2000)

of the aorta and it consists of a single layer of endothelial cells that are supported by an underlying basal lamina. The intima may also contain a subendothelial layer of connective tissue paired with axially oriented smooth muscle cells (Humphrey, 2002). An initial internal elastic lamina separates the media from the intima while allowing for the transport of water nutrients and electrolytes between the two layers. Water nutrients and electrolytes are then able to move through the medial layer. In the media, smooth muscle cells are embedded in an extracellular network of elastin and (type I, II, and V) collagen fibers with an aqueous ground substance matrix that contains proteoglycans and other matter (Humphrey, 2002). Collagen fibers in the media tend to be preferentially oriented in the circumferential direction (Wolinsky and Glagov, 1967). The human aorta has 40 to 70 concentric layers of smooth muscle cells oriented circumferentially that are five to fifteen micrometers thick (Humphrey, 2002). These layers are separated by thin fenestrated sheets of elastin which may act in a similar fashion as the initial internal elastic lamina. The final outer layer of elastin, known as the external elastic lamina, separates the media from the adventitia. The adventitia contains a dense network of type I collagen fibers, elastin fibers, nerves, fibroblasts, and the vasa vasorum network of fine blood vessels. The adventitial collagen fibers tend to be longitudinally oriented and are thought to act as a protective reinforcing sheath for the aorta, even though they only comprise approximately 10 percent of the total aortic cross-section (Humphrey, 2002). The nerves are thought to control the contraction of smooth muscle cells in the media by the diffusion of neurotransmitters. The fibroblasts are responsible for regulating the connective tissue and counteracting inflammation. The vasa vasorum both deliver nutrients and oxygen to the arterial wall and transport waste from the aorta (Ritman and Lerman, 2007).

### 2.1.2 Medial Microstructure of the Human and Porcine Aortic Wall

While observers agree on the general structure of the media, the exact microstructure of the media's layers of smooth muscle cells, elastin lamellae, and colla-

gen fibers is not fully understood. Studies that focus on examination of the medial microstructure often produce different results for different aortic variability's such as species type, specimen location, and the age of the patient. An early study by (Dingemans et al., 1981) used electron microscopy to discern differences between the thoracic porcine and human aortic medial microstructures. For porcine tissue, they observed an organization of circumferentially-oriented smooth muscle cells encompassed by a lamellar array of collagen fibers and elastin. Clark and Glagov (1985) later detected this structure in animals, including pigs, and deemed it the "musculo-elastic fascicle" (Fig. 2a). Dingemans et al. (1981) also discovered that most elastin present in the porcine aorta had well-defined structures and the elastin surfaces were closely associated with microfibrils.

The same study by Dingemans et al. (1981) did not find the same microstructure in the human aorta. Instead of the musculo-elastic fascicle, collagen fibers were found "at a distance" from smooth muscle cell surfaces while elastin was closely associated with the surface of smooth muscle cells. Elastin "streaks" were also found to be present in interlaminar spaces, contrary to the well-defined elastin structures of the porcine tissue. Furthermore, surfaces of the elastin in human tissue were often associated with deposits of flocculent material rather than microfibrils. In a sub-

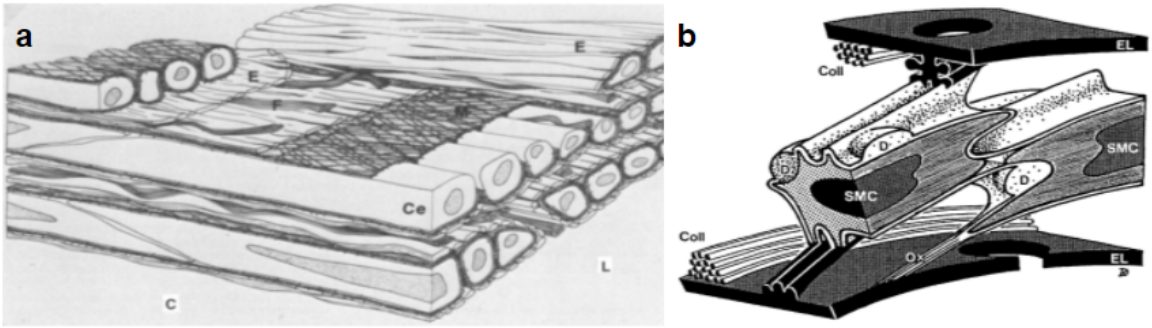


Figure 2: Proposed media structure in the aortic wall by: (a) Clark and Glagov (1985), (b) Dingemans et al. (2000). (a) Illustration of the "musculo-elastic fascicle" with smooth muscle cells encompassed by an array of elastic fibers found in porcine. (b) Illustration of the medial microstructural components and their arrangement in the human aorta.

sequent study of humans aged 45 to 74, Dingemans et al. (2000) found that these flocculent deposits contained thin basal lamina-like layers, type IV collagen, and proteoglycans. The basal lamina-like layers often connected adjacent smooth muscle cells and had an abundance of anti-fibronectin. Their study also confirmed their previous findings of the human microstructure (Fig. 2b). More descriptively, they found that collagen fibers were abundantly found close to the elastic lamellae in organized, circumferentially-oriented structures. Preferential localization of collagen fibers adjacent to the surfaces of smooth muscle cells was never found. In addition, they determined that the elastin streaks had considerable strength in their connection to the elastic laminae because they often remained intact in severely stretched specimens. They also noted that the shift from a well-defined structure to an unorganized structure likely shows the degenerative effects of aging in human aortic tissue.

It is of particular interest that the human medial lamellar unit has a more unorganized elastin arrangement, more proteoglycans, and collagen fiber more distant from smooth muscle cells as compared to the porcine medial lamellar unit. The important microstructural components that comprise the medial lamellar unit of both the porcine (Fig. 3a) and human (Fig. 3b) aortic walls are illustrated based on the previously referenced studies. These medial lamellar units correspond to generalized aged humans and 6 to 9 month old porcine, both of which are used in this study. The different microstructures offer a context in which to relate the medial lamellar unit structure to the experimentally observed mechanical response.

### 2.1.3 Aneurysmal Human Aortic Wall Medial Microstructure

Although this research focuses on comparisons between human and porcine aortic tissue, there have been many studies that focus on comparisons between aneurysmal and non-aneurysmal human aortic tissue. It is therefore useful to define the differences between the human aorta outlined in section 2.1.2 and aneurysmal aortic tissue because these studies will provide a framework for the analysis methods used

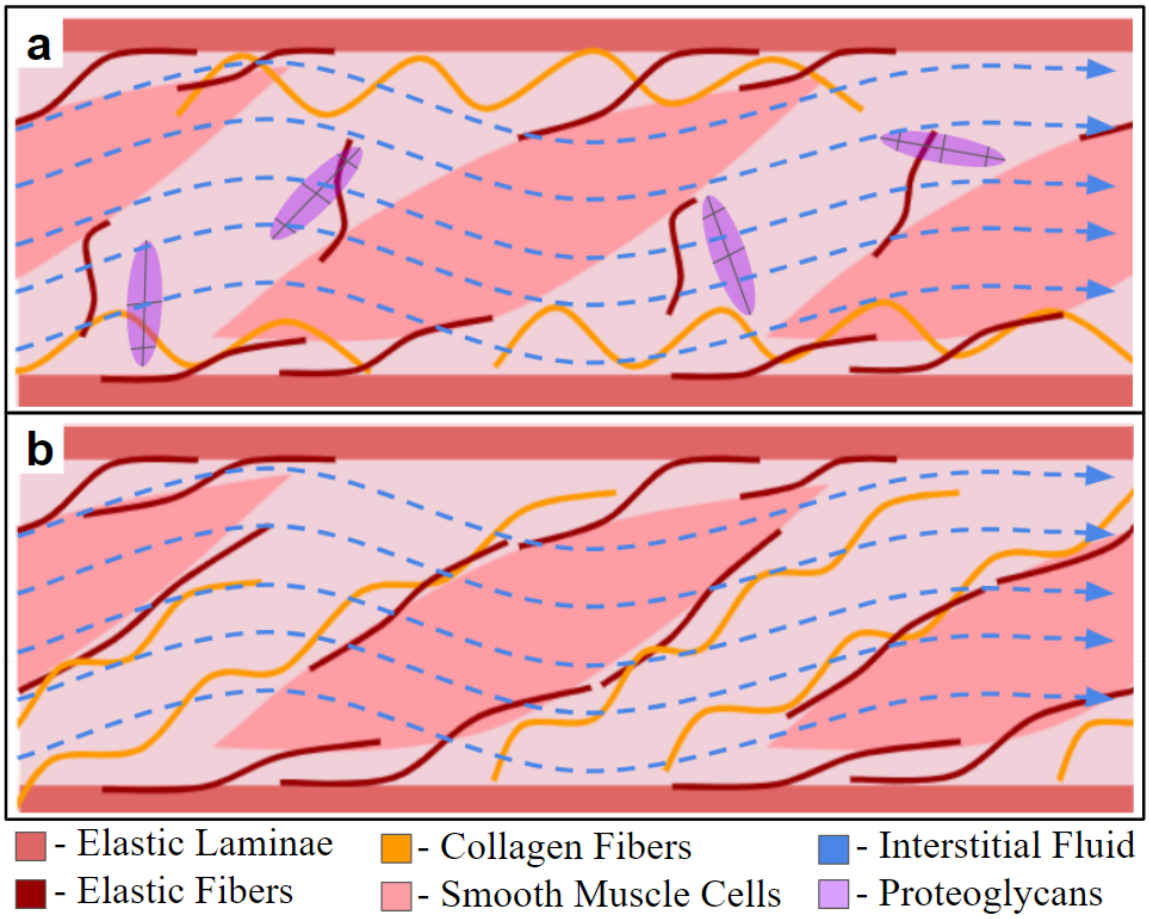


Figure 3: Important material units that comprise the proposed medial lamellar unit and their interaction with interstitial fluid in the (a) human and (b) porcine aortic walls. Medial lamellar unit adapted from Humphrey (2013).

in this thesis. In aneurysmal tissue, the lumen diameter size increases while the wall thickness remains constant or increases compared to normal aortic tissue (Freestone et al., 1995; Tang et al., 2005). Despite the preserved wall thickness, the intimal and adventitial layers of the aortic wall increase in thickness while the medial layer decreases in thickness (Tang et al., 2005). Degradation of the medial layer, particularly elastin and collagen, is commonly found in aneurysmal tissue (Fig. 4a-b) (Tang et al., 2005; Tong et al., 2013; Rabkin, 2015; Shen et al., 2019). As the tissue degeneration progresses, abundance of proteoglycans increases significantly and disrupts cell-matrix interactions (Humphrey, 2013; Wight, 2018). This modified structure of

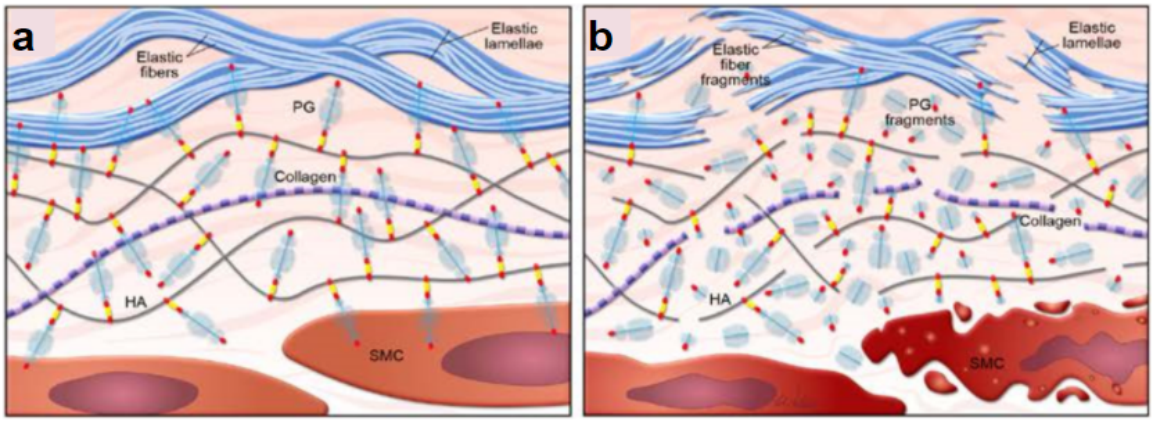


Figure 4: The medial layer microstructures of (a) non-pathological and (b) aneurysmal human aortic wall. (b) Shows the fragmented elastin fibers, collagen fibers, and cellular units that appear in the aneurysmal tissue along with an abundance of fragmented proteoglycans (Shen et al., 2019).

aneurysmal tissue is shown in Fig. 4 and likely impacts the mechanical response of the aorta.

## 2.2 Aortic Wall Mechanics

Although the importance of wall mechanics in the aortic wall is universally recognized, there are few, if any, models that accurately predict the response of the aortic wall for a given aorta. The lack of an accurate model can be attributed to the highly complex structure of the aorta and the myriad of factors that can impact aortic wall material including gender, age, smoking history, genetics, and more (Humphrey and Holzapfel, 2011). Additionally, the aorta is a compressible, hydrated, anisotropic, non-linear, and hyper-viscoelastic material, as the next section discusses.

### 2.2.1 Complexities of Aortic Tissue

With the complex properties of aortic tissue always present in mechanical tests, these properties need to be accounted for in all attempted analyses of aortic tissues. The compressibility of aortic tissue has been debated in the past with early studies showing that incompressibility was a valid assumption (Carew et al., 1968). However, more recent studies have shown that the aorta is compressible (Chuong

and Fung, 1984; Yosibash et al., 2014; Nolan and McGarry, 2016). For example, (Yosibash et al., 2014) found that the aortic wall was 2 to 6 percent compressible in physiological loading ranges.

The aqueous substance present in aortic tissue makes imaging of the aortic wall more complicated and requires dehydration of the tissue to get clear images. Dehydrating aortic tissue changes its mechanical properties (Costantini et al., 2019) which creates challenges when attempting to take accurate microstructural images of the aorta under mechanical loads. In a study of the hydraulic resistance of the aortic wall, Chooi et al. (2016) found that the hydraulic resistance of the medial layer dominates at pressures above 93 mm-Hg, which covers most of the physiological pressure range of 80 to 120 mm-Hg. Haslach (2010) shows the effect of moisture content on the mechanical response of elastin, a key microstructural component of the media.

Viscoelasticity, which is shown for aortic tissue in tension by (Delgadillo et al., 2010) and shear by Haslach et al. (2018b), complicates the analysis of aortic wall as evidenced by the additional constraints outlined by Haslach (2005). Any changes in loading or loading rates cause different responses in the tissue and creates a requirement for precise actuation of specimens in experiments. In vivo, the forces that act on the aorta are cyclical and repeat at a frequency of 1 to 1.67 Hz, which is the average resting heart rate of humans (Tripathi et al., 2011). Physiological forces vary under a change in heart rate, cyclic blood pressure amplitudes, and during individual blood pressure cycles. To create loading conditions that are representative of the physiological loads of the aortic wall, cyclical loading in which the dynamic response of the aortic wall is measured must be applied. For further discussion of dynamic loading, see section 2.4.

The anisotropies present in the aortic wall, outlined in section 2.1, add additional variables which are difficult to quantify on their own. Many studies have

attempted to quantify the effect of these anisotropies, along with hyperelastic effects, on the mechanical response of aortic tissue. Often, researchers use low deformation rates which establish a quasi-static loading condition in an attempt to decouple viscoelastic properties and analyze the anisotropic and hyperelastic behaviors. While quasi-static loads simplify analysis and testing, this type of loading does not represent the approximate steady state experienced by the aorta in vivo. Furthermore, it is commonly assumed that collagen fiber is the critical structural unit to examine due to its ability to withstand high loads. Researchers therefore impose tensile loads on the aortic wall because collagen fibers are recruited at high tensile loads when they are fully extended (Martin et al., 2011; Sommer et al., 2016). For both human and porcine aorta, hyperelastic properties under uniaxial tension (human e.g. Holzapfel (2006) and Tong et al. (2013) and porcine e.g. Purslow (1983) and Peña et al. (2019)) and biaxial tension (human e.g. Ferruzzi et al. (2011) and Duprey et al. (2016) and porcine e.g. Chow et al. (2014) and Mattson and Zhang (2017) have been studied extensively to characterize the stiffness of the aortic wall. While these tests effectively establish the tensile properties of collagen fiber and occasionally elastin, they rarely take into account other microstructural components, shear properties, or viscoelasticity of the tissue. Without characterization of these important material features, it is unlikely that an accurate model of the aortic wall can be developed. Moreover, little is known about the shear properties of the arterial wall. Researchers occasionally attempt to relate shear properties to the resulting data from tensile tests for linearly elastic materials. However, Martin et al. (2011) shows that the aortic wall is non-linear in a biaxial tensile test. Therefore, because the aorta is not linear elastic, it is not advisable to make a relation between uniaxial or biaxial tension and shear properties. Instead, shear testing, such as the tests conducted in this thesis, is a more direct and accurate path to identify important shear properties.

When taking all of these properties into account with the additional human

factors imposed on the aorta, it becomes clear that creating an accurate aortic wall model is a nearly impossible task.

### 2.2.2 Rupture Mechanics

Even less is understood about rupture mechanics of the aortic wall than non-pathological wall mechanics. Some researchers believe that failure is caused by tensile wall stress induced by large deformations. As a result, tests that investigate the damage mechanisms of collagen fibers under tension are common, such as the recent study by Peña et al. (2019). However, Haslach et al. (2011), Haslach et al. (2015), and Haslach et al. (2018a) showed that crack formation and propagation involved circumferential shear mechanisms within the wall. Additionally, Chow et al. (2014) found that both elastin and collagen fibers are progressively engaged at strains less than 20 percent, so it is unlikely that collagen fiber fracture is solely responsible for rupture in physiological conditions. Given the wavy structure and circumferential orientation of collagen fibers, it is increasingly apparent that they do not play a significant role in shear, and therefore rupture, mechanisms. One goal of this work is to produce more insight into the mechanisms of rupture and dissection because very little is known regarding these mechanisms. With a better understanding of rupture mechanics and the causes of dissection, more direct conclusions can be made on the potential effectiveness of future TEVGs.

### 2.2.3 Microstructure-Based Mechanics Approach

Rather than taking a continuum mechanics approach to define direct relationships for innumerous complex parameters, an approach that attempts to find indirect relationships between the microstructure of the aortic wall and its mechanics is used. Studies suggest that the structure of the aortic wall, and particularly the microstructure of the media, has a large effect on the mechanisms of rupture (Haslach et al., 2011; Haslach et al., 2015; Haslach et al., 2018a). The effect of the microstructure in these studies is evidenced by the slippage and apparent shearing between func-

tional units in the media as fractures propagate under a uniform internal pressure load. It is thus necessary to discern the shear properties of the aortic wall. Haslach et al. (2018b) found that under constant rate deformation, the shear stress response of non-pathological and aneurysmal aortic tissue is dependent on the rate of deformation. Because the aortic tissue is nonlinear viscoelastic, it is difficult to discern specific physiological shear properties under constant rate deformation. Therefore, a combination of cyclic loading and signal analysis techniques, such as that used in Leahy and Haslach (2018), Gipple and Haslach (2020), and Haslach et al. (2020), uncover the effect of more subtle shear properties. By separating frequency components of the shear stress versus time response, the effect of microstructural components other than collagen fiber can be analyzed. As shown in Fig. 3, the interaction of the medial microstructure components and interstitial fluid may cause internal shear stresses within the aortic wall. The proposed interstitial fluid drag force (Leahy and Haslach, 2018; Haslach et al., 2020; Gipple and Haslach, 2020) is analyzed in human non-pathological and aneurysmal aortic tissue to discover any differences in shear properties caused by degraded microstructure components in aneurysmal tissue. Porcine aortic tissue is also analyzed in this manner to establish data for comparisons between normal porcine aortic tissue and TEVG porcine aortic tissue. Given the importance of elastin in TEVGs (Miranda-Nieves and Chaikof, 2017), any differences between the microstructural mechanical response of normal and TEVG porcine aortic tissue could indicate potential TEVG failures.

## 2.3 Physiological Loading Range

In continuum mechanics, the stretch ratio is a commonly used variable to analyze the large deformation mechanics of soft tissue and hyperelastic materials (Holzapfel, 2000). The stretch ratio is defined as the ratio of the deformed length of a differential line segment and the undeformed length of the same line segment. For the aortic wall, the most significant deformation is the change in diameter resulting

from the cyclical interior blood pressure. Therefore, when defining the stretch ratio *in vivo*, the aorta can be approximated as a long, thin-walled cylindrical vessel under internal pressure (Anand and Christov, 2019). The principal axes are the radial, circumferential, and longitudinal directions, which are denoted as $x_1$, $x_2$, and $x_3$, respectively, in Fig. 5. Note that the $x_3$ axis is not pictured because it is the out-of-plane axis. For simplification, the aorta is assumed to be incompressible in this state. This assumption may be misguided because the compressibility of the arterial wall has been widely debated with several studies showing conflicting results as discussed in section 2.2.1. Despite these conflicting results, it is assumed that the compressibility of

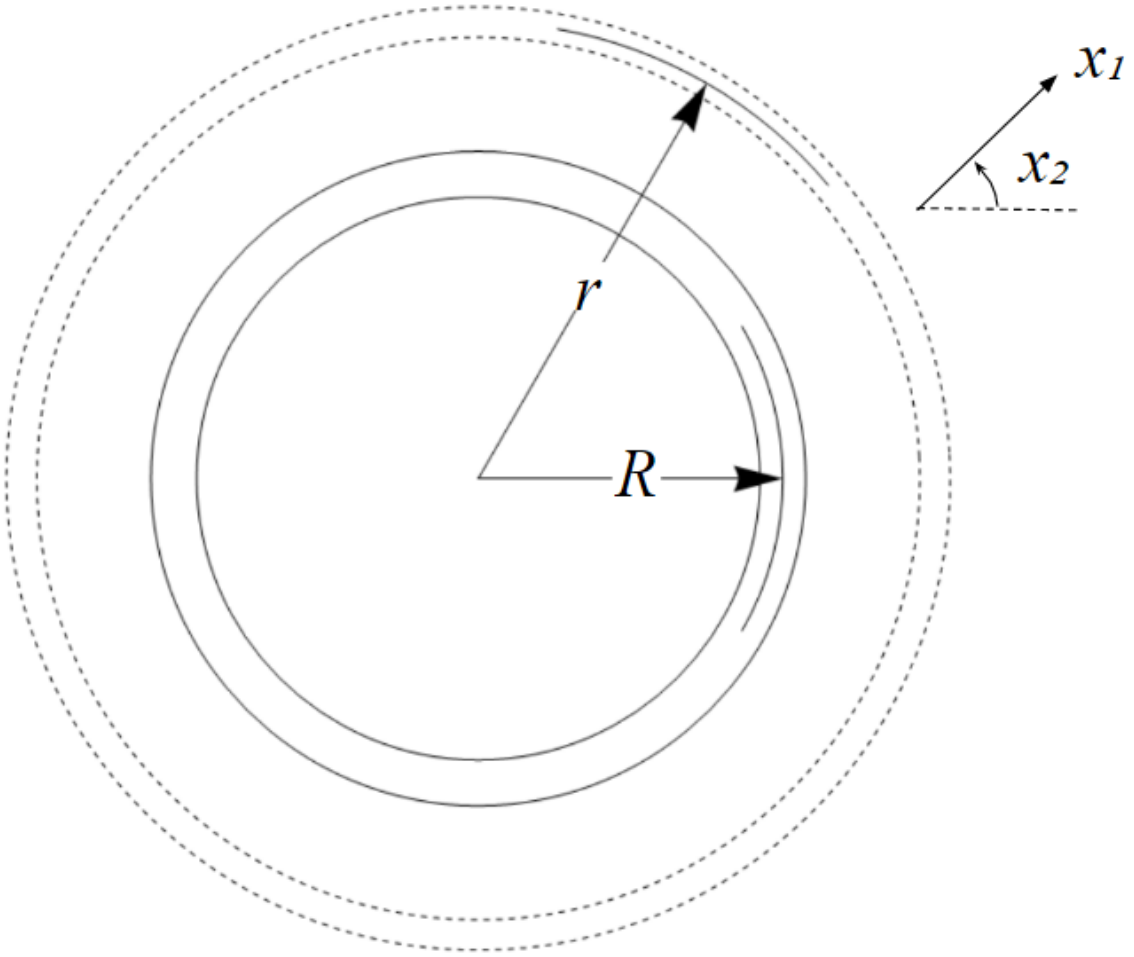


Figure 5: Deformed and undeformed positions for a cylindrical vessel undergoing internal pressure.

the arterial wall will not have a large enough effect on the stretch ratio to significantly impact the working range of the stretch ratio. With the incompressibility assumption, the stretch ratios *in vivo* are defined as

$$\lambda_1 = \frac{R}{r} = \frac{1}{\lambda}, \qquad \lambda_2 = \frac{r}{R} = \lambda, \qquad \lambda_3 = 1 \tag{1}$$

where r is the current radius and R is the unstretched radius. Under the incompressibility assumption, $\lambda_1$ is the radial stretch, $\lambda_2$ is the circumferential stretch, and $\lambda_3$ is the longitudinal stretch. The aorta is assumed to be infinitely long, eliminating the longitudinal stretch. Removing longitudinal stretch provides additional simplification, but it makes this set of values even more approximate because longitudinal stretch is present *in vivo*. For the aorta, the reference radius is the diastole radius and the current radius is dependent on the current state of the aortic diameter. The maximal stretch ratio is found at the systole diameter. Table 1 shows the *in vivo* diastolic and systolic diameters recorded in various studies that use cardiac imaging. It is important to note that cardiac imaging *in vivo* currently has several limitations, including an inverse relationship of diagnostic accuracy to vessel diameter (White et al., 2014). Using these diameter values, the stretch ratio for each group is found from Eqn. 1. Because these studies do not directly calculate the stretch ratio, standard deviation values for the stretch ratio are calculated using non-linear propagation of

Table 1: Results of human ascending aorta diameter studies

| Study | N | Age | Diastole (mm) | Systole (mm) | Calculated $\lambda$ |
|---|---|---|---|---|---|
| Carrascosa et al. (2013) | 30 | 59 ± 16 | 30.8 ± 5.1 | 33.3 ± 5.8 | 1.08 ± 0.08 |
| Martin et al. (2013) | 15 | 30-49 | 29.9 ± 2.8 | 32.5 ± 2.5 | 1.09 ± 0.05 |
| | 10 | 50-59 | 32.4 ± 3.8 | 34.7 ± 3.2 | 1.07 ± 0.06 |
| | 20 | 60-79 | 33.2 ± 3.2 | 35.1 ± 3.3 | 1.06 ± 0.05 |
| Huang et al. (2019) | 25 | 51 ± 11 | 30.57 ± 1.94 | 32.35 ± 1.95 | 1.06 ± 0.03 |
| Average | | | 31.2 ± 3.5 | 33.4 ± 3.6 | 1.07 ± 0.05 |

error. These studies also do not analyze correlations between diastolic and systolic values, so a high correlation ($\rho = 0.9$) between diastolic and systolic values for a given patient is assumed. With this assumption, the upper bound of expected physiological stretch ratios is approximately 1.12.

## 2.4 Signal Analysis

As discussed previously, the aortic wall is a nonlinear, viscoelastic, and heterogeneous body. Because of the tissue's viscoelasticity, any loading changes on the tissue cause a transient response in which the response of the tissue varies with time. Under sinusoidal loading, the transient response eventually stabilizes to an approximately periodic response where there are few differences between cycles. The transient region contains signals that have any variance between cycles. The quasi-periodic region contains signals that repeat over a specified interval of time. For a signal to be periodic, both the signal values and time interval, known as the period, must be the same on subsequent cycles.

Experimentally, signals rarely, if ever, exhibit a perfectly periodic response. Requirements for periodicity must therefore be defined. In this study, a signal is defined as periodic if both the amplitude of the response and the period time length differ by less than 5 percent on subsequent cycles (Fig. 6). It must be said that specimens do not always stay in a periodic state after the initial transition from the transient region. Occasionally, a specimen transitions into the periodic state and exhibits an increase in amplitude on subsequent cycles. Because of these slight variances, the periodic region of the shear stress response of specimens is referred to as quasi-periodic. Based on the periodicity of the signal, different approaches to analyze the frequency components of a signal can be taken. The Fourier transform is a widely-used form of signal-processing which converts signals in the time domain to the frequency domain or vice versa. In using this transform, the magnitude of different frequencies present within a signal can be found. The Fourier transform can be

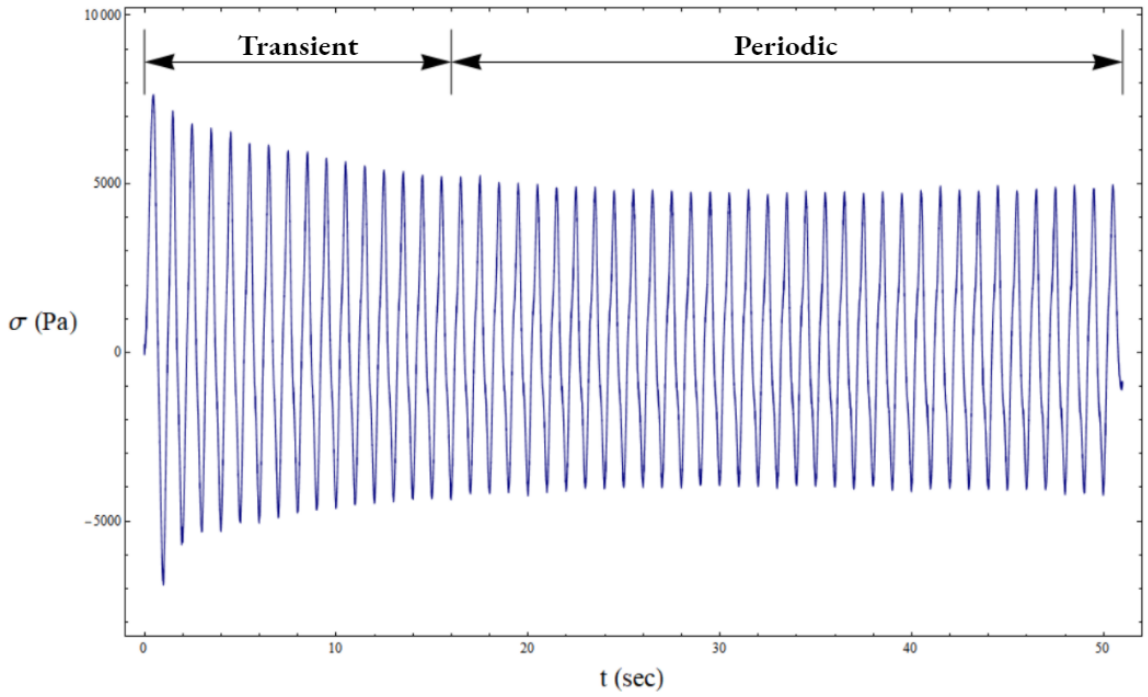


Figure 6: Transient and quasi-periodic regions of the shear stress response of aortic tissue. The deformation amplitudes are either 1.5 or 3 mm and the frequency is 1 Hz. The figure displays the shear stress response of specimen P2-j which is deformed at a 1.5 mm amplitude.

used on both periodic and non-periodic signals through the two different approaches described in sections 2.5 and 2.6 which are adapted from Press et al. (1989).

## 2.5 Discrete and Non-Periodic Fourier Transform

The Fourier transform is a useful tool which allows time-dependent signals to be converted from the time domain to the frequency domain and vice versa. For any signal *f(t)* in the time domain, there is a corresponding function *F(ξ)* which describes the same signal in the frequency domain. One moves interchangeably between these two signals by way of the Fourier transform equations:

$$\begin{aligned} F(\xi) &= \int_{-\infty}^{\infty} f(t) e^{-2\pi i \xi t} dt \\ f(t) &= \int_{-\infty}^{\infty} F(\xi) e^{-2\pi i \xi t} d\xi \end{aligned} \tag{2}$$

where the frequency, $\xi$, is in Hertz. Signals are commonly sampled at evenly spaced intervals of time, creating a discrete signal. The signal *f(t)* is then defined by the sequence of sampled values at each interval. The signal is then defined as

$$f_j \;=\; f(t_j), \qquad t_j \;=\; jh, \qquad j \;=\; 0, 1, 2, ..., N-1 \tag{3}$$

where $h$ is the uniform sampling interval and $N$ is the total number of consecutively sampled values. Using discretized versions of the Fourier transform only allows for a limited range of frequencies to be reliably recovered from the signal *f(t)*. This range is defined by the Nyquist frequency:

$$\xi_c \;=\; \frac{1}{2h} \tag{4}$$

Only frequency values within the Nyquist frequency range of $-\xi_c$ to $\xi_c$ are sought because frequencies found outside of this range are subject to aliasing.

With $N$ values of input, it is evident that there can only be $N$ values of independent outputs. Therefore, a discrete number of frequencies within the Nyquist frequency range is sought:

$$\xi_j \;=\; \frac{j}{Nh} \qquad j \;=\; -N/2, ..., N/2 \tag{5}$$

With the finite number of sampled points and frequencies, the Fourier transform integral (Eqn. 2) is approximated as

$$F(\xi_j) \;=\; \int_{-\infty}^{\infty} f(t) e^{-2\pi i \xi_j t} dt \;\approx\; h \sum_{k=0}^{N-1} f_k e^{-2\pi i k j / N} \tag{6}$$

The final summation term in Eqn. 6 is known as the discrete Fourier transform:

$$F_j \;=\; \sum_{k=0}^{N-1} f_k e^{-2\pi i k j/N} \tag{7}$$

In practice, the power contained in each frequency is a commonly found variable. The total power in a signal, $P$, is found using:

$$P \;=\; \int_{-\infty}^{\infty} |f(t)|^2 dt \;=\; \int_{-\infty}^{\infty} |F(\xi)|^2 d\xi \tag{8}$$

where the first equality in Eqn. 8 is the definition of power and the second equality is Parseval's theorem.

In most cases, one does not distinguish between positive and negative frequencies because the power for specific frequency is sought. When this is the case, the one-sided power spectral density (PSD) of the signal $f$ is defined as

$$P_f(\xi) \;= |F(\xi)|^2 + |F(-\xi)|^2 \qquad 0 \le \xi < \infty \tag{9}$$

When the signal $f$ is real, both terms in Eqn. 9 are equal and the one-sided PSD reduces to

$$P_f(\xi) \;= 2|F(\xi)|^2 \qquad 0 \le \xi < \infty \tag{10}$$

With a discretely sampled signal $f_j$, Eqn. 10 applies for all discrete frequencies $\xi_j$ (as defined in Eqn. 5) from $0 \le \xi < \xi_c$.

In this study, Eqn. 6 and 10 are used to find the one-sided PSD of the entire shear stress response of aortic tissue. This includes both the transient and steady state regions of the signal, as denoted in Fig. 6. The one-sided PSD for specimen H6-b is shown in Fig. 7 as an example of a typical one-sided PSD.

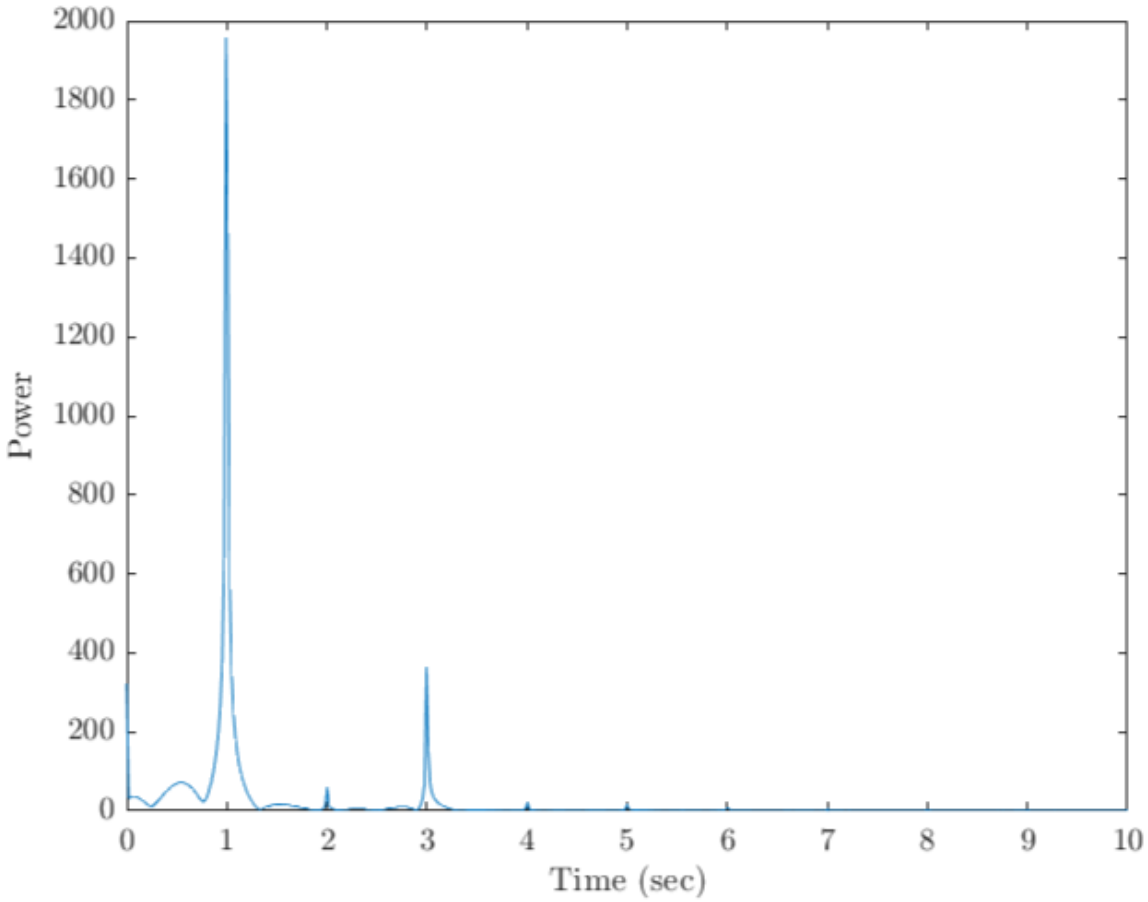


Figure 7: One sided PSD for specimen H6-b.

## 2.6 Discrete and Periodic Fourier Transform

In the case of a periodic signal, simplifications of the non-periodic Fourier transform can be made. For a continuous, periodic signal, *f(t)* is written as the sum of frequency modes multiplied by their magnitude:

$$f(t) = \sum_{k=-\infty}^{\infty} F_k e^{2\pi i k t} \tag{11}$$

This equation is known as the inverse Fourier transform because it transforms values from the frequency domain to the time domain. The coefficients $F_k$ are known as the Fourier coefficients and describe the signal in the frequency domain. The frequency modes ($u^k = e^{2\pi i k t}$) notably form an orthonormal basis in the trigonometric space.

Because the modes are orthonormal, the Fourier coefficients can be found by taking the inner product of the signal and the modes:

$$F_k \;=\; (f, u^k) \;=\; \frac{1}{T}\int_0^T f(t)e^{-2\pi ikt}dt \tag{12}$$

where $T$ is the period.

For a signal that is sampled at a finite number of points as in Eqn. 3, the frequency modes are also discretized by

$$u_j^k \;=\; e^{2\pi ikj/N} \qquad j \;=\; 0, 1, 2, ..., N-1 \tag{13}$$

Once again, only frequencies within the Nyquist frequency are sought (Eqn. 4). The Fourier transform in Eqn. 12 is approximated as

$$F_k \;=\; \frac{1}{T}\int_0^T f(t)e^{-2\pi ikt}dt \;\approx\; \frac{1}{N}\sum_{j=0}^{N-1} f_j e^{-2\pi ikj/N} \tag{14}$$

and the inverse Fourier transform is approximated as

$$f_j \;=\; \sum_{k=-\infty}^{\infty} F_k e^{2\pi ikt} \;\approx\; \sum_{k=0}^{N-1} F_k u_j^k \tag{15}$$

A continuous interpolating function which approximates the discrete input signal $f_j$ is found through the discretization of equation 11:

$$\tilde{f}(t) \;=\; \sum_{k=0}^{N-1} F_k e^{2\pi ikt} \;=\; \sum_{k=0}^{N-1} F_k u^k(t) \tag{16}$$

Frequency modal terms of $k >$ ($N$-1)/2 coincide with frequency modal terms of $k >$ -($N$-1)/2 and $k < 0$. The interpolating function can then be rewritten as

$$\tilde{f}(t) \;=\; F_0 u^0(t) + ...F_n u^n(t) + F_{N-n}u^{-n}(t) + ...F_{N-1}u^{-1}(t) \tag{17}$$

where $n$=($N$-1)/2 for an odd number of total samples $N$. Using the trigonometric identities of the sine and cosine functions, Eqn. 17 can be manipulated further:

$$\tilde{f}(t) \;=\; a_0 + \sum_{k=0}^{n} (a_k cos(2\pi kt) + b_k sin(2\pi kt)) \tag{18}$$

where the coefficients $a_0$, $a_k$ and $b_k$ are found from the Fourier coefficients $F_k$ and the aforementioned trigonometric identities. This transformation results in the following equations:

$$\begin{aligned} a_0 &= \frac{1}{T}\int_0^T f(t)dt \\ a_k &= \frac{2}{T}\int_0^T f(t)cos(2\pi kt)dt \\ b_k &= \frac{2}{T}\int_0^T f(t)sin(2\pi kt)dt \end{aligned} \tag{19}$$

Note that $a_0$ corresponds to the mean value of the data. It is also evident that there are no terms that account for phase shifts of the signal, confirming that the simplified Fourier transform must be used on a periodic signal. If there were an even number of total samples, a similar manipulation of the interpolating function can be used. For this study, the discrete, periodic Fourier transform is used on all cycles of the shear stress response of aortic tissue, regardless of the transient and steady state regions denoted by Fig. 6. Fig. 8 shows an example of the harmonics that comprise the overall interpolating function for cycle 30 of specimen H6-b.

For the Bose-Electroforce Testbench detailed in section 3.2, the shear stress response of aortic tissue specimens to a 1Hz sinusoidal loading is sampled at every 0.0002 seconds. This sampling interval inserted into equation 4 results in a Nyquist frequency of 2,500 Hz. Given that the deformation loading frequency is significantly lower than the Nyquist frequency, any aliasing of the tissue response signal is not considered. In the quasi-periodic state, the period of the tissue response is assumed

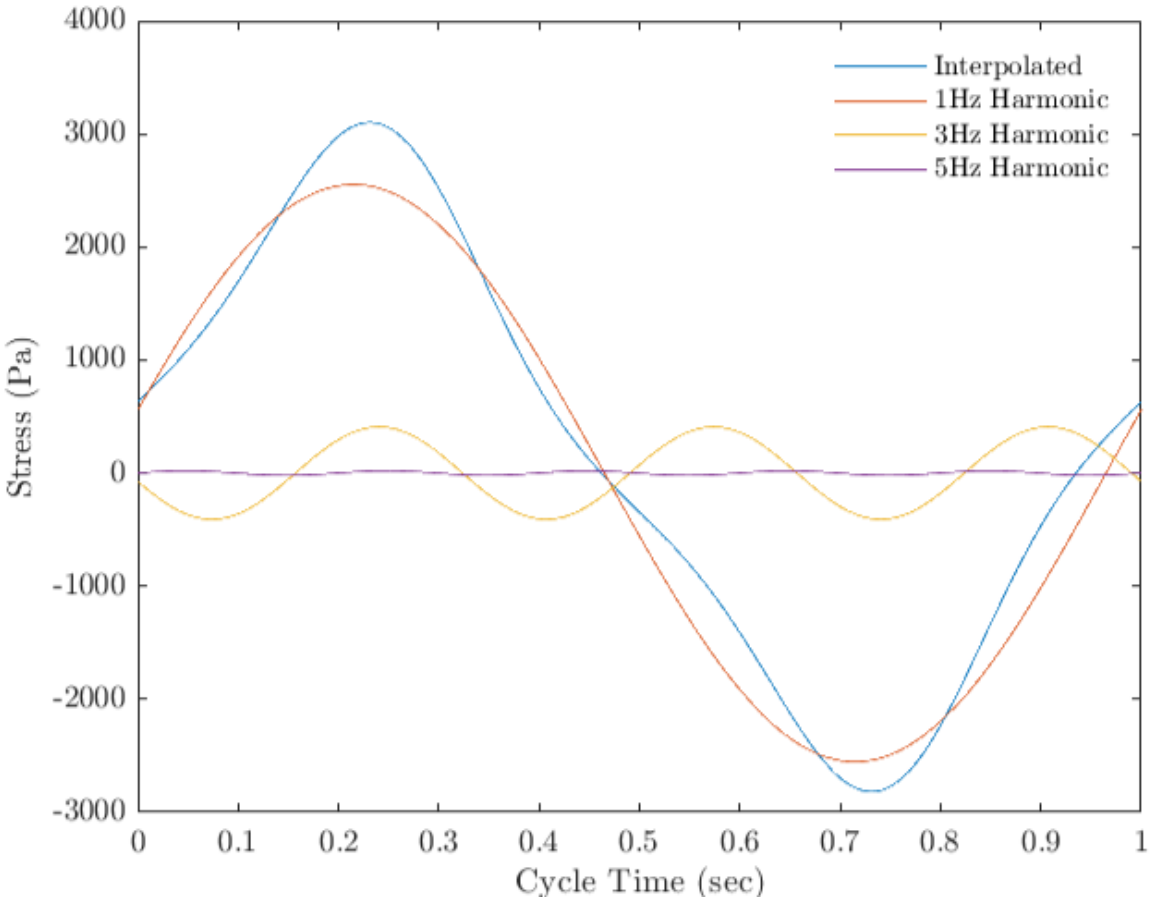


Figure 8: Decomposed frequencies of interpolated stress for cycle 30 of specimen H6-b.

to be equivalent to the sinusoidal deformation period of 1 second. With this 1 second period, 5,000 total samples are recorded in each cycle.

# 3 Methods and Materials

## 3.1 Specimen Acquisition and Preparation

From the moment of excision, fresh human aortic tissue samples are stored in a Plasma-lyte solution in the operating room and porcine aortic tissue samples are stored in a Phosphate Buffered Saline (PBS) solution. All specimens are stored at a temperature of 4°C and tested within 72 hours. With IRB approval, human aortic tissue samples are obtained directly from the operating room after either standard aneurysmal aorta repair or discarded non-pathological tissue from transplant procurement. Porcine aortic tissue samples are shipped overnight in phosphate-buffered saline (PBS) from a USDA certified biological raw materials company. All human tissue samples in this study are from the ascending thoracic aorta. The human samples from which specimens are cut are often ring shaped and 20 mm in width (Fig. 9a), but they may not always be fully intact rings. Porcine tissue samples contain the entirety of the thoracic aorta from the sinotubular junction to the end of the descending thoracic aorta with diameters up to 25 mm at the sinotubular junction (Fig. 9b). Specimens obtained from the porcine tissue samples originate in the ascending thoracic aorta to be consistent with the human tissue samples.

Fat deposits are carefully removed from the adventitial layer of each tissue sample with iris scissors and a number 11 scalpel to ensure that the fat has no effect on the response of the aortic wall. Using a guiding template, 6 mm by 6 mm specimens are cut from the tissue samples with a fresh scalpel blade. The small specimen size is chosen to both minimize the curvature of the specimens and to maintain uniformity in wall thickness throughout the specimens. The specimens are cut in alignment with the circumferential and longitudinal axes (Fig. 9c). When a specimen is fully separated from the tissue sample, the approximate thickness of the specimen is measured by hand using a digital micrometer without compressing the specimen.

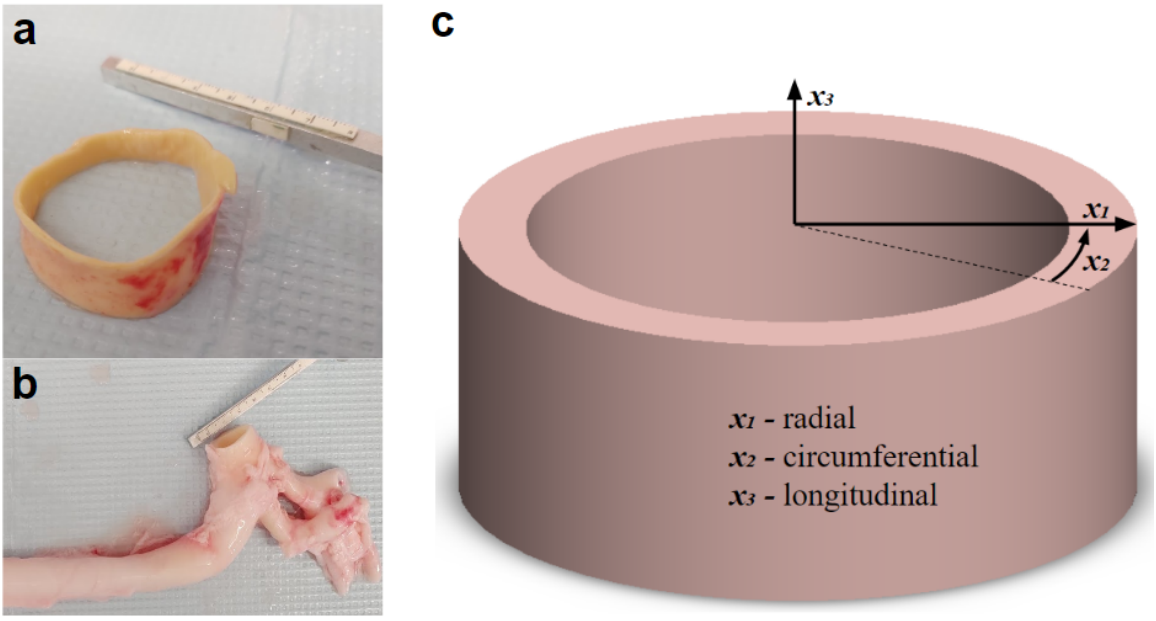


Figure 9: (a) Typical human aortic tissue sample. (b) Typical porcine aortic tissue sample. (c) Principal axes for aortic tissue samples.

## 3.2 Shear Testing Apparatus

A custom designed shear test fixture (Fig. 10) applies translational shear deformation for experimental analysis of aortic specimens. The top grip is electromagnetically controlled by the Bose-Electroforce Testbench 250N mover. The linear translation of the mover may be programmed to follow various deformation functions. The bottom grip is attached in the horizontal plane to a 250 gram load cell (Interface WMCP-250G-567) to measure the reaction force. The bottom grip is also supported in the horizontal plane by a linear ball bearing (Del-tron M-1 linear ball slide) with a manufacturer-specified 0.003 coefficient of friction. The bearing ensures that the bottom grip remains parallel to the horizontal plane while providing low resistance to translational forces. The bottom grip, load cell, and linear ball bearing are fixed to a support bracket through the use of a spring-loaded stage (ThorLabs T12X). The stage can be raised or lowered in the vertical plane to adjust the distance between the top and bottom grips for specimens of different wall thickness. Both the Bose-

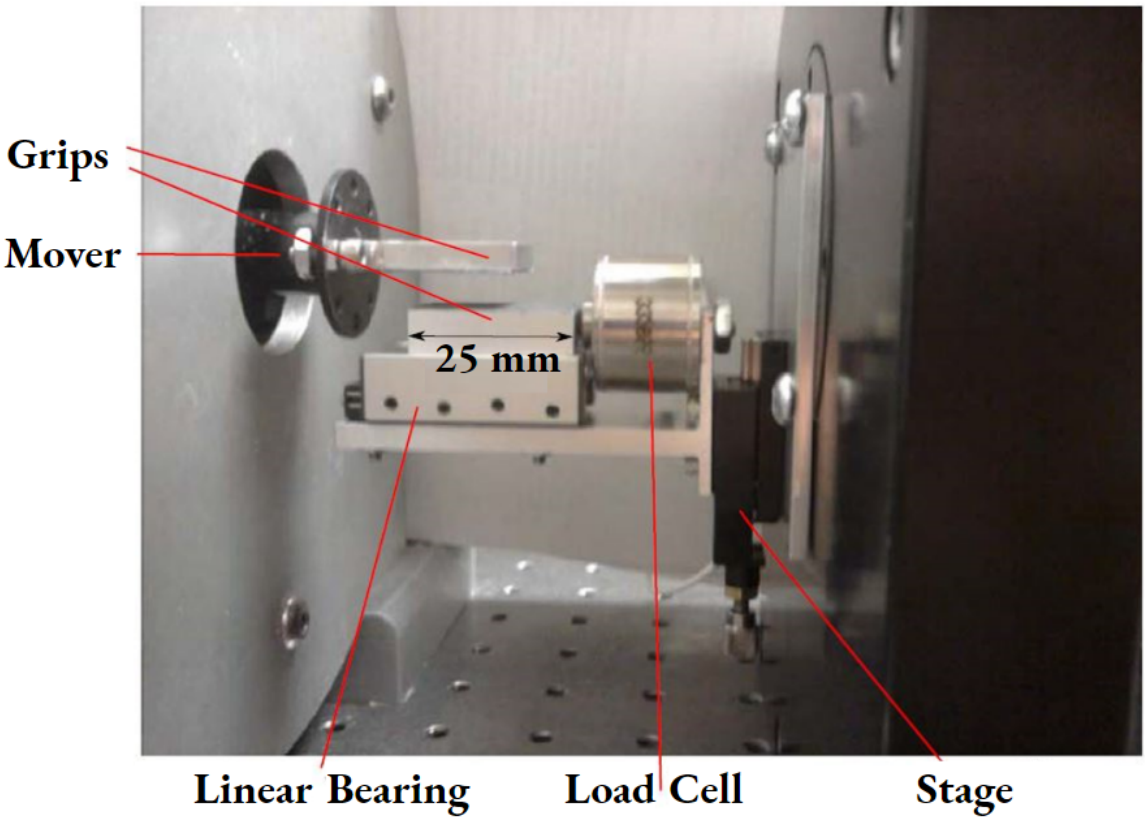


Figure 10: Uniquely-designed shear testing apparatus and its critical components.

Electroforce Testbench and the support bracket are fixed to a stationary stand (Fig. 10).

The Bose proprietary software WinTest 4.1 controls the desired motion of the mover to deform specimens. Throughout the tests, WinTest records the time, displacement of the mover, and reaction force of the load cell. Data points are sampled at the shortest interval allowed by WinTest, 0.0002 seconds, to obtain the maximal amount of points for analysis.

## 3.3 Protocols

The prepared specimen is aligned with the desired axis of testing, either circumferential or longitudinal, and carefully glued to the bottom grip of the shear testing apparatus using 3M Vetbond tissue adhesive. A small drop of glue is then applied to the top surface of the specimen and the stage is raised so as to fully

contact the top surface of the specimen to the bottom surface of the top grip without compressing the specimen. The manufacturer specifies a 15 second dry time between soft tissue and metal, so the glue is given 90 seconds to dry to ensure bonding of the surfaces.

The specimens are aligned in either the circumferential or longitudinal axes and sheared under deformation-controlled displacement in either constant rate or sinusoidal translational shear deformation. For constant rate tests, the mover deforms specimens from 0 mm to 3 mm at rates of either 1mm/sec or 12 mm/sec. The deformation rates of 1 mm/sec and 12 mm/sec are chosen because they are extremes of physiological loading rate. For sinusoidal tests, the mover deforms specimens at a 1 Hz frequency with amplitudes of either 1.5 mm or 3 mm. The deformation frequency of 1 Hz is chosen because it is close to the physiological pulse rate. Circumferential and longitudinal directions are chosen to test the influence collagen fibers, which preferentially align in the circumferential axis.

Both human and porcine specimens are excised from the thoracic ascending aorta and loaded in either constant rate shear or sinusoidal shear. Constant shear deformation rates of 1 mm/sec and 12 mm/sec are used for specimens in either the circumferential or longitudinal axes. Therefore, there are 4 constant rate groups for comparative analyses: porcine circumferential deformed at 1 mm/sec (cP1C), porcine longitudinal deformed at 1 mm/sec (cP1L), porcine circumferential deformed at 12 mm/sec (cP12C), and porcine longitudinal deformed at 12 mm/sec (cP12L). In each of these groups, 10 specimens are used, creating 40 total constant rate specimens for comparative analysis.

Sinusoidal deformation amplitudes of 25% and 50% are used for specimens in either the circumferential or longitudinal axes. Therefore, there are 8 sinusoidal groups for comparative analyses: porcine circumferential at 25% deformation (P25C), porcine longitudinal at 25% deformation (P25L), porcine circumferential at 50% de-

formation (P50C), porcine longitudinal at 50% deformation (P50L), human circumferential at 25% deformation (H25C), human longitudinal at 25% deformation (H25L), human circumferential at 50% deformation (H50C), and human longitudinal at 50% deformation (H50L). For each of these groups, 11 individual specimens are analyzed, creating 88 total sinusoidal specimens for comparative analysis.

## 3.4 Analysis

Because of the compressibility of the aorta, the exact specimen geometry during shear deformation is unknown (Fig. 11). Therefore, traditional strain measures, such as the simple shear stretch ratio for incompressible hyperelastic materials (Treloar, 1975), cannot be used. Instead, a simplified stretch ratio is defined to be $\lambda = 1 + d/L$ with the specimen length $L$ remaining a constant 6 mm for each specimen. Experiments with a 1.5 mm amplitude are referred to as 25% deformation tests ($d_0/L = 1.5\text{mm}/6\text{mm}$) and experiments with 3 mm amplitudes are referred to as 50% deformation tests ($d_0/L = 3\text{mm}/6\text{mm}$).

For constant rate specimens, deformation and shear stress data are recorded throughout the test (Fig. 12). The maximum shear stress, $\sigma_{max}$, and the time at which it occurs, $t_{max,\sigma}$, are recorded. The initial point in which the shear deformation is greater or equal to 3 mm is recorded as the initial time of maximum deformation, $t_{max,d}$. The lead time, $\Delta t$, is the difference between the time of maximum deformation and maximum stress ($\Delta t = t_{max,d} - t_{max,\sigma}$). The relaxation stress, $\sigma_r$, is recorded as the stress 60 seconds after $t_{max,d}$. Using these values, the Relaxation Fraction ($RF$) is recorded as

$$RF = \frac{\sigma_{max} - \sigma_r}{\sigma_{max}} \tag{20}$$

The $RF$ is a measure of the fraction of stress recovered in the specimen over 60 seconds. Higher $RF$ magnitudes indicate that the specimen is able to recover more

stress in the same time period as lower $RF$ magnitudes.

For sinusoidal specimens, discrete and non-periodic Fourier Transforms are performed to analyze the power (Eqn. 10) of each frequency contained within the entire test. For all specimens, each of the 50 deformation cycles in the test are separated for analysis of both stress and deformation data. In each cycle, the time of maximum

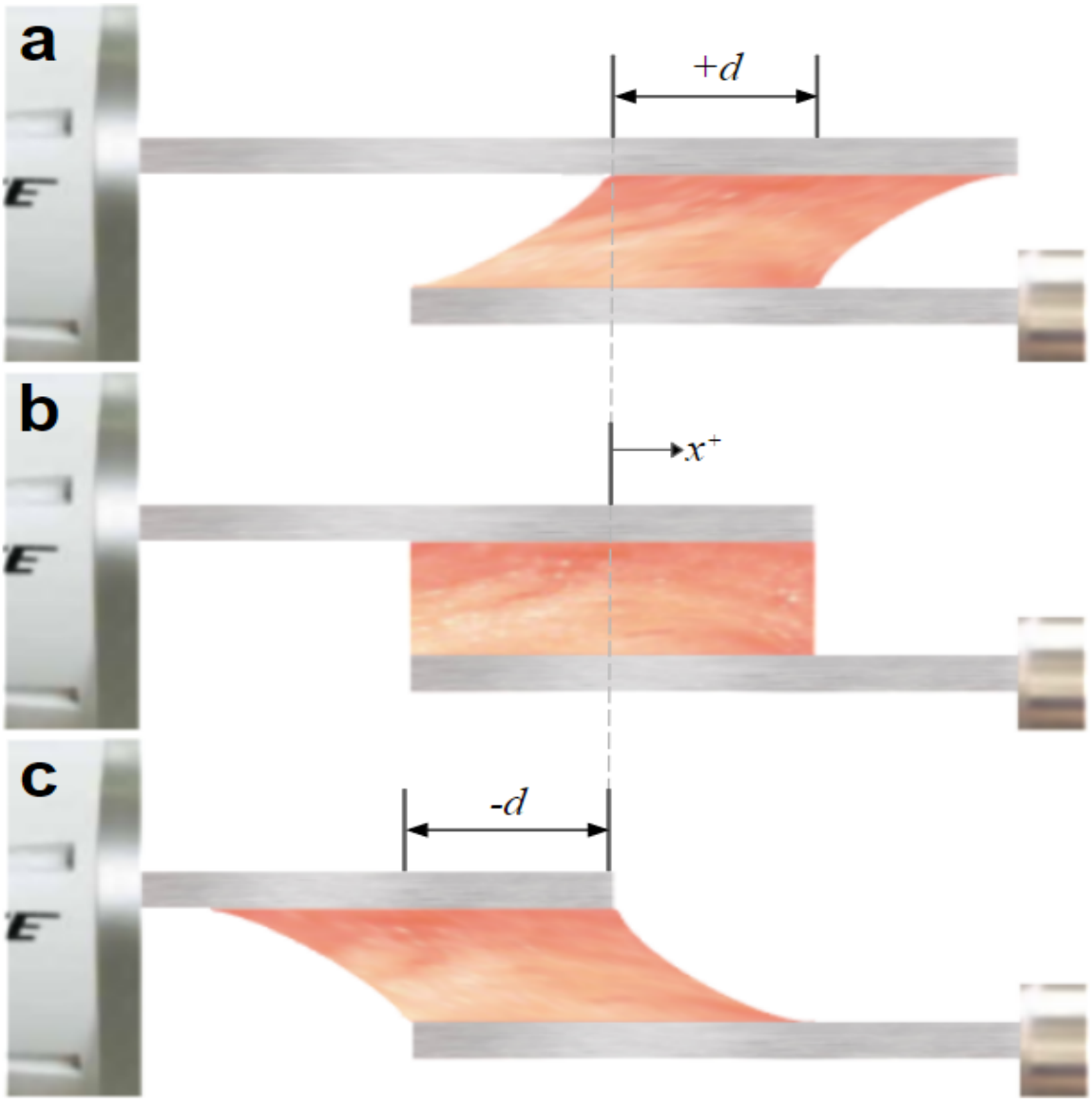


Figure 11: Side view of the shear deformation of a specimen and the visual representation of the measure of displacement, $d$, at (a) positive deformation, (b) no deformation, and (c) negative deformation. Note that when the specimen is sheared, the vertical edges of the specimen curve, indicating that the specimen is not in simple shear.

and minimum stresses are compared to the time of maximum and minimum deformations ($\Delta t_{maxormin} = t_d - t_\sigma$). The time difference between stress and deformation is the lead time, $\Delta t$, and is equal to the average time difference for maximum and minimum peaks for the deformation cycle for sinusoidal tests ($\Delta t_i = 0.5(\Delta t_{i,max} + \Delta t_{i,min})$). The stress amplitude in each deformation cycle is recorded ($\sigma_A = 0.5(\sigma_{max} - \sigma_{min})$). Additionally, Fourier Transforms are performed on stress data using Eqn. 19 to ob-

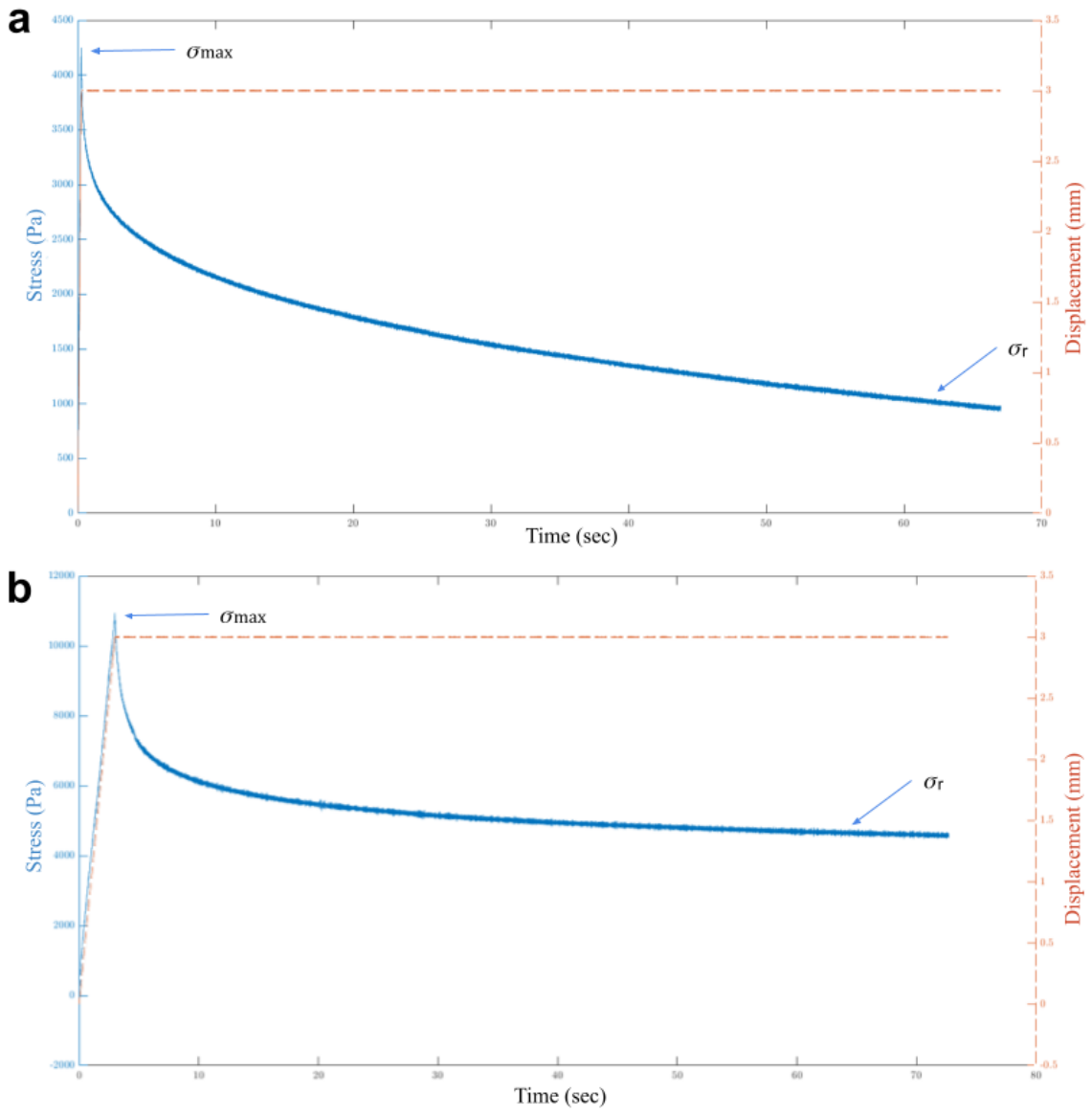


Figure 12: Typical specimen shear stress response under constant rate deformation for (a) 12 mm/sec and (b) 1 mm/sec. Displacement is plotted in red for reference.

tain the sine and cosine coefficients for each harmonic frequency. An interpolating function (Eqn. 18) containing the 1, 3, and 5 Hertz harmonics is created to visually compare with recorded stress data from which the harmonics are decomposed from (Fig. 13). The total magnitude of each harmonic, $\sigma_k = \sqrt{a_k^2 + b_k^2}$, is calculated for each cycle.

Previous work by Leahy and Haslach (2018) establishes a relationship between harmonic shear stress components and the interstitial fluid-solid drag force, $F_d$. Using a dimensional analysis with the Buckingham Pi theorem, the interstitial fluid-solid drag force involves the magnitude of the third harmonic $\sigma_3$. From the analysis, the drag force equation is defined as

$$F_d = \sigma_3 A_p = 0.25 \rho A g_2(\pi_2, \pi_4) a (v_1 2\pi)^2 \tag{21}$$

where $A_p$ is the specimen surface area, $A$ is a function of the initial solid volume fraction and the specimen cross sectional area, $g_2$ is a function of the unknown dimensionless parameters $\pi_i$, $a$ is the deformation amplitude, and $v_1$ is the average interstitial fluid velocity. The third harmonic is therefore proportional to the interstitial fluid-solid drag force. Because the magnitude of harmonics vary due to a variety of specimen differences, the normalized Interaction Ratio ($IR = \sigma_3/\sigma_1$) is calculated to yield a value that is comparable between specimen groups. An additional Roughness Ratio ($RR = \sigma_5/\sigma_1$) measures the normalized smoothness of the shear stress response versus time curve. The $RR$ may also measure the roughness of the elastin lamellae surfaces that interact with the interstitial fluid.

The $IR$ and $RR$ are computed for each of the 50 cycles to analyze how the stress response of the dynamically changes throughout the test. The dynamic response of the tissues yields insight into potential incompatibilities. Time differences between the peak shear stress response and the peak shear deformation are recorded to measure quasi-periodicity. Tissues with significantly different time differences in-

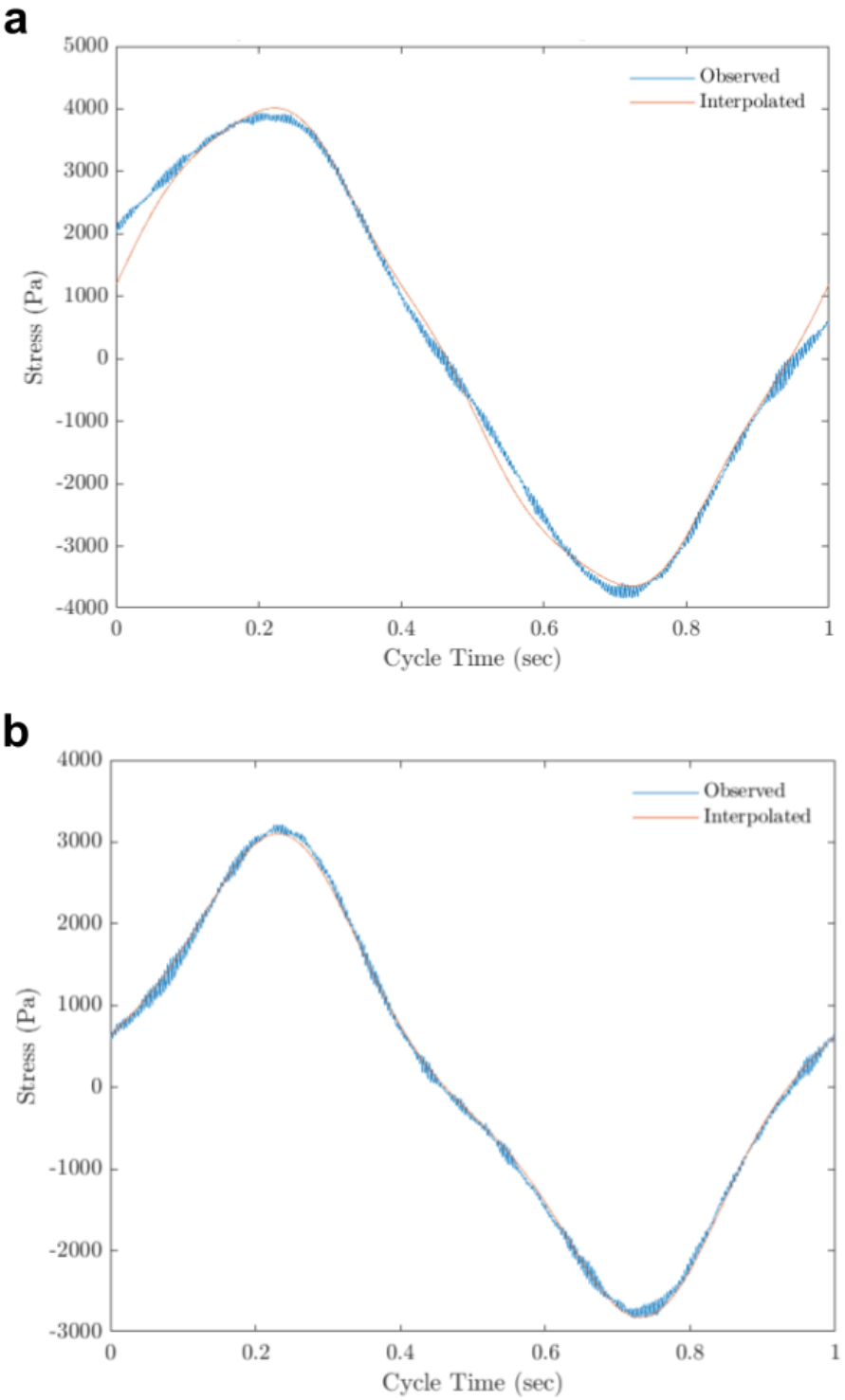


Figure 13: The actual versus interpolated shear stress response of specimen H6-b for (a) cycle 1 and (b) cycle 30. (a) Shows the typical transient response interpolation accuracy and (b) shows the typical quasi-periodic response interpolation accuracy.

dicates a potential dynamic incompatibility between the tissues.

## 3.5 Statistical Power

In scientific studies, the population size used for statistical analyses is critical to determine the usefulness of the analysis results. Statistical power defines the probability of detecting significant effects that truly exists in a population (Park and Schutz, 1999). To determine the sample size necessary to achieve a desired statistical power, the sample size, $n$, is defined as

$$n = \left(\frac{Z \cdot S}{E}\right)^2 \tag{22}$$

where $Z$ is a the standard normal distribution value to achieve a desired confidence interval, $S$ is the standard deviation of the population, and $E$ is the margin of error determined to be significant from a practical standpoint.

In this study, quasi-periodic $IR$ and $RR$ amplitudes are statistically analyzed to determine the effect of group types. To determine a target sample size for each specimen group, the quasi-periodic $IR$ amplitude is analyzed. The average quasi-periodic $IR$ across all tests in this study is 0.2303. The maximum margin of error is therefore chosen to be 0.03 with a confidence interval of 95% ($Z = 1.96$). The standard deviation of the quasi-periodic Interaction Ratio across all tests in this study is 0.0504. The required number of samples to not exceed this margin of error is therefore $n = (1.96 \cdot 0.0504/0.03)^2 = 10.8 = 11$. A sample size of 11 specimens per specimen group is therefore chosen to achieve a large statistical power.

## 3.6 Statistical Analysis

In total, there are 100 one-factor Analyses of Variances (ANOVAs) performed in this thesis to analyze mechanical properties of aortic tissue. One-factor ANOVAs analyze the effect of a single factor for two independent groups (Snedecor and Cochran, 1980). All critical p-values are set to be $\alpha = 0.05$ with null hypotheses

that there is a significant difference between the analyzed groups. For constant rate specimens, a set of 16 one-factor ANOVAs analyze the effects of deformation rate and deformation direction on the lead time, maximum stress, relaxation stress, and Relaxation Fraction of specimens. For sinusoidal specimens, a set of 84 one-factor ANOVAs analyze the effects of tissue type, deformation amplitude, and deformation direction on the quasi-periodic total stress amplitudes, 1 Hz harmonic magnitudes, 3 Hz harmonic magnitudes, 5 Hz harmonic magnitudes, lead times, Interaction Ratios, and Roughness Ratios of specimens. For each group, there are 11 specimens to analyze. The number of specimens is chosen to be at least 11 to obtain a statistical power large enough validate the results of the one-factor ANOVAs.

# 4 Results

For both constant rate and sinusoidal tests, aortic tissue specimens have shown non-linear and hyper-viscoelastic response characteristics. Regardless of the test type, the point of maximum shear stress in specimens consistently occurs prior to the point of maximum deformation, resulting in positive lead times.

## 4.1 Constant Rate Shear Deformation

Specimens loaded in constant rate deformation exhibit an shear stress increase during the constant rate deformation portion of the test. The point of maximum shear stress, $\sigma_{max}$, for all specimens occurs prior to the end of the constant rate deformation portion of the test, indicating a stress leading response and therefore positive lead times, $\Delta t$. During the constant deformation portion of the test, the stress decreases and reaches the relaxation stress 60 seconds after the time of maximum shear stress. The relaxation fraction, $RF$, is recorded (Eqn. 20) and represents the fraction of stress recovered. Tables 2 and 3 show the results for the constant rate groups. Table 4 shows the statistical results for the one-factor ANOVAs analyzing the constant rate groups.

The lead time exhibits no significant difference between the 1 mm/sec and 12 mm/sec porcine groups in the circumferential direction ($p = 0.906$), the 1 mm/sec and 12 mm/sec porcine groups in the longitudinal direction ($p = 0.176$), the circumferential and longitudinal porcine groups at 1 mm/sec ($p = 0.688$), or the circumferential and longitudinal porcine groups at 12 mm/sec ($p = 0.459$). However, the 1 mm/sec porcine groups generally appear to have shorter lead times than the 12 mm/sec porcine groups with few outliers (specimens cP2-m, cP2-l, and cP3-d) raising the average of the groups. These outliers yield high standard deviations for the 1 mm/sec circumferential (75.7 msec) and longitudinal (33.4 msec) groups compared to the 12 mm/sec circumferential (4.35 msec) and longitudinal (4.11 msec) groups.

This trend in the lead time indicates that longer lead times are more common for faster deformation rates.

The maximum shear stress, $\sigma_{max}$, statistical analyses shows that there is no significant difference between the 1 mm/sec and 12 mm/sec groups in the circumferential direction ($p = 0.091$), the 1 mm/sec and 12 mm/sec groups in the longitudinal direction ($p = 0.071$), the circumferential and longitudinal groups at 1 mm/sec ($p = 0.905$), or the circumferential and longitudinal groups at 12 mm/sec ($p = 0.755$).

Table 2: Constant rate shear deformation results for the 1 mm/sec group.

| Circumferential | | | | |
|---|---|---|---|---|
| Specimen | $\Delta t$ (msec) | $\sigma_{max}$ (kPa) | $\sigma_r$ (kPa) | $RF$ |
| cP1-b | 25.2 | 14.162 | 5.788 | 0.582 |
| cP1-d | 16.4 | 4.856 | 2.196 | 0.531 |
| cP1-f | 24.0 | 8.589 | 4.673 | 0.439 |
| cP2-i | 25.2 | 3.033 | 1.267 | 0.573 |
| cP2-k | 22.4 | 6.630 | 2.842 | 0.566 |
| cP2-m | 264 | 7.240 | 3.720 | 0.472 |
| cP3-c | 20.8 | 8.992 | 4.867 | 0.454 |
| cP3-e | 23.2 | 5.853 | 2.281 | 0.607 |
| cP4-f | 26.4 | 5.267 | 1.278 | 0.754 |
| cP4-h | 42.8 | 1.698 | 0.093 | 0.945 |
| AVG | 49.0 | 6.632 | 2.900 | 0.592 |
| STD | 75.7 | 3.486 | 1.828 | 0.154 |
| Longitudinal | | | | |
| Specimen | $\Delta t$ (msec) | $\sigma_{max}$ (kPa) | $\sigma_r$ (kPa) | $RF$ |
| cP1-a | 21.8 | 10.927 | 4.657 | 0.564 |
| cP1-c | 21.4 | 10.668 | 5.597 | 0.469 |
| cP1-e | 23.2 | 5.780 | 2.820 | 0.497 |
| cP2-h | 18.6 | 5.638 | 3.371 | 0.397 |
| cP2-j | 19.8 | 5.455 | 2.929 | 0.457 |
| cP2-l | 87.0 | 7.254 | 3.439 | 0.498 |
| cP3-b | 24.2 | 8.834 | 3.594 | 0.589 |
| cP3-d | 114 | 6.167 | 2.790 | 0.525 |
| cP4-e | 28.6 | 3.613 | 0.232 | 0.935 |
| cP4-g | 24.8 | 3.649 | 1.469 | 0.592 |
| AVG | 38.3 | 6.799 | 3.090 | 0.552 |
| STD | 33.4 | 2.604 | 1.498 | 0.148 |

There are once again trends showing that there are differences between the deformation rate groups, however. The average maximum shear stress for the 1 mm/sec circumferential (6.632 kPa) and longitudinal (6.799 kPa) groups are comparatively higher than the 12 mm/sec circumferential (5.100 kPa) and longitudinal (4.168 kPa) groups. The standard deviation for all groups is similar, ranging from 2.224 kPa (cP12C) to 3.468 kPa (cP1L).

The relaxation stress, $\sigma_r$, statistical analyses shows that there is a signifi-

Table 3: Constant rate shear deformation results for the 12 mm/sec group.

| Circumferential | | | | |
|---|---|---|---|---|
| Specimen | $\Delta t$ (msec) | $\sigma_{max}$ (kPa) | $\sigma_r$ (kPa) | $RF$ |
| cP2-b | 56.8 | 3.627 | 0.627 | 0.798 |
| cP2-d | 53.2 | 3.831 | 1.123 | 0.675 |
| cP2-g | 54.6 | 4.954 | 1.730 | 0.616 |
| cP3-g | 42.8 | 7.210 | 2.542 | 0.589 |
| cP3-i | 48.2 | 6.009 | 2.859 | 0.497 |
| cP3-k | 47.0 | 3.728 | 1.256 | 0.636 |
| cP4-b | 51.0 | 4.932 | 1.469 | 0.673 |
| cP4-d | 54.8 | 4.246 | 1.033 | 0.733 |
| cP5-b | 54.6 | 2.899 | 1.093 | 0.587 |
| cP5-d | 55.6 | 3.943 | 0.897 | 0.749 |
| AVG | 51.9 | 4.538 | 1.463 | 0.655 |
| STD | 4.52 | 1.280 | 0.722 | 0.089 |
| Longitudinal | | | | |
| Specimen | $\Delta t$ (msec) | $\sigma_{max}$ (kPa) | $\sigma_r$ (kPa) | $RF$ |
| cP2-a | 50.0 | 13.129 | 6.712 | 0.451 |
| cP2-c | 45.0 | 6.728 | 1.474 | 0.740 |
| cP2-e | 58.0 | 1.621 | 0.550 | 0.621 |
| cP3-f | 53.2 | 2.581 | 1.095 | 0.543 |
| cP3-h | 51.6 | 4.074 | 1.845 | 0.520 |
| cP3-j | 53.0 | 2.905 | 0.665 | 0.746 |
| cP4-a | 54.4 | 3.090 | 0.703 | 0.745 |
| cP4-c | 52.2 | 3.600 | 0.436 | 0.866 |
| cP5-a | 59.0 | 1.839 | 0.537 | 0.669 |
| cP5-c | 56.8 | 2.109 | 0.610 | 0.679 |
| AVG | 53.3 | 4.168 | 1.463 | 0.658 |
| STD | 4.11 | 3.474 | 1.901 | 0.126 |

Table 4: One-factor ANOVA results for constant rate shear deformation.

| Direction | Def. Rate (mm/sec) | $p$-value $\Delta t$ | $\sigma_{max}$ | $\sigma_r$ | $RF$ |
|---|---|---|---|---|---|
| Circ | **Factor** | 0.906 | 0.091 | 0.033 | 0.276 |
| Long | **Factor** | 0.176 | 0.071 | 0.048 | 0.102 |
| **Factor** | 1 | 0.688 | 0.905 | 0.803 | 0.562 |
| **Factor** | 12 | 0.459 | 0.755 | 1.000 | 0.959 |

cant difference between the 1 mm/sec and 12 mm/sec groups in the circumferential direction ($p = 0.033$) and the 1 mm/sec and 12 mm/sec groups in the longitudinal direction ($p = 0.048$). In contrast, there is no significant difference between the circumferential and longitudinal groups at 1 mm/sec ($p = 0.803$) or the circumferential and longitudinal groups at 12 mm/sec ($p = 1.000$). On average, the 1 mm/sec circumferential (2.900 kPa) and longitudinal (3.090 kPa) groups have higher relaxation stresses than in the 12 mm/sec circumferential (1.463 kPa) and longitudinal (1.463 kPa) groups. The standard deviation for all groups is similar, ranging from 0.722 kPa (cP12C) to 1.901 kPa (cP12L).

The $RF$ statistical analyses shows that there is no significant difference between the 1 mm/sec and 12 mm/sec groups in the circumferential direction ($p = 0.276$), the 1 mm/sec and 12 mm/sec groups in the longitudinal direction ($p = 0.102$), the circumferential and longitudinal groups at 1 mm/sec ($p = 0.562$), or the circumferential and longitudinal groups at 12 mm/sec ($p = 0.959$). However, the 1 mm/sec groups generally appear to have smaller $RF$ magnitudes than the 12 mm/sec groups with a few outliers (specimens cP4-h and cP4-e), raising the average of the 1 mm/sec groups. The 1 mm/sec groups more commonly yield $RF$ magnitudes in the range of 0.45 to 0.6, as compared to the 12 mm/sec groups that yield $RF$ magnitudes in the range of 0.55 to 0.75.

## 4.2 Sinusoidal Shear Deformation

All specimens loaded in sinusoidal shear exhibit the highest magnitude of total stress amplitude response in the first deformation cycle of the experiment. Because the deformation amplitude and frequency are constant throughout the experiment, any changes in stress show that different amounts of force are required from the shearing apparatus to generate the same deformation. After the first deformation cycle, both the total stress amplitude, $\sigma_A$, and the first harmonic, $\sigma_1$, decrease on each subsequent cycle until the aortic tissue enters a quasi-periodic state (Fig. 14a and 15). The decreases in the total stress amplitude indicate that the aortic tissue is damaged in the transient stage because there is less resistance to deformation. The specimens usually enter the quasi-periodic stress state within deformation cycle number 5. To ensure that all specimens have entered the quasi-periodic state, cycle 20 is conservatively chosen as the first quasi-periodic cycle for analyses.

The total stress amplitude remains relatively constant in the quasi-periodic state, yet there are instances where the total stress amplitude increases or decreases during the quasi-periodic state. However, the magnitude of the total stress amplitude changes in the quasi-periodic stress state are significantly smaller than the magnitude of the changes seen in the transient stress state. The total stress amplitude, stress harmonic amplitudes, IR amplitudes, and RR amplitudes from cycles 20 to 50 are averaged for analysis of each specimen to account for any discrepancies within the quasi-periodic cycles. Obtaining the average value yields one value for statistical analyses and guarantees that the value is representative of the true quasi-periodic value for each specimen within a group. One-factor ANOVAs compare all 11 quasi-periodic values between analyzed groups. Table 5a is provided to show trends for each specimen group in the quasi-periodic state. Notably, the porcine aortic tissue stress values are lower on average than human aortic tissue stress values (Table 5a). Tables 7, 8, 9, and 10 are displayed at the end of the Results section and show the quasi-

periodic value for each specimen within their respective groups. Table 6 is provided to show the results of all one-factor ANOVAs performed on sinusoidal quasi-periodic data.

The transient state is more difficult to quantify for statistical analyses, so

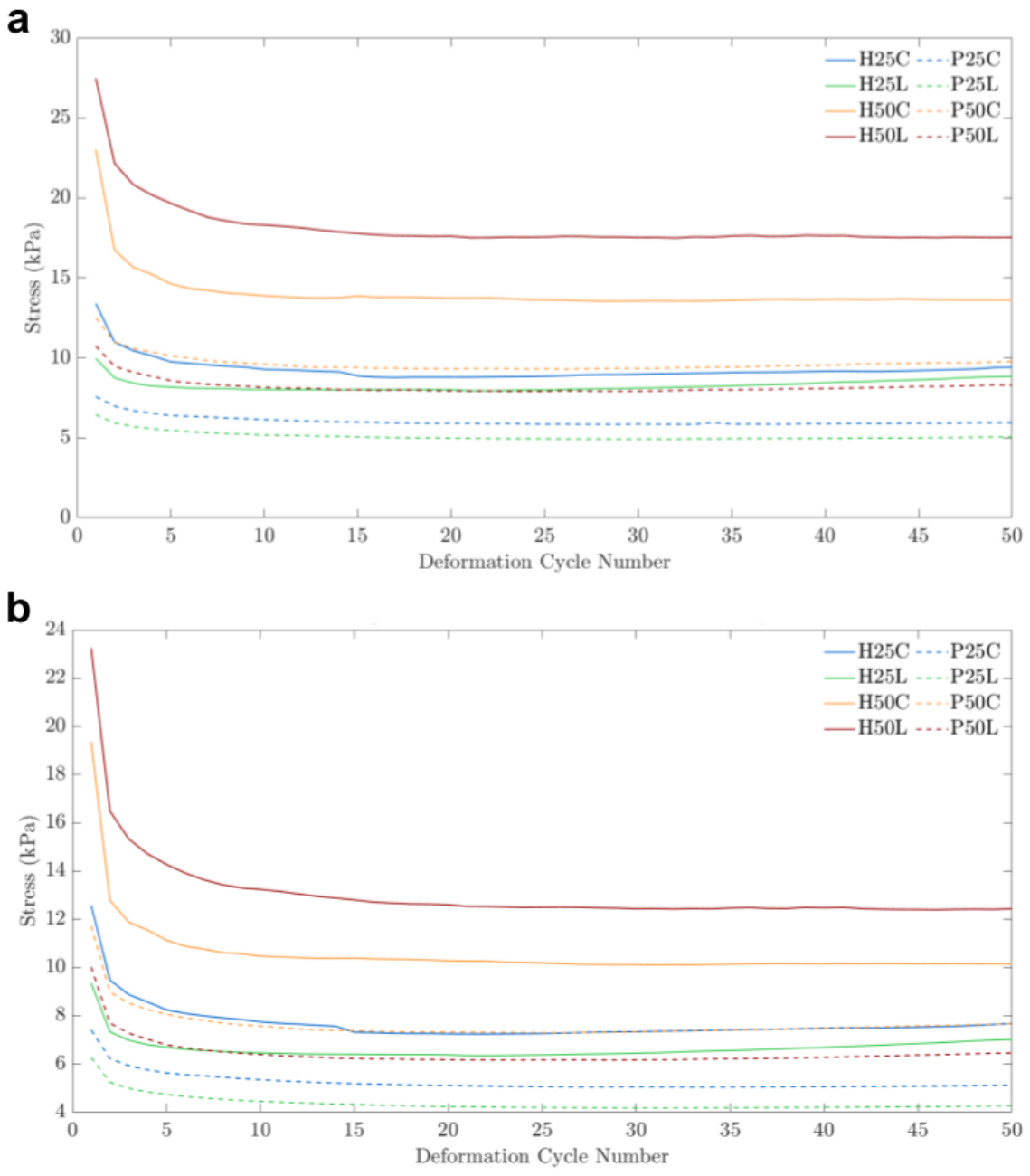


Figure 14: The average (a) amplitude $\sigma_A$ and (b) 1 Hz harmonic amplitude $\sigma_1$ on each deformation cycle for all specimen groups.

Figs. 14, 15, 16, and 17 are provided to demonstrate visual trends in the transient state for each specimen group. The figures display the average value of each specimen group for every cycle in the experiment. To provide comparative values for response trends in the transient stage, Table 5b shows the differences between deformation

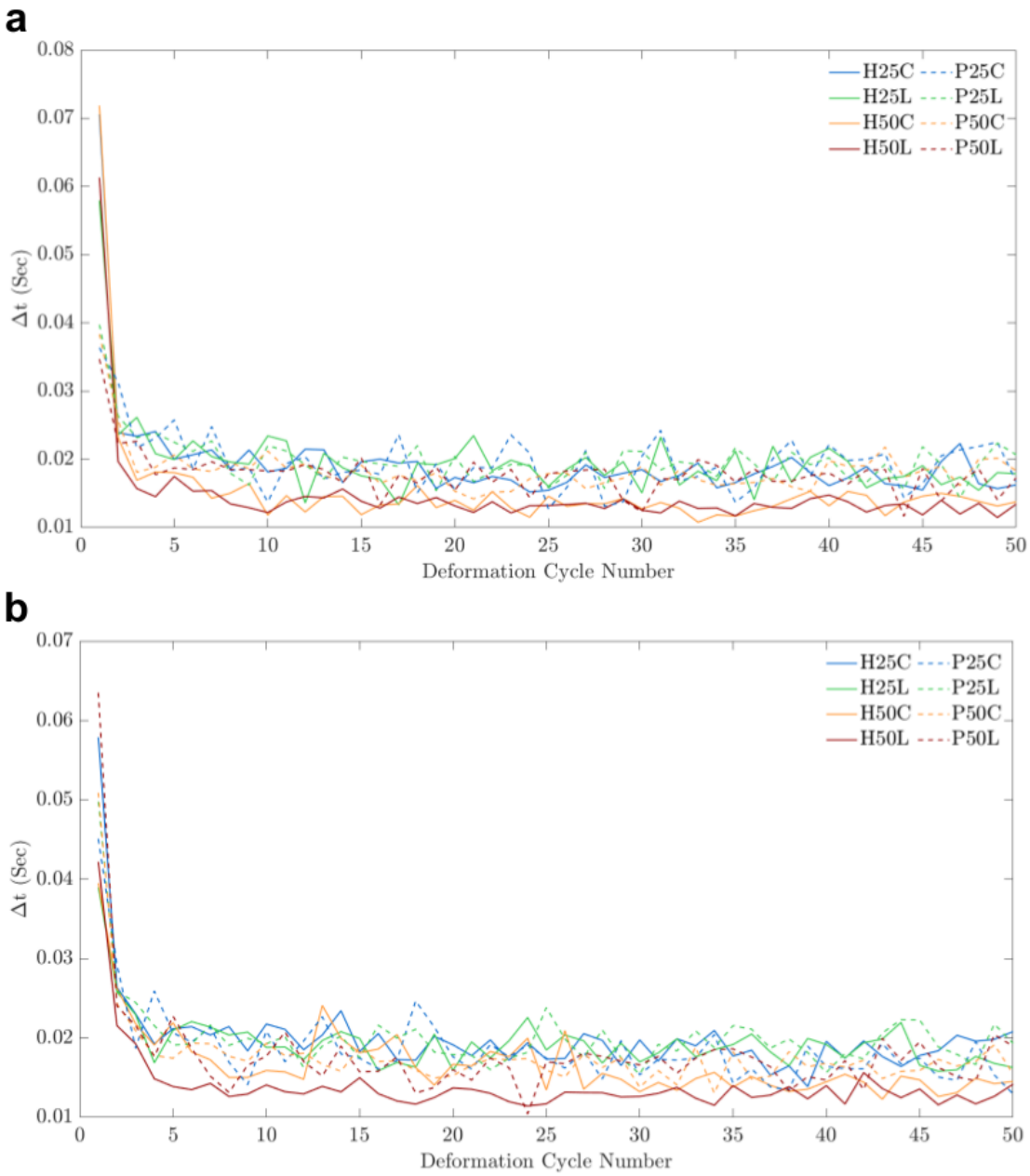


Figure 15: The average time difference between the (a) maximum value of stress and deformation and (b) minimum value of stress and deformation on each deformation cycle for all specimen groups.

Table 5: (a) Average and standard deviation values of cycles 20 to 50 for each specimen group. These values are the quasi-periodic values for each specimen group. (b) Average and standard deviation values of the difference between deformation cycles 1 and 2 for each specimen group.

(a) Quasi-Periodic

| | $\sigma_A$ (kPa) | | $\sigma_1$ (kPa) | | $\sigma_3$ (kPa) | | $\sigma_5$ (kPa) | | $IR$ | | $RR$ | |
|---|---|---|---|---|---|---|---|---|---|---|---|---|
| Group | AVG | SD | AVG | SD | AVG | SD | AVG | SD | AVG | SD | AVG | SD |
| H25C | 9.063 | 4.729 | 7.409 | 3.685 | 1.490 | 0.976 | 0.202 | 0.201 | 0.190 | 0.042 | 0.022 | 0.014 |
| H25L | 8.311 | 6.228 | 6.596 | 4.718 | 1.495 | 1.378 | 0.238 | 0.285 | 0.202 | 0.064 | 0.028 | 0.023 |
| H50C | 13.63 | 3.018 | 10.16 | 2.485 | 2.866 | 0.705 | 0.598 | 0.216 | 0.288 | 0.065 | 0.061 | 0.024 |
| H50L | 17.56 | 6.659 | 12.46 | 4.472 | 4.101 | 1.718 | 0.887 | 0.472 | 0.325 | 0.044 | 0.067 | 0.017 |
| P25C | 5.891 | 3.733 | 5.061 | 3.359 | 0.748 | 0.363 | 0.060 | 0.066 | 0.165 | 0.047 | 0.010 | 0.006 |
| P25L | 4.972 | 1.438 | 4.201 | 1.288 | 0.708 | 0.224 | 0.043 | 0.031 | 0.173 | 0.058 | 0.010 | 0.006 |
| P50C | 9.478 | 4.027 | 7.426 | 3.217 | 1.779 | 0.713 | 0.278 | 0.191 | 0.250 | 0.049 | 0.038 | 0.019 |
| P50L | 8.049 | 2.172 | 6.246 | 1.688 | 1.555 | 0.460 | 0.252 | 0.155 | 0.249 | 0.034 | 0.039 | 0.020 |

(b) Transient

| | $\Delta\sigma_A$ (kPa) | | $\Delta\sigma_1$ (kPa) | | $\Delta\sigma_3$ (kPa) | | $\Delta\sigma_5$ (kPa) | | $\Delta IR$ | | $\Delta RR$ | |
|---|---|---|---|---|---|---|---|---|---|---|---|---|
| Group | AVG | SD | AVG | SD | AVG | SD | AVG | SD | AVG | SD | AVG | SD |
| H25C | -2.415 | 4.074 | -3.103 | 4.064 | 0.542 | 0.367 | -0.742 | 1.337 | 0.091 | 0.020 | -0.038 | 0.023 |
| H25L | -1.203 | 1.536 | -2.020 | 2.154 | 0.678 | 0.484 | -0.359 | 0.333 | 0.107 | 0.024 | -0.031 | 0.009 |
| H50C | -6.266 | 7.943 | -6.591 | 5.771 | 0.330 | 2.158 | -0.460 | 0.429 | 0.115 | 0.072 | -0.009 | 0.016 |
| H50L | -5.312 | 3.437 | -6.774 | 4.090 | 1.029 | 0.899 | -0.412 | 0.379 | 0.123 | 0.035 | -0.004 | 0.014 |
| P25C | -0.594 | 0.290 | -1.190 | 0.640 | 0.494 | 0.243 | -0.245 | 0.186 | 0.090 | 0.016 | -0.029 | 0.007 |
| P25L | -0.516 | 0.186 | -1.036 | 0.316 | 0.475 | 0.168 | -0.204 | 0.054 | 0.096 | 0.028 | -0.031 | 0.004 |
| P50C | -1.506 | 0.808 | -2.738 | 1.082 | 0.926 | 0.343 | -0.400 | 0.135 | 0.133 | 0.029 | -0.029 | 0.007 |
| P50L | -1.263 | 0.626 | -2.329 | 0.769 | 0.861 | 0.286 | -0.374 | 0.114 | 0.134 | 0.026 | -0.032 | 0.009 |

cycle 1 and cycle 2 values. Negative values in Table 5b indicate that the value has decreased from cycle 1 to cycle 2.

The maximum and minimum values of stress nearly always occur before the maximum and minimum values of deformation (Fig. 15). This time difference indicates that the stress leads the response in the deformation controlled experiment. In the transient stage, the stress leading time difference is more pronounced, particularly in the first cycle. Regardless of tissue type, tissue direction, deformation amplitude, or deformation direction, the lead time $\Delta t$ for each group is consistently

within 10 to 30 milliseconds in the quasi-periodic state (Tables 7, 8, 9, and 10). In all quasi-periodic statistical analyses, the only significant differences are seen between the human and porcine 50% deformation groups ($p = 0.014$), 25% and 50% human circumferential groups ($p = 0.022$), and the 25% and 50% human longitudinal groups ($p$ = 1.18e-4). The average time difference is wider ranging in the transient stage; however, for most specimens the lead time $\Delta t$ ranges from 30 to 70 milliseconds.

The total stress amplitude in the quasi-periodic state varies when analyz-

Table 6: One-factor ANOVA results for sinusoidal shear deformation.

| | | | $p$-value | | |
|---|---|---|---|---|---|
| Tissue | Direction | Def. Amp. (%) | $IR$ | $RR$ | $\Delta t$ |
| **Factor** | Circ | 25 | 0.206 | 0.012 | 0.890 |
| **Factor** | Long | 25 | 0.280 | 0.018 | 0.694 |
| **Factor** | Circ | 50 | 0.146 | 0.024 | 0.082 |
| **Factor** | Long | 50 | 2.04e-4 | 1.95e-3 | 0.014 |
| Human | **Factor** | 25 | 0.616 | 0.494 | 0.681 |
| Human | **Factor** | 50 | 0.136 | 0.441 | 0.379 |
| Porcine | **Factor** | 25 | 0.734 | 0.969 | 0.386 |
| Porcine | **Factor** | 50 | 0.960 | 0.956 | 0.950 |
| Human | Circ | **Factor** | 4.57e-4 | 1.62e-4 | 0.022 |
| Human | Long | **Factor** | 3.71e-5 | 1.56e-4 | 1.18e-4 |
| Porcine | Circ | **Factor** | 4.74e-4 | 8.36e-5 | 0.555 |
| Porcine | Long | **Factor** | 1.09e-3 | 1.79e-4 | 0.165 |

| | | | $p$-value | | | |
|---|---|---|---|---|---|---|
| Tissue | Direction | Def. Amp. (%) | $\sigma_A$ | $\sigma_1$ | $\sigma_3$ | $\sigma_5$ |
| **Factor** | Circ | 25 | 0.096 | 0.134 | 0.028 | 0.038 |
| **Factor** | Long | 25 | 0.099 | 0.120 | 0.076 | 0.036 |
| **Factor** | Circ | 50 | 0.013 | 0.037 | 1.81e-3 | 1.48e-3 |
| **Factor** | Long | 50 | 2.16e-4 | 3.40e-4 | 1.24e-4 | 3.99e-4 |
| Human | **Factor** | 25 | 0.753 | 0.657 | 0.992 | 0.741 |
| Human | **Factor** | 50 | 0.090 | 0.152 | 0.039 | 0.079 |
| Porcine | **Factor** | 25 | 0.455 | 0.437 | 0.761 | 0.444 |
| Porcine | **Factor** | 50 | 0.313 | 0.294 | 0.392 | 0.726 |
| Human | Circ | **Factor** | 0.014 | 0.053 | 1.15e-3 | 2.51e-4 |
| Human | Long | **Factor** | 3.07e-3 | 7.21e-3 | 8.39e-4 | 8.73e-4 |
| Porcine | Circ | **Factor** | 0.043 | 0.107 | 3.70e-4 | 1.87e-3 |
| Porcine | Long | **Factor** | 8.52e-4 | 4.56e-3 | 2.23e-5 | 2.98e-4 |

ing numerous factors. In these experiments, tissue type, deformation direction, and deformation amplitude are analyzed. Statistically, the effect of deformation direction on the total stress amplitude does not create any significant differences between groups with $p$-values ranging from 0.090 to 0.753 (Table 6). The effect of deformation amplitude on the total stress amplitude creates significant differences between all group with $p$-values ranging from 8.52e-4 to 0.043 (Table 6). For tissue type, the porcine and human 50% deformation groups have significantly different total stress amplitudes ($p = 0.013$ for circumferential and $p = 2.16\text{e-}4$ for longitudinal) while the 25% deformation groups are not significantly different ($p = 0.096$ for circumferential and $p = 0.099$ for longitudinal).

### 4.2.1 Frequency Components of Shear Stress

The one-sided power spectrum of each test is found using the MATLAB FFT function and Eqn. 10. Commonly, the most significant frequencies contained within the stress response are the 1 Hz, 3 Hz, and 5 Hz frequencies. The coefficients of the frequency components for each deformation cycle of the shear stress response are computed using the MATLAB function "trapz" to integrate Eqn. 19. In general, porcine aortic tissue specimens have lower amplitudes of stress harmonics than human specimens with the same deformation magnitudes and tissue directions (Fig. 14 and 16). Specimens deformed at a 50% deformation amplitude also have larger average amplitudes of stress harmonics than specimens deformed at a 25% deformation amplitude. Statistically, the stress harmonics of 50% deformation specimens are almost always significantly larger than 25% deformation specimens with $p$-values ranging from 2.23e-5 to 0.107. The only comparisons that produce non-significantly different stress harmonics at different deformation amplitudes are the 1 Hz circumferential human comparison ($p = 0.053$) and the 1 Hz circumferential porcine comparison ($p = 0.107$). All other comparisons analyzing deformation amplitude for the 1 Hz, 3 Hz, and 5 Hz harmonics are significantly different.

With a 1 Hz deformation frequency, the 1 Hz harmonic is the largest in magnitude for the shear stress response of all specimens across all cycles (Table 5a). The transient region of the 1 Hz harmonic often decreases in amplitude until a quasi-periodic value is reached (Fig. 14a). Like the total shear stress amplitude response, there are instances where the 1 Hz harmonic increases or decreases in the quasi-periodic region. However, these changes in magnitude are significantly smaller than those that occur in the transient region. In the transition from deformation cycle 1 to cycle 2, all specimens exhibit an amplitude decrease in the 1 Hz harmonic (Fig. 14a). Human specimen groups have higher magnitudes of decrease in this transition than porcine specimen groups with the same deformation amplitude and tissue direction (Table 5b). When the aortic tissue response becomes quasi-periodic, the human specimen groups also have higher average amplitudes of the 1 Hz harmonic than porcine specimen groups with the same deformation amplitude and tissue direction (Table 5a). Comparative $p$-values analyzing the effect of tissue type range from 3.40e-4 to 0.099 (Table 6)

The 3 Hz harmonic is the second largest harmonic in magnitude for the shear stress response of specimens (Table 5a). Unlike other harmonics, the transient region of the 3 Hz harmonic generally increases in magnitude until a quasi-periodic amplitude is reached (Fig. 16a). For 50% deformation human specimen groups, the shape of the transient region differs from other specimen groups. The 50% deformation human specimen groups show a decrease in the magnitude of the 3 Hz harmonic after the initial increase from deformation cycle 1 to 2. Across all 88 specimens, only 4 specimens showed a decrease in the amplitude of the 3 Hz harmonic during the transition from deformation cycle 1 to 2. All 4 of these specimens originated from human aortic tissue, and 3 of the 4 occurred at a 50% deformation amplitude. The average magnitudes of the increase in the 3 Hz harmonic from deformation cycle 1 to 2 are somewhat similar regardless of the tissue type, however, human specimen

groups have a higher standard deviation than porcine specimen groups (Table 5b). When the aortic tissue response becomes quasi-periodic, the human specimen groups have higher average amplitudes of the 3 Hz harmonic than porcine specimen groups with the same deformation amplitude and tissue direction (Table 5a). Comparative

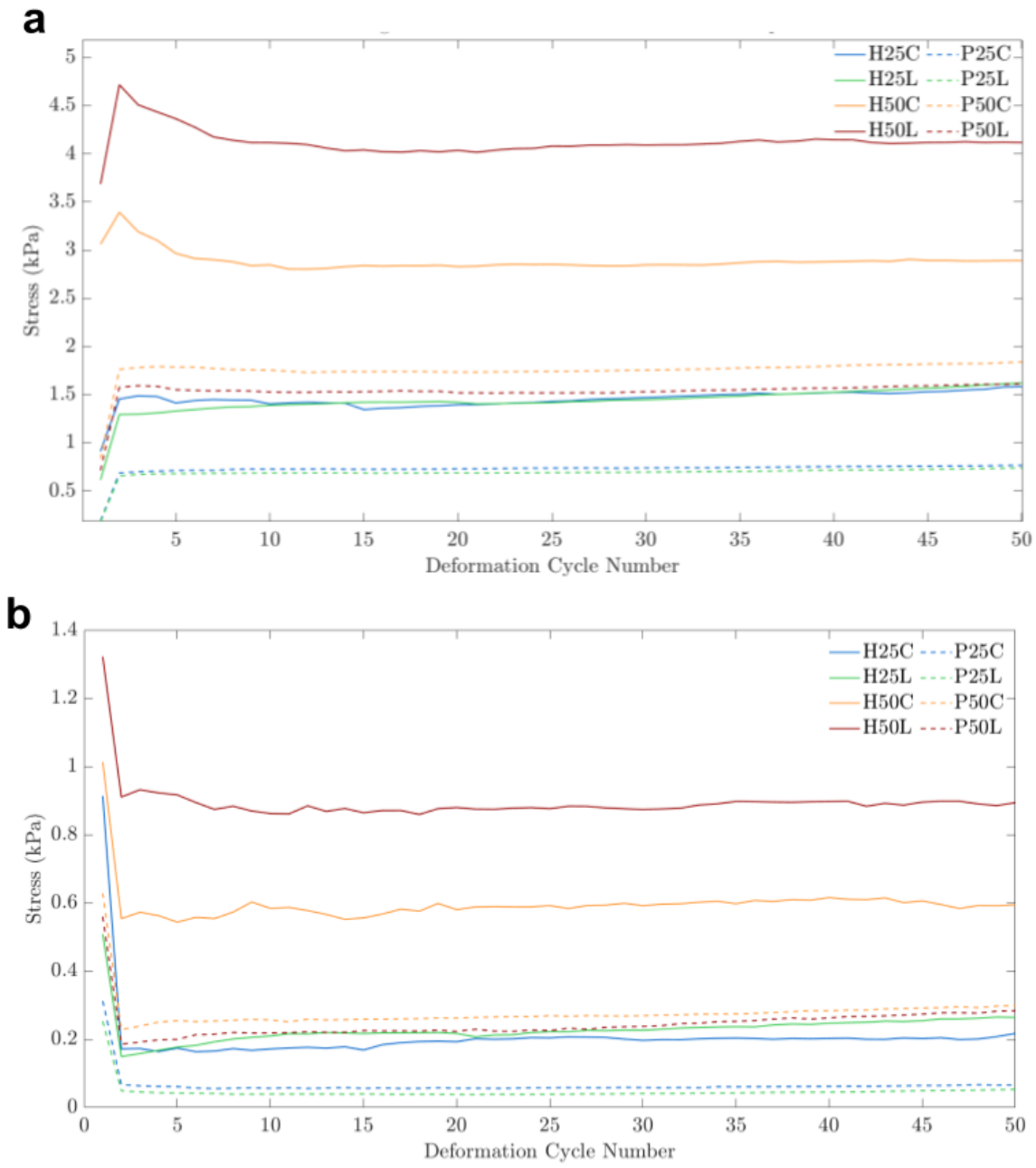


Figure 16: The average (a) 3 Hz harmonic and (b) 5 Hz harmonic magnitudes across all of the 50 deformation cycles for each specimen group.

$p$-values analyzing the effect of tissue type range from 1.24e-4 to 0.076 (Table 6)

The 5 Hz harmonic is the smallest in magnitude of the 1 Hz, 3 Hz, and 5 Hz harmonics of the shear stress response for all specimens (Table 5a). The transient region of the 5 Hz harmonic decreases in amplitude until a quasi-periodic amplitude is reached (Fig. 16b). Although the shape of the transient region is similar to the 1 Hz harmonic, the 5 Hz harmonic reaches its quasi-periodic amplitude in fewer cycles than the 1 Hz harmonic. The 5 Hz harmonic quasi-periodic amplitude is often reached by deformation cycle 3 after the initial decrease from cycle 1 to 2. 2 specimens exhibited an increase in the 5 Hz harmonic amplitude during the transition from deformation cycle 1 to cycle 2, both of which originating from human aortic tissue with a 50% deformation amplitude. On average, human specimen groups exhibit larger decreases in the 5 Hz harmonic amplitude during the cycle 1 to cycle 2 transition than porcine specimen groups with the same deformation amplitude and tissue direction (Table 5b). When the aortic tissue response becomes periodic, the human specimen groups have higher average magnitudes of the 5 Hz harmonic than porcine specimen groups with the same deformation amplitude and tissue direction (Table 5a). Comparative $p$-values analyzing the effect of tissue type range from 3.99e-4 to 0.038 (Table 6)

### 4.2.2 Interaction and Roughness Ratios

Using the frequency components extracted from each deformation cycle, $IR$ and $RR$ amplitudes are calculated for each deformation cycle. The $IR$ and $RR$ yield a dimensionless value for more specific comparisons of material properties contained within specimens. $IR$ measures the relative magnitude of fluid-solid interaction within the aortic tissue and $RR$ measures the relative smoothness of the shear stress response. These values are useful because they have a physical meaning that does not rely on total stress magnitudes. In aortic tissue, it is difficult to make conclusions based on total stress magnitudes due to the myriad of factors that impact the mechanical response of aortic tissues. All statistical results comparing quasi-periodic $IR$ and

$RR$ amplitudes are listed in Table 6. Figures 18, 19, 20, 21, 22, 23, 24, and 25 are displayed at the end of the Results section to show the $IR$ and $RR$ values for all specimens on each deformation cycle throughout the sinusoidal tests.

The $IR$ amplitude is on the order of 6 to 12 times larger than the $RR$ on average (Table 5a). The $IR$ amplitude increases in the transient region until it reaches its quasi-periodic value wherein the magnitude becomes relatively constant (Fig. 17). In the transition from deformation cycle 1 to cycle 2, all specimens exhibited an increase in the $IR$ magnitude except for one specimen in the human 50% deformation circumferential group (Fig. 19a). At 25% deformation, human and porcine tissue have similar average changes in the $IR$ amplitude during this transition (Table 5b). At 50% deformation, porcine tissues have higher average increases in the $IR$ amplitude during this transition. Once quasi-periodicity is reached, porcine specimens have lower average $IR$ magnitudes than human specimens with the same deformation amplitude and tissue direction (Table 5a).

Comparatively, there is not a significant difference in the quasi-periodic $IR$ amplitude between human and porcine aortic tissue deformed at a 25% deformation amplitude in the circumferential direction ($p = 0.206$) or the longitudinal direction ($p = 0.280$). At a 50% deformation amplitude, there is not a significant difference in the quasi-periodic $IR$ amplitude between porcine and human aortic tissue in the circumferential direction ($p = 0.146$). However, there is a significant difference in the quasi-periodic $IR$ amplitude between porcine and human aortic tissue in the longitudinal direction ($p = 2.030\text{e-}4$). For human aortic tissue, there is no significant difference in the quasi-periodic $IR$ amplitude between the circumferential and longitudinal directions for specimens deformed at a 25% deformation amplitude ($p = 0.616$) or a 50% deformation amplitude ($p = 0.135$). For porcine aortic tissue, there is no significant difference in the quasi-periodic $IR$ amplitude between the circumferential and longitudinal directions for specimens deformed at a 25% deformation

amplitude ($p = 0.735$) or a 50% deformation amplitude ($p = 0.960$).

The *RR* amplitude for individual specimens generally does not contain the smooth curves that are seen for *IR* across the 50 cycle experiment (Fig. 17, 22, 23, 24, and 25). However, in the initial transition from deformation cycle 1 to cycle 2,

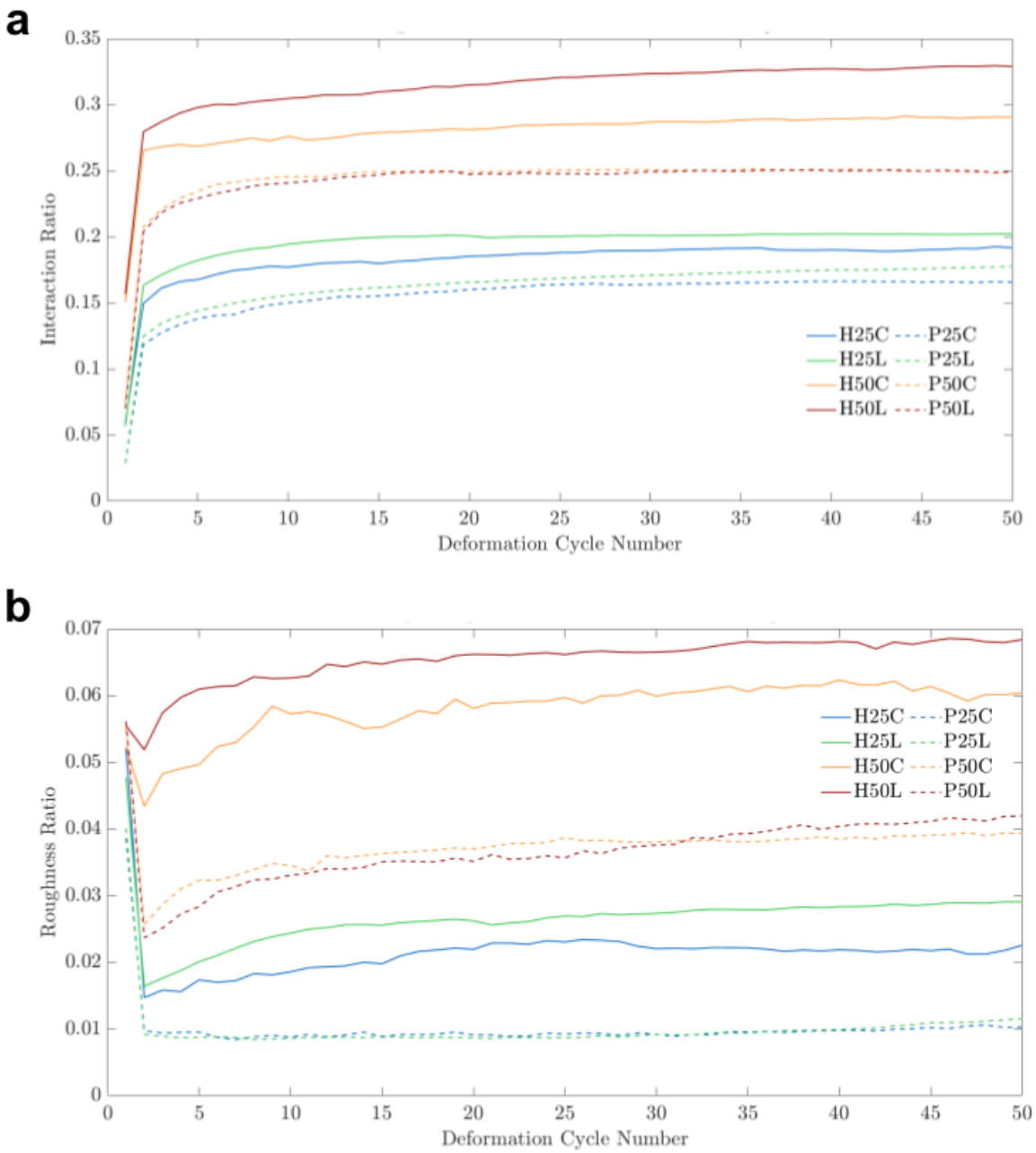


Figure 17: Average (a) Interaction Ratio and (b) Roughness Ratio on each deformation cycle for each specimen group.

a consistent decrease in the $RR$ magnitude is seen in specimens. Only 5 specimens exhibited an increase in $RR$ magnitude in the initial transition, all of which originated from the human 50% deformation groups (Fig. 23). In the human 50% deformation groups, $RR$ values decreased significantly less than all other specimen groups on average during the initial transition (Table 5b). Once quasi-periodicity is reached, porcine specimens have lower average $RR$ amplitudes than human specimens with the same deformation amplitude and tissue direction (Table 5a).

There is a significant difference in the quasi-periodic $RR$ amplitude between human and porcine aortic tissue deformed at a 25% deformation amplitude in the circumferential direction ($p = 0.012$) and the longitudinal direction ($p = 0.018$). Again, at a 50% deformation amplitude, there is a significant difference in the quasi-periodic $RR$ amplitude between porcine and human aortic tissue in both the circumferential direction ($p = 0.024$) and the longitudinal direction ($p = 1.945\text{e-}3$). For human aortic tissue, there is no significant difference in the quasi-periodic $RR$ amplitude between the circumferential and longitudinal directions for specimens deformed at a 25% deformation amplitude ($p = 0.494$) or a 50% deformation amplitude ($p = 0.441$). For porcine aortic tissue, there is no significant difference in the quasi-periodic $RR$ amplitude between the circumferential and longitudinal directions for specimens deformed at a 25% deformation amplitude ($p = 0.966$) or a 50% deformation amplitude ($p = 0.956$).

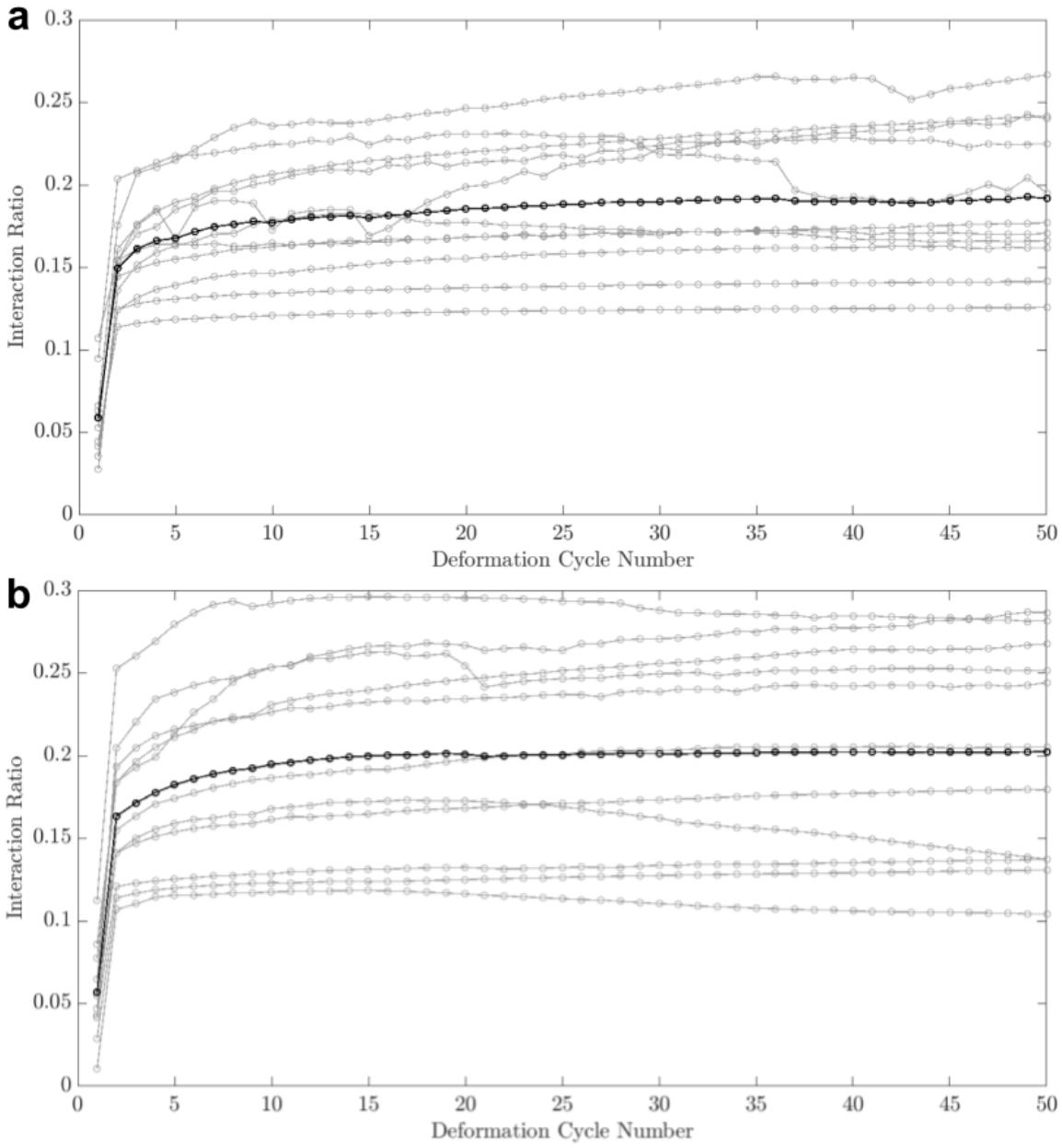


Figure 18: Interaction ratio on each deformation cycle for each specimen in the Human 25% deformation (a) Circumferential and (b) Longitudinal groups. The average Interaction Ratio for the group is denoted by the darkest plotted line. Each dot represents the value for a single cycle.

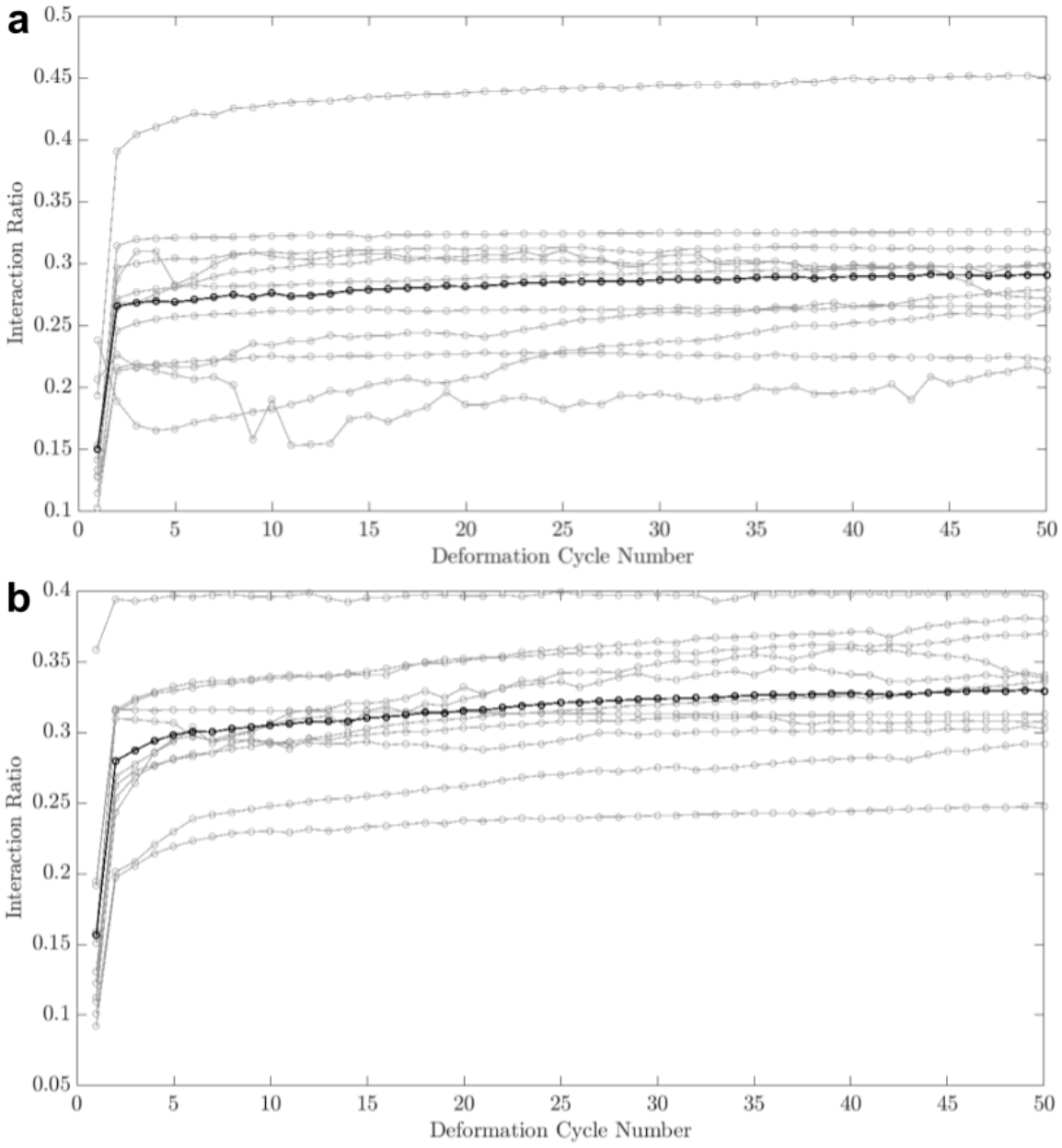


Figure 19: Interaction ratio on each deformation cycle for each specimen in the Human 50% deformation (a) Circumferential and (b) Longitudinal groups. The average Interaction Ratio for the group is denoted by the darkest plotted line. Each dot represents the value for a single cycle.

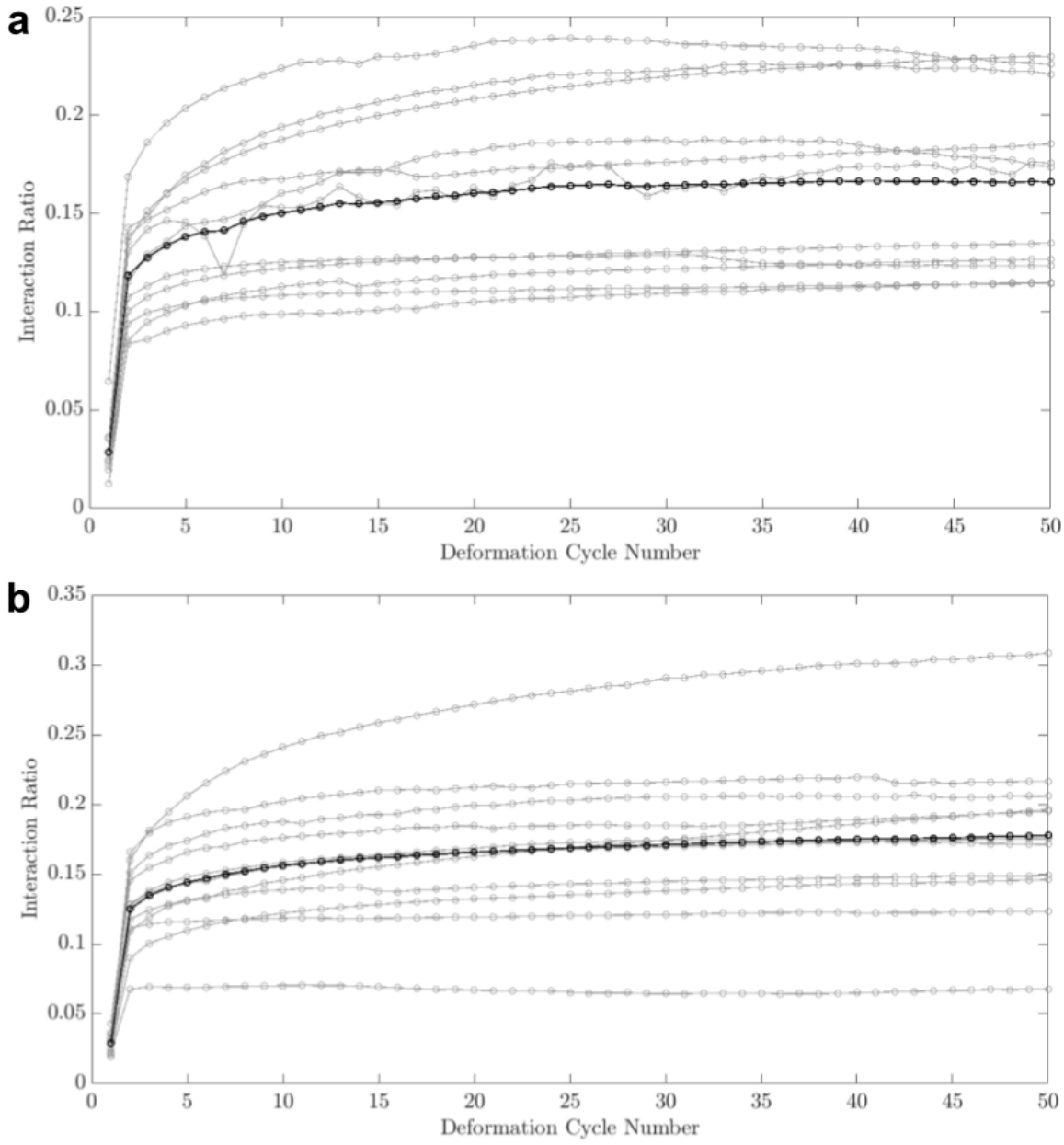


Figure 20: Interaction ratio on each deformation cycle for each specimen in the Porcine 25% deformation (a) Circumferential and (b) Longitudinal groups. The average Interaction Ratio on each deformation cycle for the group is denoted by the darkest plotted line. Each dot represents the value for a single cycle.

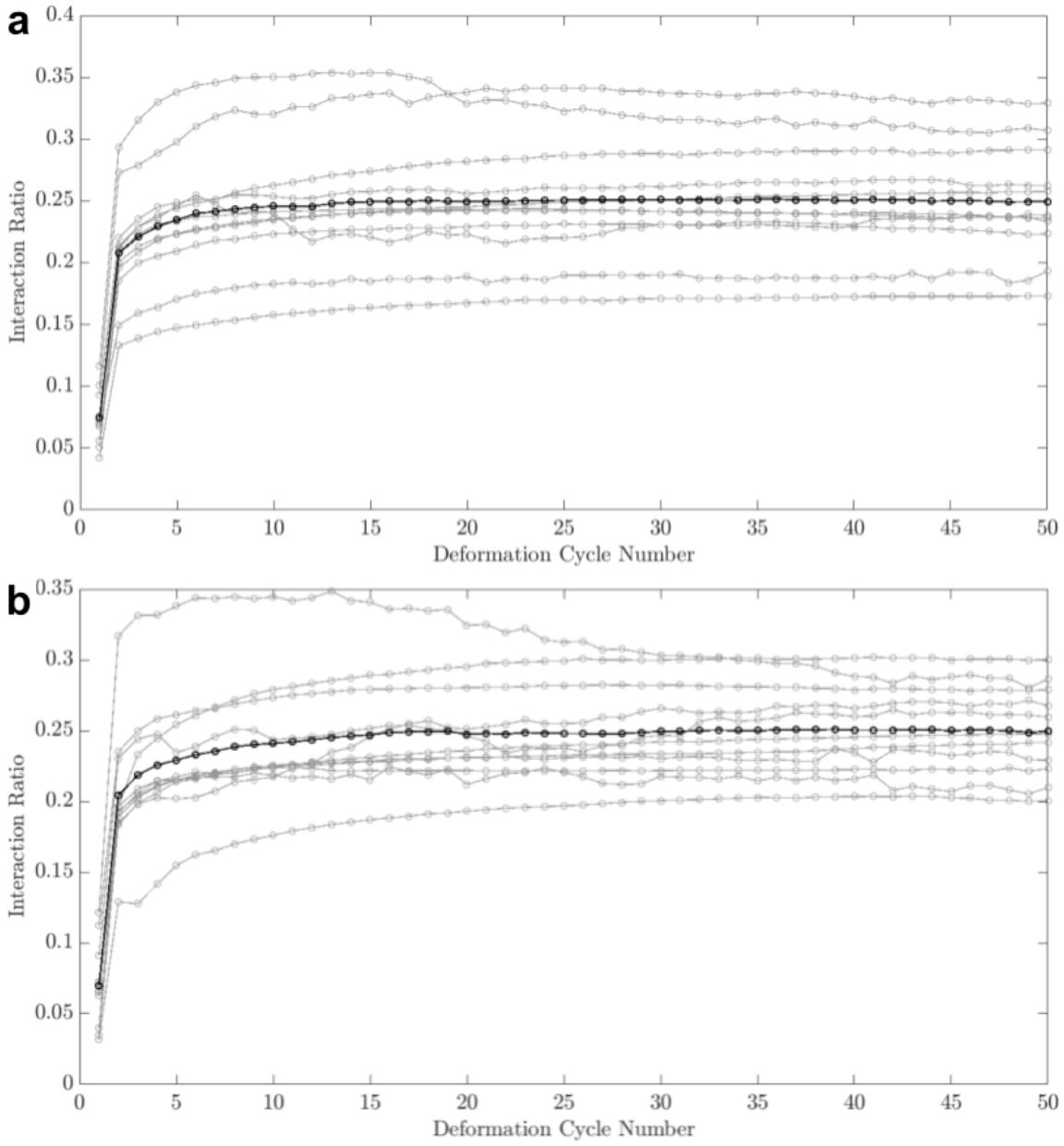


Figure 21: Interaction ratio on each deformation cycle for each specimen in the Porcine 50% deformation (a) Circumferential and (b) Longitudinal groups. The average Interaction Ratio on each deformation cycle for the group is denoted by the darkest plotted line. Each dot represents the value for a single cycle.

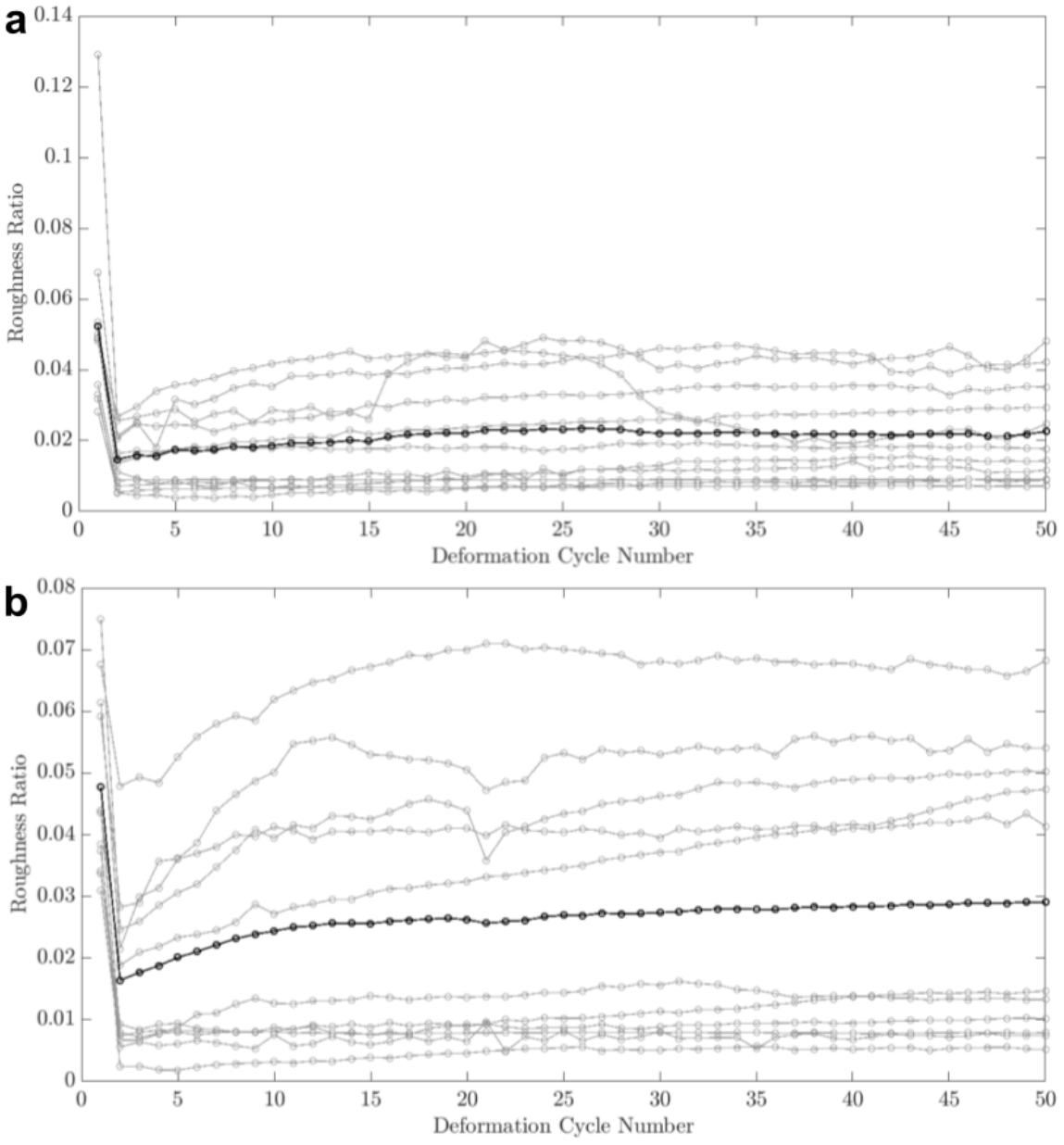


Figure 22: Roughness ratio on each deformation cycle for each specimen in the Human 25% deformation (a) Circumferential and (b) Longitudinal groups. The average Roughness Ratio on each deformation cycle for the group is denoted by the darkest plotted line. Each dot represents the value for a single cycle.

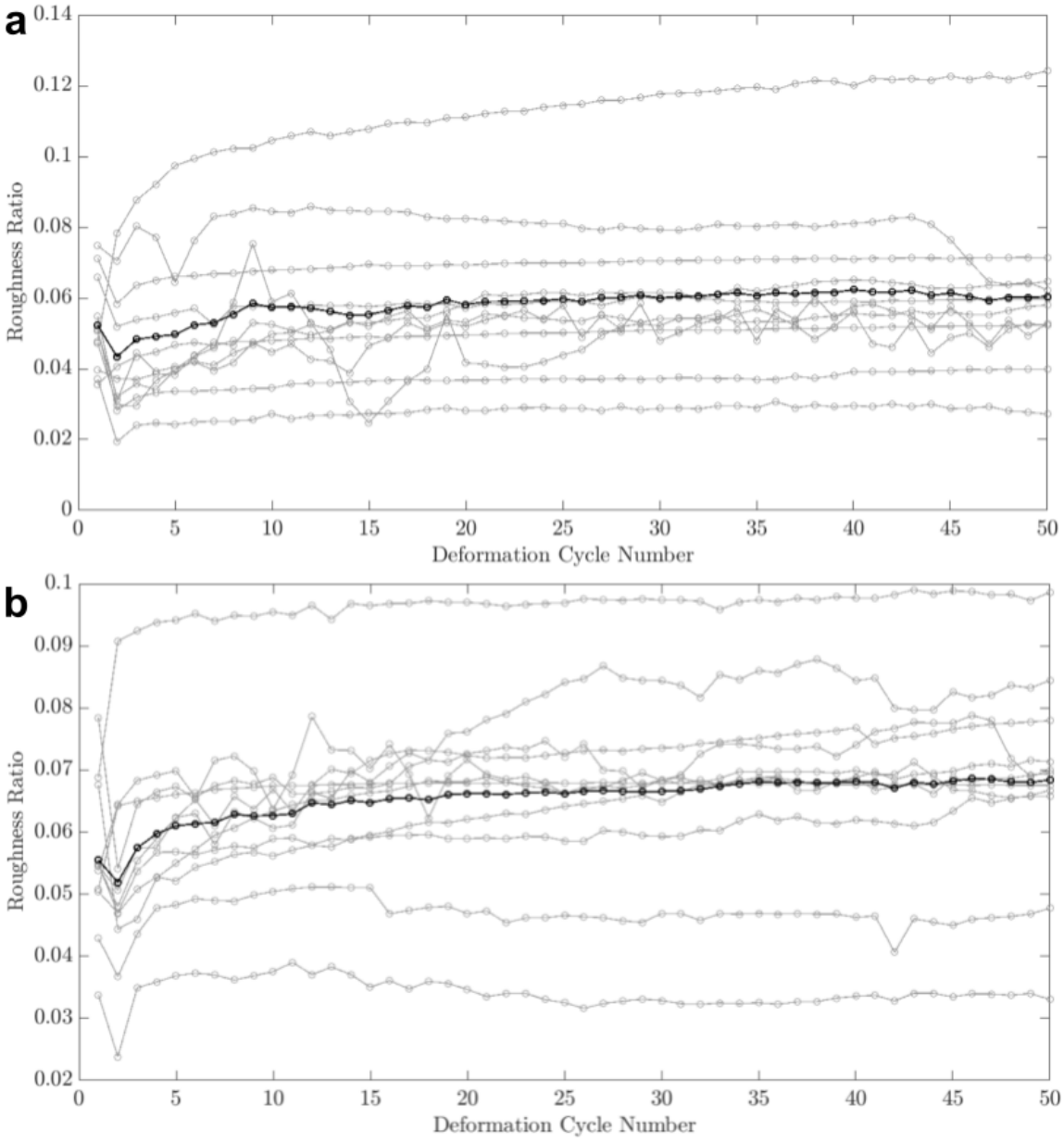


Figure 23: Roughness ratio on each deformation cycle for each specimen in the Human 50% deformation (a) Circumferential and (b) Longitudinal groups. The average Roughness Ratio on each deformation cycle for the group is denoted by the darkest plotted line. Each dot represents the value for a single cycle.

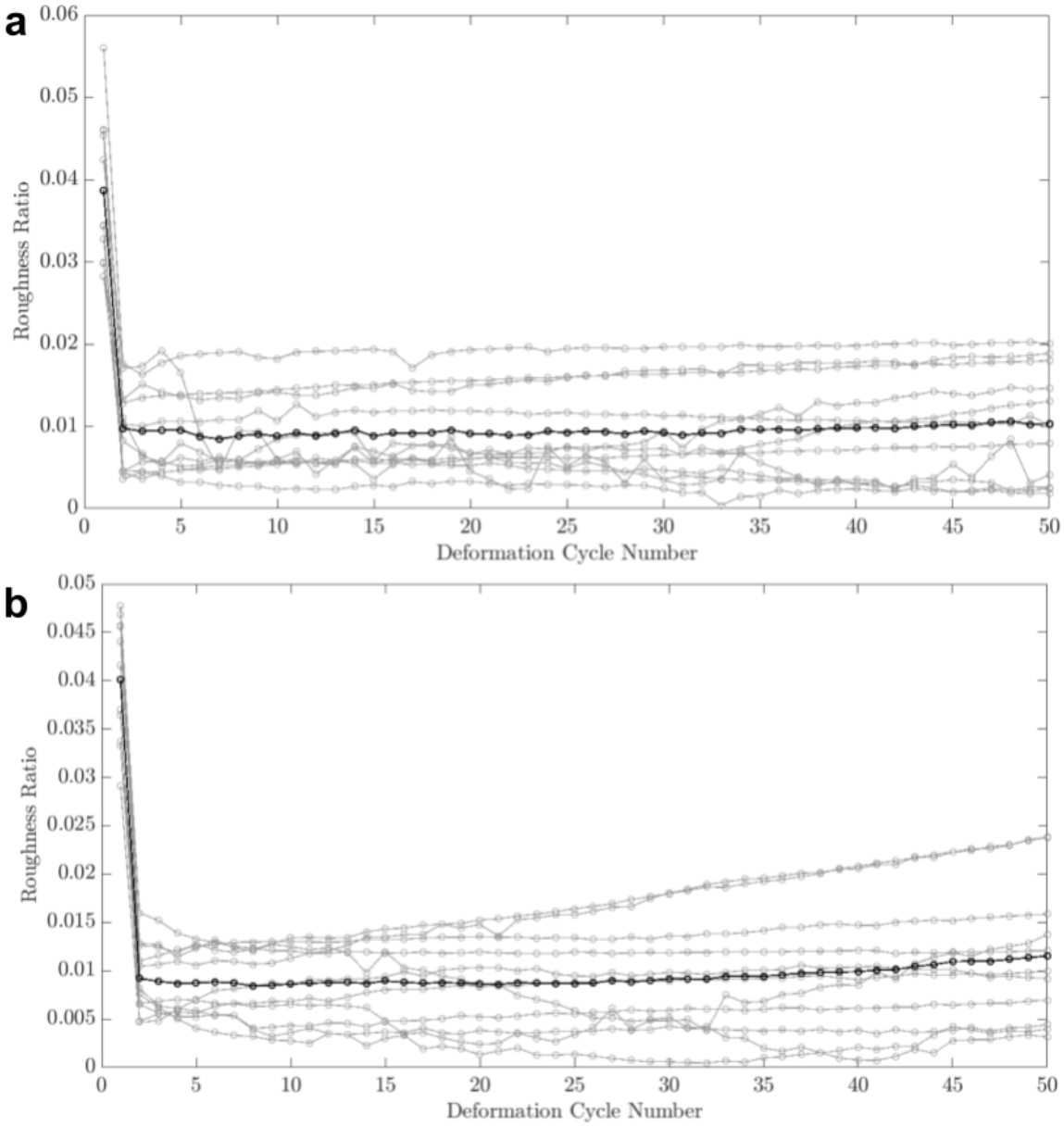


Figure 24: Roughness ratio across on each deformation cycle for each specimen in the Porcine 25% deformation (a) Circumferential and (b) Longitudinal groups. The average Roughness Ratio on each deformation cycle for the group is denoted by the darkest plotted line. Each dot represents the value for a single cycle.

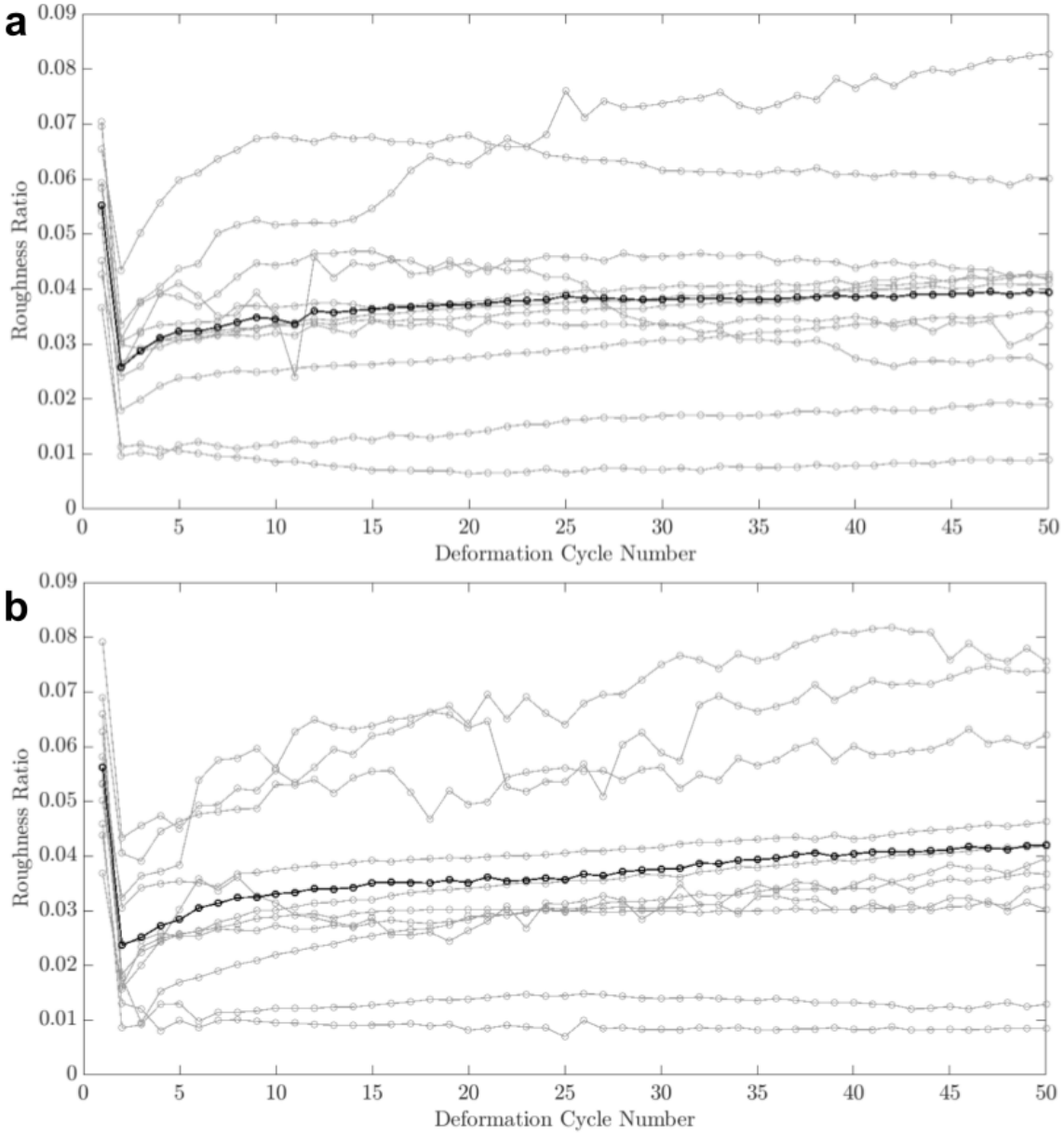


Figure 25: Roughness ratio on each deformation cycle for each specimen in the Porcine 50% deformation (a) Circumferential and (b) Longitudinal groups. The average Roughness Ratio on each deformation cycle for the group is denoted by the darkest plotted line. Each dot represents the value for a single cycle.

Table 7: The average total stress amplitude, 1 Hz harmonic, 3 Hz harmonic, 5 Hz harmonic, Interaction Ratio, Roughness Ratio, and lead time on deformation cycles 20 through 50 for each specimen in the Human 25% deformation group.

| Circumferential | | | | | | | |
|---|---|---|---|---|---|---|---|
| Specimen | $\sigma_A$ (kPa) | $\sigma_1$ (kPa) | $\sigma_3$ (kPa) | $\sigma_5$ (kPa) | $IR$ | $RR$ | $\Delta t$ (msec) |
| H4-m | 8.789 | 7.758 | 0.967 | 0.055 | 0.1246 | 0.0070 | 13.05 |
| H4-o | 8.086 | 7.025 | 0.983 | 0.063 | 0.1399 | 0.0089 | 12.74 |
| H6-b | 3.051 | 2.567 | 0.412 | 0.020 | 0.1605 | 0.0080 | 19.59 |
| H6-d | 3.493 | 2.924 | 0.499 | 0.034 | 0.1706 | 0.0117 | 16.31 |
| H6-f | 4.405 | 3.733 | 0.636 | 0.050 | 0.1704 | 0.0134 | 23.98 |
| H7-b | 9.295 | 7.419 | 1.719 | 0.199 | 0.2315 | 0.0268 | 19.08 |
| H7-d | 7.884 | 6.570 | 1.133 | 0.120 | 0.1725 | 0.0183 | 17.77 |
| H7-f | 7.917 | 6.417 | 1.357 | 1.890 | 0.2107 | 0.0289 | 20.40 |
| H8-a | 14.15 | 10.90 | 2.820 | 0.470 | 0.2585 | 0.0431 | 18.06 |
| H8-c | 16.33 | 13.06 | 2.927 | 0.576 | 0.2241 | 0.0441 | 16.62 |
| H8-e | 16.29 | 13.13 | 2.935 | 0.450 | 0.2233 | 0.0342 | 19.51 |
| AVG | 9.063 | 7.409 | 1.490 | 0.202 | 0.1897 | 0.0222 | 17.92 |
| SD | 4.729 | 3.685 | 0.967 | 0.201 | 0.0422 | 0.0139 | 3.555 |
| Longitudinal | | | | | | | |
| Specimen | $\sigma_A$ (kPa) | $\sigma_1$ (kPa) | $\sigma_3$ (kPa) | $\sigma_5$ (kPa) | $IR$ | $RR$ | $\Delta t$ (msec) |
| H4-n | 6.446 | 5.662 | 0.726 | 0.045 | 0.1282 | 0.0079 | 14.20 |
| H6-a | 3.339 | 2.920 | 0.317 | 0.015 | 0.1089 | 0.0053 | 23.08 |
| H6-c | 3.188 | 2.713 | 0.421 | 0.039 | 0.1561 | 0.0142 | 19.58 |
| H6-e | 2.919 | 2.417 | 0.423 | 0.023 | 0.1749 | 0.0094 | 21.66 |
| H6-l | 6.081 | 4.440 | 1.277 | 0.304 | 0.2873 | 0.0684 | 20.43 |
| H7-a | 7.106 | 5.828 | 1.187 | 0.071 | 0.2036 | 0.0122 | 16.59 |
| H7-c | 21.86 | 16.74 | 4.600 | 0.896 | 0.2745 | 0.0535 | 18.59 |
| H7-e | 9.960 | 7.720 | 1.998 | 0.307 | 0.2586 | 0.0396 | 19.45 |
| H8-b | 8.576 | 6.597 | 1.649 | 0.309 | 0.2499 | 0.0468 | 17.67 |
| H8-d | 17.95 | 14.10 | 3.385 | 0.580 | 0.2400 | 0.0411 | 17.59 |
| H8-f | 3.991 | 3.424 | 0.460 | 0.025 | 0.1343 | 0.0072 | 14.19 |
| AVG | 8.311 | 6.596 | 1.495 | 0.238 | 0.2015 | 0.0278 | 18.46 |
| SD | 6.228 | 4.718 | 1.378 | 0.285 | 0.0640 | 0.0225 | 3.129 |

Table 8: The average total stress amplitude, 1 Hz harmonic, 3 Hz harmonic, 5 Hz harmonic, Interaction Ratio, Roughness Ratio, and lead time on deformation cycles 20 through 50 for each specimen in the Human 50% deformation group.

| Circumferential | | | | | | | |
|---|---|---|---|---|---|---|---|
| Specimen | $\sigma_A$ (kPa) | $\sigma_1$ (kPa) | $\sigma_3$ (kPa) | $\sigma_5$ (kPa) | $IR$ | $RR$ | $\Delta t$ (msec) |
| H1-a | 12.89 | 10.38 | 2.041 | 0.530 | 0.1968 | 0.0512 | 17.44 |
| H2-d | 15.68 | 11.61 | 3.412 | 0.593 | 0.2940 | 0.0511 | 11.44 |
| H2-f | 9.244 | 6.534 | 2.123 | 0.462 | 0.3249 | 0.0707 | 10.01 |
| H2-h | 16.03 | 12.78 | 2.885 | 0.370 | 0.2258 | 0.0290 | 13.42 |
| H2-j | 13.32 | 8.476 | 3.777 | 1.004 | 0.4458 | 0.1186 | 10.00 |
| H3-d | 18.85 | 14.71 | 3.568 | 0.805 | 0.2423 | 0.0547 | 15.11 |
| H6-k | 11.79 | 8.673 | 2.614 | 0.453 | 0.3012 | 0.0522 | 17.57 |
| H6-n | 13.80 | 10.27 | 3.044 | 0.803 | 0.2963 | 0.0781 | 21.46 |
| H6-p | 16.94 | 12.15 | 3.793 | 0.718 | 0.3121 | 0.0591 | 11.47 |
| H8-g | 11.86 | 8.947 | 2.353 | 0.559 | 0.2624 | 0.0624 | 17.07 |
| H8-i | 9.569 | 7.254 | 1.915 | 0.276 | 0.2641 | 0.0380 | 11.35 |
| AVG | 13.63 | 10.16 | 2.866 | 0.598 | 0.2878 | 0.0605 | 14.21 |
| SD | 3.018 | 2.485 | 0.705 | 0.216 | 0.0653 | 0.0236 | 4.148 |
| Longitudinal | | | | | | | |
| Specimen | $\sigma_A$ (kPa) | $\sigma_1$ (kPa) | $\sigma_3$ (kPa) | $\sigma_5$ (kPa) | $IR$ | $RR$ | $\Delta t$ (msec) |
| H1-b | 23.96 | 15.80 | 6.275 | 1.541 | 0.3972 | 0.0976 | 9.229 |
| H2-c | 13.17 | 9.224 | 3.315 | 0.566 | 0.3595 | 0.0614 | 11.45 |
| H2-e | 10.74 | 7.553 | 2.767 | 0.349 | 0.3670 | 0.0462 | 11.30 |
| H2-i | 10.18 | 7.988 | 1.938 | 0.265 | 0.2426 | 0.0331 | 15.40 |
| H3-a | 23.03 | 16.75 | 5.003 | 1.163 | 0.2987 | 0.0694 | 10.91 |
| H3-e | 13.87 | 9.948 | 3.111 | 0.674 | 0.3127 | 0.0678 | 10.17 |
| H6-j | 13.17 | 9.724 | 2.702 | 0.662 | 0.2775 | 0.0681 | 13.47 |
| H6-m | 26.84 | 19.00 | 6.603 | 1.373 | 0.3474 | 0.0722 | 16.71 |
| H6-o | 15.91 | 11.25 | 3.630 | 0.842 | 0.3224 | 0.0748 | 15.69 |
| H8-h | 28.40 | 19.70 | 6.656 | 1.639 | 0.3380 | 0.0832 | 12.54 |
| H8-j | 13.95 | 10.12 | 3.114 | 0.681 | 0.3077 | 0.0672 | 15.80 |
| AVG | 17.56 | 12.46 | 4.101 | 0.887 | 0.3246 | 0.0674 | 12.97 |
| SD | 6.659 | 4.472 | 1.718 | 0.472 | 0.0436 | 0.0170 | 2.631 |

Table 9: The average total stress amplitude, 1 Hz harmonic, 3 Hz harmonic, 5 Hz harmonic, Interaction Ratio, Roughness Ratio, and lead time on deformation cycles 20 through 50 for each specimen in the Porcine 25% deformation group.

| Circumferential | | | | | | | |
|---|---|---|---|---|---|---|---|
| Specimen | $\sigma_A$ (kPa) | $\sigma_1$ (kPa) | $\sigma_3$ (kPa) | $\sigma_5$ (kPa) | $IR$ | $RR$ | $\Delta t$ (msec) |
| P1-a | 2.455 | 1.900 | 0.445 | 0.020 | 0.2341 | 0.0107 | 12.56 |
| P1-c | 4.433 | 3.755 | 0.636 | 0.016 | 0.1694 | 0.0043 | 19.18 |
| P1-e | 5.110 | 4.167 | 0.923 | 0.046 | 0.2217 | 0.0110 | 16.18 |
| P2-h | 2.167 | 1.713 | 0.381 | 0.007 | 0.2227 | 0.0041 | 19.82 |
| P2-j | 4.446 | 3.770 | 0.692 | 0.034 | 0.1837 | 0.0090 | 18.55 |
| P2-l | 3.035 | 2.610 | 0.328 | 0.006 | 0.1257 | 0.0023 | 15.09 |
| P3-i | 10.32 | 9.201 | 1.036 | 0.063 | 0.1126 | 0.0069 | 16.11 |
| P3-k | 13.16 | 11.64 | 1.289 | 0.199 | 0.1107 | 0.0171 | 12.79 |
| P4-g | 7.486 | 6.257 | 1.116 | 0.124 | 0.1783 | 0.0197 | 20.63 |
| P4-i | 9.675 | 8.446 | 1.110 | 0.142 | 0.1314 | 0.0168 | 20.17 |
| P4-k | 2.515 | 2.213 | 0.272 | 0.008 | 0.1229 | 0.0035 | 23.83 |
| AVG | 5.891 | 5.061 | 0.748 | 0.060 | 0.1648 | 0.0096 | 17.72 |
| SD | 3.733 | 3.359 | 0.363 | 0.066 | 0.0469 | 0.0061 | 4.012 |
| Longitudinal | | | | | | | |
| Specimen | $\sigma_A$ (kPa) | $\sigma_1$ (kPa) | $\sigma_3$ (kPa) | $\sigma_5$ (kPa) | $IR$ | $RR$ | $\Delta t$ (msec) |
| P1-b | 3.124 | 2.580 | 0.446 | 0.010 | 0.1728 | 0.0039 | 19.22 |
| P1-d | 4.250 | 3.290 | 0.965 | 0.012 | 0.2934 | 0.0037 | 18.55 |
| P1-f | 4.384 | 3.579 | 0.772 | 0.025 | 0.2159 | 0.0073 | 18.40 |
| P2-i | 6.332 | 5.500 | 0.802 | 0.033 | 0.1457 | 0.0060 | 19.55 |
| P2-k | 7.439 | 6.506 | 0.792 | 0.060 | 0.1217 | 0.0092 | 11.99 |
| P2-m | 3.806 | 3.135 | 0.641 | 0.006 | 0.2046 | 0.0018 | 23.86 |
| P3-j | 5.903 | 4.901 | 0.919 | 0.094 | 0.1875 | 0.0192 | 20.74 |
| P3-l | 2.891 | 2.634 | 0.173 | 0.026 | 0.0656 | 0.0099 | 17.20 |
| P4-h | 4.960 | 4.183 | 0.716 | 0.060 | 0.1712 | 0.0143 | 18.82 |
| P4-j | 6.318 | 5.474 | 0.766 | 0.065 | 0.1400 | 0.0119 | 17.90 |
| P4-l | 5.284 | 4.429 | 0.799 | 0.086 | 0.1800 | 0.0193 | 22.28 |
| AVG | 4.972 | 4.201 | 0.708 | 0.043 | 0.1726 | 0.0097 | 18.96 |
| SD | 1.438 | 1.288 | 0.224 | 0.031 | 0.0580 | 0.0060 | 3.330 |

Table 10: The average total stress amplitude, 1 Hz harmonic, 3 Hz harmonic, 5 Hz harmonic, Interaction Ratio, Roughness Ratio, and lead time on deformation cycles 20 through 50 for each specimen in the Porcine 50% deformation group.

| Circumferential | | | | | | | |
|---|---|---|---|---|---|---|---|
| Specimen | $\sigma_A$ (kPa) | $\sigma_1$ (kPa) | $\sigma_3$ (kPa) | $\sigma_5$ (kPa) | $IR$ | $RR$ | $\Delta t$ (msec) |
| P1-j | 10.25 | 8.314 | 1.567 | 0.279 | 0.1885 | 0.0336 | 19.25 |
| P1-m | 13.21 | 11.04 | 1.890 | 0.085 | 0.1713 | 0.0077 | 20.48 |
| P2-a | 3.272 | 2.316 | 0.778 | 0.104 | 0.3358 | 0.0448 | 16.64 |
| P2-c | 5.159 | 4.154 | 0.956 | 0.135 | 0.2299 | 0.0327 | 22.40 |
| P3-a | 15.35 | 11.58 | 3.042 | 0.718 | 0.2628 | 0.0620 | 15.28 |
| P3-e | 15.47 | 12.13 | 2.920 | 0.462 | 0.2407 | 0.0381 | 14.58 |
| P3-g | 7.727 | 5.866 | 1.692 | 0.238 | 0.2884 | 0.0406 | 16.37 |
| P4-a | 6.681 | 5.338 | 1.222 | 0.092 | 0.2289 | 0.0172 | 12.76 |
| P4-c | 9.984 | 7.887 | 1.891 | 0.252 | 0.2398 | 0.0319 | 13.55 |
| P4-e | 10.50 | 8.109 | 2.049 | 0.320 | 0.2527 | 0.0395 | 15.52 |
| P5-a | 6.658 | 4.962 | 1.564 | 0.373 | 0.3158 | 0.0749 | 18.88 |
| AVG | 9.478 | 7.426 | 1.779 | 0.278 | 0.2504 | 0.0384 | 16.88 |
| SD | 4.027 | 3.217 | 0.713 | 0.191 | 0.0494 | 0.0185 | 3.299 |
| Longitudinal | | | | | | | |
| Specimen | $\sigma_A$ (kPa) | $\sigma_1$ (kPa) | $\sigma_3$ (kPa) | $\sigma_5$ (kPa) | $IR$ | $RR$ | $\Delta t$ (msec) |
| P1-i | 8.087 | 6.301 | 1.532 | 0.053 | 0.2432 | 0.0084 | 19.54 |
| P1-l | 5.426 | 4.336 | 0.869 | 0.059 | 0.2004 | 0.0136 | 26.38 |
| P2-b | 8.242 | 6.157 | 1.843 | 0.460 | 0.2998 | 0.0746 | 16.56 |
| P2-e | 4.242 | 3.154 | 0.947 | 0.104 | 0.3001 | 0.0330 | 11.40 |
| P2-g | 10.17 | 7.810 | 1.976 | 0.513 | 0.2529 | 0.0656 | 19.04 |
| P3-b | 8.435 | 6.406 | 1.797 | 0.244 | 0.2805 | 0.0380 | 14.41 |
| P3-f | 8.463 | 6.799 | 1.510 | 0.206 | 0.2221 | 0.0303 | 17.14 |
| P3-h | 11.20 | 8.759 | 2.065 | 0.375 | 0.2357 | 0.0428 | 15.10 |
| P4-b | 10.79 | 8.348 | 2.202 | 0.281 | 0.2637 | 0.0336 | 16.72 |
| P4-d | 6.924 | 5.467 | 1.172 | 0.313 | 0.2144 | 0.0572 | 14.88 |
| P4-f | 6.559 | 5.169 | 1.198 | 0.160 | 0.2317 | 0.0310 | 13.50 |
| AVG | 8.049 | 6.246 | 1.555 | 0.252 | 0.2495 | 0.0389 | 16.79 |
| SD | 2.172 | 1.688 | 0.460 | 0.155 | 0.0335 | 0.0203 | 4.158 |

# 5 Discussion

The non-linear and hyper-viscoelastic behavior of aortic tissue is demonstrated in both the constant rate and sinusoidal translational shear deformation experiments. The sinusoidal tests also show the effect of hydration on the harmonic response of aortic tissue. Combining the material behavior of aortic tissue with the many factors that impact the response of aortic tissues (Humphrey and Holzapfel, 2011) makes it nearly impossible to create an accurate material model of the aorta. Therefore, no model is attempted in this thesis. Instead, the dynamic response properties of aortic tissue are analyzed with dynamic response variables, such as the $RF$, $IR$ and $RR$. The dynamic variables help identify potential incompatibilities between porcine and future TEVG specimens along with the differences between human and porcine specimens.

## 5.1 Viscoelasticity of Aortic Tissues

Regardless of the deformation test or any specimen factors, the viscoelasticity of aortic tissues is verified in these experiments. All specimens exhibit a time-dependent response wherein the stress leads the response of the deformation controlled experiments. The stress leading strain phenomena is often referred to as the phase angle for sinusoidal loading. Here, it is referred to as the lead time because it occurs in both the sinusoidal and constant rate translational shear deformation tests. The stress response lead time is a common occurrence in viscoelastic materials and proves that the aorta is a viscoelastic material. Additionally, stress relaxation in constant rate tests and amplitude decreases in sinusoidal tests provide more proof that the aorta is a viscoelastic material.

## 5.2 Constant Rate Deformation

A non-linear viscoelastic material is described as a material whose response to large deformation is time-dependent (Wineman, 2009). In the constant rate trans-

lational shear tests, specimens exhibit this non-linear viscoelastic behavior, as shown in Figures 26 and 27. Specimens that undergo the faster 12 mm/sec loading rate tend to have lower maximum and relaxation stresses along with faster stress relaxation on average than specimens that undergo 1 mm/sec loading rates. Faster loading rates resulting in lower stresses indicates that the aortic wall is better suited to respond to fast acting loads. Given that the aorta responds to fast acting loads frequently *in vivo*, it is not surprising that the aortic wall is able to handle fast loading.

In the loading region, the stress response behavior is somewhat unpredictable. The convexity of the stress response curve is either up, down, or a combination of convexity's. The differences in the stress response shape is seemingly random, occurring with both circumferential and longitudinal specimens. For 1 mm/sec spec-

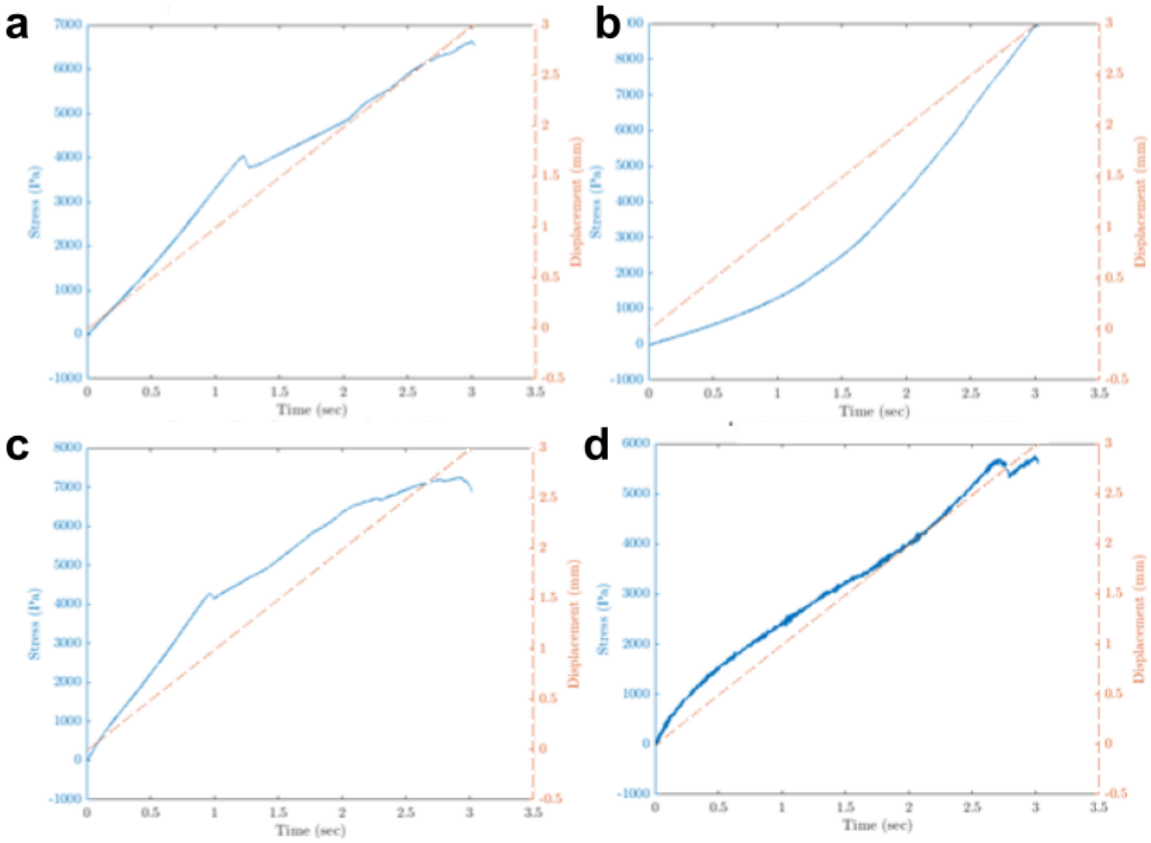


Figure 26: The stress response of 1 mm/sec Porcine during constant rate deformation for specimens (a) cP2-k, (b) cP3-c, (c) cP2-l, and (d) cP1-e.

imens, the stress response may have multiple local maxima in the loading region, as shown in specimens cP2-k, cP3-c, and cP2-l (Fig. 26a-c). It is unknown what causes the multiple local maxima, but it could be an indication that several bonds in the specimen either break or disentangle at the time of the maxima. Interestingly, the local maxima phenomena does not occur as frequently in the 12mm/sec specimens. The 12 mm/sec specimens have lower stresses on average, so perhaps the lack of local maxima's is caused by a lack of stress in the tissue. Lower stresses allow the tissue to respond without bond breaking or disentanglement.

Potentially, TEVG specimens that exhibit different constant rate properties could create incompatibilities between TEVG and normal tissue. Aortic tissue that

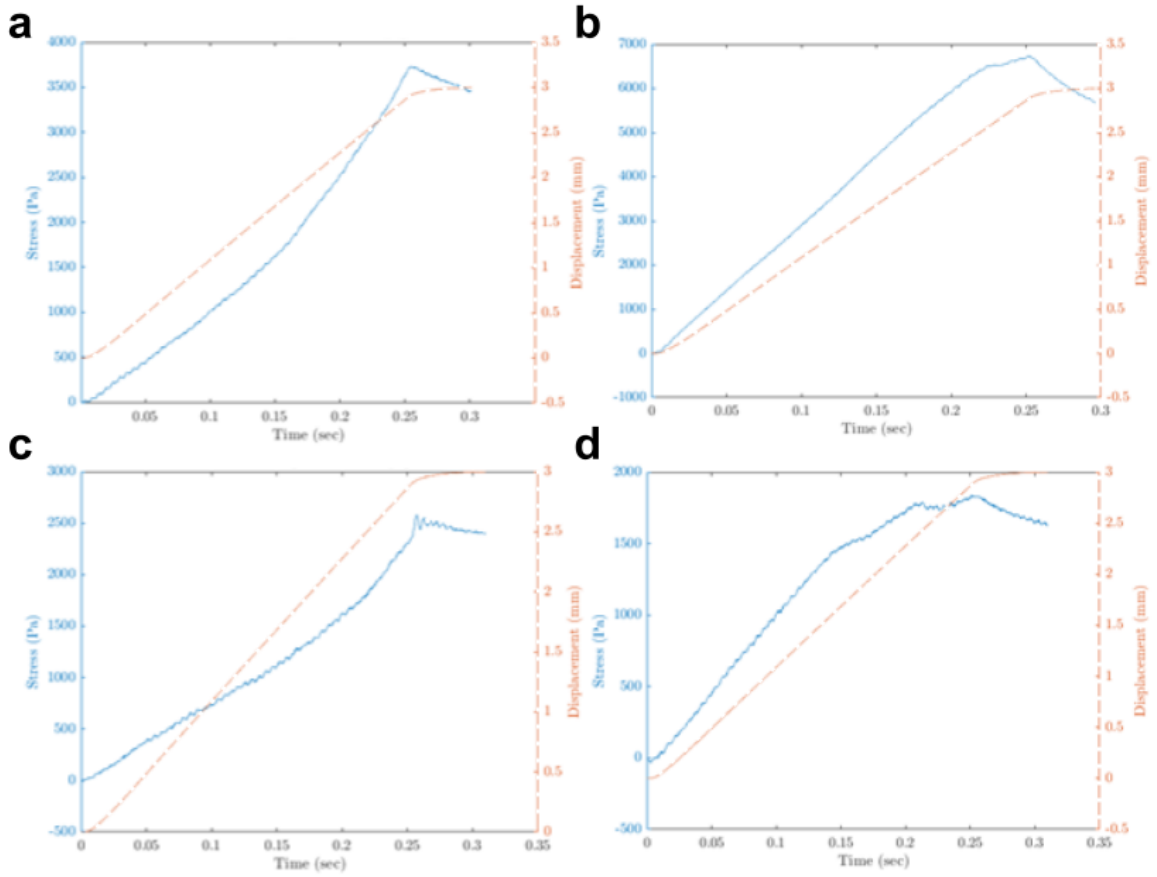


Figure 27: The stress response of 12 mm/sec Porcine during constant rate deformation for specimens (a) cP3-k, (b) cP2-c, (c) cP3-f, and (d) cP5-a.

does not recover from induced stress similar to normal human specimens could create internal stresses where the TEVGs are grafted. Porcine aortic tissue has been shown to respond effectively to faster loading rates. For TEVGs to be effective, they likely need to mimic the aortic walls ability to respond to fast loading. Additionally, TEVGs need to relax on a similar scale and speed as normal human tissue to prove that TEVGs are able to recover efficiently from large deformations.

## 5.3 Sinusoidal Shear Deformation

In all sinusoidal specimens, the first deformation cycle contains the peak amplitude of stress for the entire 50 cycle test (Fig. 14). Stress amplitudes in subsequent cycles decrease and approximately level out around the 5th deformation cycle, generally speaking. This decrease in stress amplitude resembles the stress softening, known as the Mullins effect (Mullins, 1948), that is seen in rubber (Diani et al., 2006). Rubber materials are comprised of long macromolecular, crosslinked chains and, when damaged, are hyper-viscoelastic materials (Blanchard and Parkinson, 1952). Rubber materials exhibit the highest stress response upon initial deformation and then exhibit decreasing stress responses on subsequent deformation cycles. There is no general agreement regarding the microstructural source of the Mullins effect, but several interpretations have been proposed. Stress softening has been interpreted to originate from bond rupture (Blanchard and Parkinson, 1952), slipping molecules and re-bonding chains (Houwink, 1956), and chain disentanglement (Hanson et al., 2005). Although the Mullins effect phenomena is not extensively examined in this study, it provides useful background for analyses of aortic tissue.

### 5.3.1 Microstructural Sources of the Shear Stress Response

Although the source of specific harmonics is not immediately clear, the microstructural components that are likely to cause each harmonic is ascertained through knowledge of both the mode of deformation and the orientation of microstructural components in the medial layer. With the specimen orientations used in this

study, the shear deformation mode generates the highest stress response from components that provide structural bonds in the radial direction. Inducing translational shear deformation on a specimen causes adjacent radial layers to deform relative to one another, parallel to the shear deformation direction. The relative deformation of adjacent layers stresses the interlaminar bonds which link the layers together. In aortic tissue, the interconnecting chain of elastic laminae, elastic fibers, and smooth muscle cells (Fig. 3) connect medial functional units in the radial direction. This interconnecting chain (here referred to as the elastic network) experiences significant deformation and stress in shear. Conversely, components which are both preferentially oriented in the circumferential axis and not interconnected to radially adjacent layers, such as collagen fibers, do not generate a significant shear stress response because they do not experience significant deformation in the shear mode, as indicated by the similar shear response in the circumferential and longitudinal directions. It is much more likely that the elastic network, rather than collagen fiber, dominates the stress response under shear deformation.

The dynamic shear deformation introduces a stress response from the redistribution of interstitial fluid. This aspect of aortic tissue is often neglected in quasi-static loading experiments, however, interstitial fluid redistribution is an important characteristic to define because the fluid has the potential to generate internal shear within the aortic wall. Under dynamic shear deformation, interstitial fluid redistributes and interacts with solid structural components throughout the deformation. The fluid redistribution causes friction on the elastin lamellae, as indicated by the Interaction Ratio. Additionally, disorganized microstructural units, such as the free floating proteoglycans found in humans, provide some resistance to the redistribution of interstitial fluid where they are present in the aortic tissue. Prior to deformation, porcine aortic tissue is more structurally organized and less likely to contain these disorganized units, as evidenced by histological studies of both tissue types (Dingemans

et al., 1981; Dingemans et al., 2000).

The average results for each group provide a comparative basis for the microstructural source of each harmonic (Fig. 14 and 16). The 1 Hz and 5 Hz harmonics both exhibit similar transient responses in which the magnitude of stress is the highest in the first cycle and decreases on subsequent cycles, similar to the Mullins effect. Additionally, the 1 Hz harmonic contains by far the largest magnitude of stress response from aortic tissue deformed at a 1 Hz frequency (Table 5). Therefore, this harmonic originates from the elastic network, given that it is the main structural component of aortic tissue other than collagen fibers. The 5 Hz harmonic is the smallest in amplitude of the 1 Hz, 3 Hz, and 5 Hz harmonics. Because there are few other microstructural solids that can cause a shear response of this magnitude, the 5 Hz harmonic likely arises from the presence of disorganized or degenerated microstructural units. This determination is also supported by the human groups having a higher average 5 Hz harmonic magnitude compared to the corresponding pig groups because pigs have less disorganized microstructural units than humans during shear.

The 3 Hz harmonic contains the next largest amplitude of stress response after the 1 Hz harmonic and contains a transient response that is in opposition to both the 1 Hz and 5 Hz transient responses. The 3 Hz harmonic also creates a shoulder in the shear stress response of the aortic wall (Fig. 8). In all tests, regardless of tissue type, loading direction or loading magnitude, the average 3 Hz harmonic for a group increases from the first cycle to the second cycle. The transition from the second cycle to the third cycle is not the same for all groups, however. For the human circumferential and longitudinal 50% deformation groups, the stress amplitude decreases on the third cycle and levels out on subsequent cycles. For all other groups, the stress amplitude does not decrease on the third cycle; the amplitude simply levels out. An explanation for these transient responses arises from the interstitial fluid-solid interaction within the aorta. On the first cycle of the test, the solid components

are undamaged and therefore there is less interaction with interstitial fluid, resulting in a lower stress magnitude. In the second cycle, the solid components are damaged, causing resistance to fluid flow and maximizing the fluid-solid interaction. For the human circumferential and longitudinal 50% deformation groups, this fluid-solid interaction is large enough to break bonds of the solid components interacting with the interstitial fluid. The broken solid bonds lowers the fluid resistance provided by the solid components and causes the stress amplitude to decrease on subsequent cycles. In all other groups, the fluid-solid drag force is not great enough to break bonds of solid components. Therefore, instead of a decrease in stress, the drag force levels out once the tissue reaches the peak resistance of fluid redistribution. The magnitude of stress contained within the 3 Hz harmonic is also indicative of interstitial fluid because of high levels of hydration in aortic tissue.

The 3 Hz harmonic sine term, $b_3$ (Eqn. 19), is negative across all cycles for all specimens in this study. The cosine term, $a_3$, is often negligible, so the negative $b_3$ creates shoulders in the aortic tissue stress response (Fig. 8). This shoulder is another indicator that the 3 Hz harmonic originates from interstitial fluid redistribution. The interstitial fluid-solid drag force is dependent on fluid velocity, and there is likely a lag in the fluid redistribution velocity relative to the deformation of the specimen. The third harmonic therefore causes the shoulders seen in the aortic tissue shear stress response.

### 5.3.2 Deformation Direction Factor

The quasi-periodic $IR$ and $RR$ amplitudes in specimens of the same tissue type and deformation amplitude exhibit no statistical difference between the deformation direction (Table 6). The lack of a statistical difference in deformation direction reinforces the fact that the fluid-solid interaction response in shear deformation is not dependent on microstructural elements which are preferentially oriented in the circumferential direction, such as collagen fibers. However, for both the $IR$ and $RR$

amplitudes, there is less confidence that there is no statistical difference between human aortic tissue at 25% and 50% deformations than between porcine aortic tissue at 25% and 50% deformations. While not statistically different, the trend shows that slightly larger $IR$ and $RR$ amplitudes are generated in the longitudinal direction (Fig. 17), particularly in human aortic tissue. A potential explanation for this trend is that in both tissue microstructures, the elastic network elastin links lie mainly in the circumferential-radial plane (Dingemans et al., 2000). In the circumferential shear direction, the elastic network is nearly parallel to the shear deformation, and there is likely less resistance to interstitial fluid flow. The trend is more pronounced in humans due to the more disorganized structure of human aortic tissue compared to porcine aortic tissue (Fig. 3).

### 5.3.3 Deformation Amplitude Factor

Of the 28 one-factor ANOVAs analyzing the effect of the deformation amplitude factor on $IR$, $RR$, $\Delta t$, $\sigma_A$, $\sigma_1$, $\sigma_3$, and $\sigma_5$, only 4 ANOVAs found that there was no statistical difference between groups (Porcine Circumferential $\Delta t$, Porcine Longitudinal $\Delta t$, Human Circumferential $\sigma_1$, and Porcine Circumferential $\sigma_1$). There is a clear difference between deformation amplitude groupings in every dynamic variable analyzed in the sinusoidal experiments, indicating that there are differences in both fluid and solid responses of aortic tissue, as well as the fluid-solid interaction. Larger deformation amplitudes produce significantly larger magnitudes for harmonics, $IR$, and $RR$. The larger $IR$ and $RR$ magnitudes indicates that more fluid-solid interaction occurs at larger amplitudes, allowing for more damage to occur in the larger deformation specimens.

### 5.3.4 Tissue Type Factor

The $IR$ amplitude measures the relative fluid-solid interaction in aortic tissues. Because the medial microstructure of human and porcine aortic tissue is structurally very similar (Dingemans et al., 2000), it is expected that the tissues resistances

to interstitial fluid flow are similar. In these experiments, human and porcine tissue $IR$ values are only statistically different in the longitudinal direction at a 50% deformation amplitude (Table 6). All other deformation directions and amplitudes show that the tissues are statistically the same. However, each human specimen group has higher average $IR$ amplitudes than porcine specimen groups with the same deformation direction and amplitude (Fig. 17). The human specimens therefore tend to have somewhat higher resistance to interstitial fluid flow than porcine specimens, although often not statistically different. The tendency for human specimens to have higher resistance to interstitial fluid flow than porcine specimens likely arises from the degenerated elastic network seen in humans (Fig. 3). Although human and porcine medial microstructures are similar, human aortic tissue contains more disorganized units that have the potential to resist interstitial fluid flow. The human aortic tissue specimens tend to have higher $IR$ amplitudes because of these disorganized units.

The $RR$ amplitude measures the relative smoothness of the elastin lamellae to shear deformation response of aortic tissue. All of the human and porcine specimen groups contain statistically different quasi-periodic $RR$ amplitudes, regardless of the deformation direction or amplitude (Table 6). Once again an explanation arises from the medial microstructures of each tissue. Because the $RR$ amplitude measures the relative smoothness and is small in magnitude compared to the $IR$ amplitude (Fig. 17), the disorganized and degenerated microstructure of the human media as compared to the porcine media is likely the cause of human specimens having larger $RR$ amplitudes. While the degeneration of the human media is not great enough to cause a statistical difference in the $IR$ amplitude, the $RR$ amplitude arises directly from medial degeneration. Therefore, the differences between the human and porcine $RR$ amplitudes are more obvious than $IR$ amplitudes because the porcine medial microstructure is more organized than the human medial microstructure.

## 5.4 Aortic Wall Microstructural Differences

While there are slight differences between the medial microstructure of porcine and human aortic tissues, the reason for these discrepancies are unclear. Given that the porcine aortic tissue is retrieved from pigs aged 6 to 9 months old (Martin et al., 2011), the differences in microstructure between porcine and human aortic tissue tested could be due to either species differences or age-related degeneration. Stephens and Grande-Allen (2007) discovered that collagen content in porcine increases with age, which also occurs in humans (Martin et al., 2011). Stephens and Grande-Allen (2007) also suggested that a 6 month old pig corresponds to a 17-year old male or 19 year-old female while a 6-year old pig corresponds to an aged human. However, in humans, it is uncommon for an aortic specimen to be obtained from a young patient (age <20 years) without a pathological disease, so less is known about the exact medial microstructure for young humans. It is therefore difficult to make direct comparisons between young pigs and young humans to determine the reason for the microstructural differences found in the aortic wall. However, young porcine tissue is used in this study because the proposed TEVGs are grown in young pigs.

Porcine aortic tissue is considered as the animal species most similar to human aortic tissue (Nicosia et al., 2002; Gundiah et al., 2008; Okuno et al., 2012), so it may be postulated that human aortic tissue is formed with a structure close to what is seen in 6 to 9 month-old pigs and then degenerates into the microstructure that is seen in aged human studies. While this hypothesis has not been tested in this study, future research comparing aged pig aortic tissue to aged humans could be beneficial to establish a better understanding of the similarities between these tissues. Further knowledge of similarities between the tissues as a function of age is not necessary for the TEVG application, however.

## 5.5 Aortic Wall Similarities

The ultimate goal of this work is to investigate whether porcine dynamic shear properties are similar enough to humans to justify growing TEVGs in pigs as a next step for animal testing. The mechanical efficacy of specific TEVGs need to be tested individually, however, there was previously no information available regarding dissection related properties of the porcine aorta compared to the human aorta. Without this information, using porcine aortic tissue as the most similar to human aortic tissue for TEVG development is an unproven assumption. It is critical that porcine aortic tissue has similar dynamic and dissection resistance-related properties to human aortic tissue to make informed conclusions regarding whether TEVGs grown in pigs will be effective when grown in humans.

The dynamic and dissection-related properties of porcine tissue found in this study are sufficiently similar to human aortic tissue to justify growing model TEVGs in pigs to further the development of TEVGs. Overall, porcine aortic tissue displays dynamic shear properties that trend towards a healthy human aorta as opposed to a pathological human aorta (Haslach et al., 2020). Porcine and human aortic tissue have similar lead times in sinusoidal shear deformation indicating that porcine tissue responds at the same time as human tissue. This similarity allows researchers to determine whether the lead time of porcine grown TEVGs is likely to create internal stresses in human implementation. Different lead times in aortic grafts, and therefore deformation mismatches, has the potential to generate internal stresses in a grafted tissue. Additionally, porcine aortic tissue displays $IR$ and $RR$ properties that are lower in magnitude compared to humans and indicative of healthier, non-degenerated, and potentially younger human aortic tissue. If TEVG porcine specimens can match the porcine aortic tissue $IR$ and $RR$ properties, dissection within the graft is unlikely to occur *in vivo*. Porcine aortic tissue also displays an ability to effectively respond to fast loading, as shown by the porcine specimens relaxation properties in the 12

mm/sec constant rate tests. The porcine aortic tissue fast relaxation properties are an important property for tissue in the aortic wall because of the dynamic loads that the aorta undergoes *in vivo*. Porcine grown TEVGs likely need to replicate the porcine aortic tissue's ability to effectively respond to fast loading to be deemed a mechanically viable grafting material.

## 5.6 Limitations and Future Work

While this work aims to extract useful information relating to damage of the aortic wall, the complexities of aortic tissue do create practical limitations in studying the tissue's deformation response. In the excision of specimens, no standard diameter or wall thickness measurements are possible because of the non-uniform wall thickness around the cylindrical shape of the aorta. The specimens used in these experiments are small in size (6 mm by 6 mm), but even at this scale the wall thickness between specimens can vary considerably in different sections of the aortic wall. Lacking the appropriate technology and methods to take measurements, it requires a skilled operator to get accurate measurements for both wall thickness and diameter. It is also known that the location of the specimen within the aortic wall effects the mechanical response of specimens (Haskett et al., 2010), so an additional challenge to track the specimens origin is created.

In the future, researchers may grow TEVGs in porcine, furthering their development towards implementation in humans (Yeung et al., 2020). The normal porcine aortic tissue in these experiments displayed similar dynamic and dissection-related properties to human aortic tissue, justifying the use of pigs to further the development of TEVG models. Additionally, baseline properties of normal porcine aortic tissue have been found to compare with any TEVG grown in pigs. If porcine TEVG specimens exhibit shear properties that indicate increased interstitial fluid flow resistance or medial degeneration as compared to normal porcine specimens, the TEVG specimens may not be sufficient models for human implementation. Additional

measurements from TEVG specimens, such as a time response mismatch with normal porcine aortic tissue, is another basis for analyzing the effectiveness of the TEVG aorta implementation.

# 6 Conclusion

Dynamic shear properties of porcine aortic tissue have been analyzed in this study to determine whether growing TEVGs in pigs is a justifiable approach to prepare for human implementation. Additionally, the experimental results prepare for future analyses of the dynamic properties of TEVG models produced in pigs, such as those in Yeung et al. (2020). Dynamic shear properties relating to rupture mechanics, such as the Interaction Ratio and Roughness Ratio, have been computed for normal porcine aortic tissue. Quantified stress relaxation properties in the porcine aorta have also been shown using the Relaxation Fraction. This is the first study known to the author that examines dynamic, dissection-related properties of porcine aortic tissue. Importantly, the dynamic mechanical properties of porcine aortic tissue are sufficiently similar to the dynamic mechanical properties of human aortic tissue to justify further development of TEVGs grown in pigs.

The dynamic characteristics of porcine aortic tissue found in this thesis prepare for analysis of any TEVG grown in pigs. TEVG porcine specimens which display shear properties that indicate increased interstitial fluid flow resistance or degenerated microstructures as compared to normal porcine aortic tissues provides a basis for determining the effectiveness of the TEVG porcine tissue. TEVG porcine specimens must also display time response characteristics that are consistent with normal porcine specimens because differences in the time response of TEVG tissue and human aortic tissue has the potential to create deformation mismatches and internal stresses within the aortic wall.

Additionally, more data that is used to determine the microstructural sources of the shear stress response have been obtained and recorded. By comparing both the shear stress response and the medial microstructures of porcine and human aortic tissue specimens, more accurate postulations on the specific microstructural elements

that generate the different dissection-related shear properties in porcine and human aortic tissues are possible. These postulations build on previous studies that compare normal human aortic tissue to aneurysmal human aortic tissue (Haslach et al., 2020).

**Conflict of Interest Statement** The author declares no conflict of interest.

# References


[1] A.A.M. Ali, P. Sharma, R.N. Rege, S. Rajesh, and K. Nadhamuni. "Dacron graft aneurysm with dissection". In: *The Indian journal of radiology & imaging* 26.4 (2016), p. 472.

[2] V. Anand and I.C. Christov. "On the deformation of a hyperelastic tube due to steady viscous flow within". In: *Dynamical Processes in Generalized Continua and Structures*. Springer, 2019, pp. 17–35.

[3] A.F. Blanchard and D. Parkinson. "Breakage of carbon-rubber networks by applied stress". In: *Rubber Chemistry and Technology* 25.4 (1952), pp. 808–842.

[4] J. Bogaert, S. Dymarkowski, W. Budts, M. Gewillig, and W. Daenen. "Graft dilation after redo surgery for aneurysm formation following patch angioplasty for aortic coarctation". In: *European journal of cardio-thoracic surgery* 19.3 (2001), pp. 274–278.

[5] T.E. Carew, R.N. Vaishnav, and D.J. Patel. "Compressibility of the arterial wall". In: *Circulation research* 23.1 (1968), pp. 61–68.

[6] P. Carrascosa, C. Capuñay, A. Deviggiano, G.A. Rodríguez-Granillo, M.I. Sagarduy, P. Cortines, J. Carrascosa, and J.C. Parodi. "Thoracic aorta cardiac-cycle related dynamic changes assessed with a 256-slice CT scanner". In: *Cardiovascular diagnosis and therapy* 3.3 (2013), p. 125.

[7] C. Cavinato, J. Molimard, N. Curt, S. Campisi, L. Orgéas, and P. Badel. "Does the Knowledge of the Local Thickness of Human Ascending Thoracic Aneurysm Walls Improve Their Mechanical Analysis?" In: *Frontiers in Bioengineering and Biotechnology* 7 (2019), p. 169.

[8] K.Y. Chooi, A. Comerford, S.J. Sherwin, and P.D. Weinberg. "Intimal and medial contributions to the hydraulic resistance of the arterial wall at different pressures: a combined computational and experimental study". In: *Journal of The Royal Society Interface* 13.119 (2016), pp. 234–245.

[9] M.J. Chow, R. Turcotte, C.P. Lin, and Y. Zhang. "Arterial extracellular matrix: a mechanobiological study of the contributions and interactions of elastin and collagen". In: *Biophysical journal* 106.12 (2014), pp. 2684–2692.

[10] C.J. Chuong and Y.C. Fung. "Compressibility and constitutive equation of arterial wall in radial compression experiments". In: *Journal of biomechanics* 17.1 (1984), pp. 35–40.

[11] J.M. Clark and S. Glagov. "Transmural organization of the arterial media". In: *Arteriosclerosis* 5 (1985), pp. 19–34.

[12] I. Costantini, R. Cicchi, L. Silvestri, F. Vanzi, and F.S. Pavone. "In-vivo and ex-vivo optical clearing methods for biological tissues". In: *Biomedical optics express* 10.10 (2019), pp. 5251–5267.

[13] J.V. Delgadillo, S. Delorme, V. Mora, R. DiRaddo, and S.G. Hatzikiriakos. "Effect of deformation rate on the mechanical properties of arteries". In: *Journal of Biomedical Science and Engineering* 3.02 (2010), p. 124.

[14] J. Diani, M. Brieu, and J.M. Vacherand. "A damage directional constitutive model for Mullins effect with permanent set and induced anisotropy". In: *European Journal of Mechanics-A/Solids* 25.3 (2006), pp. 483–496.

[15] K. P. Dingemans, P. Teeling, J.H. Lagendijk, and A.E. Becker. "Extracellular matrix of the human aortic media: an ultrastructural histochemical and immunohistochemical study of the adult aortic media". In: *The Anatomical Record: An Official Publication of the American Association of Anatomists* 258.1 (2000), pp. 1–14.

[16] K.P. Dingemans, N. Jansen, and A.E. Becker. "Ultrastructure of the normal human aortic media". In: *Virchows Archiv A* 392.2 (1981), pp. 199–216.

[17] Centers for Disease Control. "Deaths, percent of total deaths, and death rates for the 15 leading causes of death in 5-year age groups, by race, and sex: United States". In: (2015).

[18] A. Duprey, O. Trabelsi, M. Vola, J. Favre, and S. Avril. "Biaxial rupture properties of ascending thoracic aortic aneurysms". In: *Acta biomaterialia* 42 (2016), pp. 273–285.

[19] J. Ferruzzi, D.A. Vorp, and J.D. Humphrey. "On constitutive descriptors of the biaxial mechanical behaviour of human abdominal aorta and aneurysms". In: *Journal of the Royal Society* 8.56 (2011), pp. 435–450.

[20] T. Freestone, R.J. Turner, A. Coady, D.J. Higman, R.M. Greenhalgh, and J.T. Powell. "Inflammation and matrix metalloproteinases in the enlarging abdominal aortic aneurysm". In: *Arteriosclerosis, thrombosis, and vascular biology* 15.8 (1995), pp. 1145–1151.

[21] J.M. Gipple and H.W. Haslach. "Damage to the rat cerebrum under in vitro sinusoidal translational shear deformation". In: *Journal of the Mechanical Behavior of Biomedical Materials* 110 (2020), p. 103969.

[22] N. Gundiah, P.B. Matthews, R. Karimi, A. Azadani, J. Guccione, S.T. Guy, D. Saloner, and E.E. Tseng. "Significant material property differences between the porcine ascending aorta and aortic sinuses". In: *Journal of Heart Valve Disease* 17.6 (2008), p. 606.

[23] D.E. Hanson, M. Hawley, R. Houlton, K. Chitanvis, P. Rae, E.B. Orler, and D.A. Wrobleski. "Stress softening experiments in silica-filled polydimethylsiloxane provide insight into a mechanism for the Mullins effect". In: *Polymer* 46.24 (2005), pp. 10989–10995.

[24] D. Haskett, G. Johnson, A. Zhou, U. Utzinger, and J.V. Geest. "Microstructural and biomechanical alterations of the human aorta as a function of age and location". In: *Biomechanics and modeling in mechanobiology* 9.6 (2010), pp. 725–736.

[25] H.W. Haslach. “A maximum dissipation thermodynamic multi-scale model for the dynamic response of the arterial elastin–water system”. In: *Acta mechanica* 213.1-2 (2010), pp. 169–188.

[26] H.W. Haslach. “Nonlinear viscoelastic, thermodynamically consistent, models for biological soft tissue”. In: *Biomechanics and Modeling in Mechanobiology* 3.3 (2005), pp. 172–189.

[27] H.W. Haslach, J. Gipple, J. Harwerth, and J. Rabin. “Interstitial fluid–solid interaction within aneurysmal and non-pathological human ascending aortic tissue under translational sinusoidal shear deformation”. In: *Acta Biomaterialia* 113 (2020), pp. 452–463.

[28] H.W. Haslach, J. Gipple, B. Taylor, and J. Rabin. “Comparison of aneurysmal and non-pathologic human ascending aortic tissue in shear”. In: *Clinical Biomechanics* 58 (2018), pp. 49–56.

[29] H.W. Haslach, L.N. Leahy, P. Fathi, J.M. Barrett, A.E. Heyes, T.A. Dumsha, and E.L. McMahon. “Crack Propagation and Its Shear Mechanisms in the Bovine Descending Aorta”. In: *Cardiovascular Engineering and Technology* 6.4 (2015), pp. 501–518.

[30] H.W. Haslach, P. Riley, and A. Molotsky. “The influence of medial substructures on rupture in bovine aortas”. In: *Cardiovascular Engineering and Technology* 2.4 (2011), pp. 372–387.

[31] H.W. Haslach, A. Siddiqui, A. Weerasooriya, R. Nguyen, J. Roshgadol, N. Monforte, and E. McMahon. “Fracture mechanics of shear crack propagation and dissection in the healthy bovine descending aortic media”. In: *Acta biomaterialia* 68 (2018), pp. 53–66.

[32] A.E. Hirst, V.J. Johns, and S.W. Kime. “Dissecting aneurysms of the aorta: a review of 505 cases”. In: *Medicine (Baltimore)* 37.1 (1958), pp. 217–279.

[33] G.A. Holzapfel. “Determination of material models for arterial walls from uniaxial extension tests and histological structure”. In: *Journal of Theoretical Biology* 238 (2006), pp. 290–302.

[34] G.A. Holzapfel. *Nonlinear solid mechanics : a continuum approach for engineering*. 2000. Chap. 6, pp. 239–294.

[35] G.A. Holzapfel, T.C. Gasser, and R.W. Ogden. “A New Constitutive Framework for Arterial Wall Mechanics and a Comparative Study of Material Models”. In: *Journal of Elasticity* 61 (2000), pp. 1–48.

[36] R. Houwink. “Slipping of molecules during the deformation of reinforced rubber”. In: *Rubber Chemistry and Technology* 29.3 (1956), pp. 888–893.

[37] J. Huang, Y. Wang, L. Lin, Z. Li, Z. Shan, and S. Zheng. “Comparison of dynamic changes in aortic diameter during the cardiac cycle measured by computed tomography angiography and transthoracic echocardiography”. In: *Journal of Vascular Surgery* 69.5 (2019), pp. 1538–1544.

[38] J.D. Humphrey. "Cardiovascular Solid Mechanics: Cells, Tissues, and Organs". In: *Springer Science & Business Media* (2002), pp. 249–259.

[39] J.D. Humphrey. "Possible mechanical roles of glycosaminoglycans in thoracic aortic dissection and associations with dysregulated transforming growth factor-$\beta$". In: *Journal of Vascular Research* 50.1 (2013), pp. 1–10.

[40] J.D. Humphrey and G.A. Holzapfel. "Mechanics, mechanobiology, and modeling of human abdominal aorta and aneurysms". In: *Journal of Biomechanics* 45.5 (2011), pp. 805–814.

[41] E.M. Isselbacher. "Thoracic and abdominal aortic aneurysms". In: *Circulation* 111.6 (2005), pp. 816–828.

[42] L.N. Leahy and H.W. Haslach. "Time-frequency analyses of fluid–solid interaction under sinusoidal translational shear deformation of the viscoelastic rat cerebrum". In: *Mechanics of Time-Dependent Materials* 22.1 (2018), pp. 1–27.

[43] P.P. Lelovas, N.G. Kostomitsopoulos, and T.T. Xanthos. "A Comparative Anatomic and Physiologic Overview of the Porcine Heart". In: *Journal of the American Association for Laboratory Animal Science* 53.5 (2014), pp. 432–438.

[44] Y. Luo, A. Duprey, and S. Avril. "Characteristics of thoracic aortic aneurysm rupture in vitro". In: *Acta Biomaterialia* 42 (2016), pp. 286–295.

[45] C. Martin, T. Pham, and W. Sun. "Significant differences in the material properties between aged human and porcine aortic tissues". In: *European Journal of Cardio-Thoracic Surgery* 40.1 (2011), pp. 28–34.

[46] C. Martin, W. Sun, C. Primiano, R. McKay, and J. Elefteriades. "Age-dependent ascending aorta mechanics assessed through multiphase CT". In: *Annals of biomedical engineering* 41.12 (2013), pp. 2565–2574.

[47] J.M. Mattson and Y. Zhang. "Structural and functional differences between porcine aorta and vena cava". In: *Journal of biomechanical engineering* 139.7 (2017).

[48] D. Miranda-Nieves and E.L. Chaikof. "Collagen and elastin biomaterials for the fabrication of engineered living tissues". In: *ACS Biomaterials Science & Engineering* 3.5 (2017), pp. 694–711.

[49] D.C. Moreira and L.C.S. Nunes. "Comparison of simple and pure shear for an incompressible isotropic hyperelastic material under large deformation". In: *Polymer Testing* 32.2 (2013), pp. 240–248.

[50] L. Mullins. "Effect of stretching on the properties of rubber". In: *Rubber chemistry and technology* 21.2 (1948), pp. 281–300.

[51] M.A. Nicosia, J.S. Kasalko, R.P. Cochran, D.R. Einstein, and K.S. Kunzelman. "Biaxial mechanical properties of porcine ascending aortic wall tissue." In: *The Journal of heart valve disease* 11.5 (2002), p. 680.

[52] D.R. Nolan and J.P. McGarry. "On the compressibility of arterial tissue". In: *Annals of biomedical engineering* 44.4 (2016), pp. 993–1007.

[53] T. Okuno, M. Yamaguchi, T. Okada, T. Takahashi, N. Sakamoto, E. Ueshima, K. Sugimura, and K. Sugimoto. "Endovascular creation of aortic dissection in a swine model with technical considerations". In: *Journal of vascular surgery* 55.5 (2012), pp. 1410–1418.

[54] I. Park and R.W. Schutz. ""Quick and easy" formulae for approximating statistical power in repeated measures ANOVA". In: *Measurement in Physical Education and Exercise Science* 3.4 (1999), pp. 249–270.

[55] S. Pashneh-Tala, S. MacNeil, and F. Claeyssens. "The Tissue-Engineered Vascular Graft — Past, Present, and Future". In: *Tissue Engineering* 22.1 (2016), pp. 68–100.

[56] J.A. Peña, M.A. Martinez, and E. Peña. "Failure damage mechanical properties of thoracic and abdominal porcine aorta layers and related constitutive modeling: phenomenological and microstructural approach". In: *Biomechanics and Modeling in Mechanobiology* 18 (2019), 1709–1730.

[57] J.A. Phillippi, S. Pasta, and D.A. Vorp. "Biomechanics and pathobiology of aortic aneurysms". In: *Biomechanics and mechanobiology of aneurysms*. Springer, 2011, pp. 67–118.

[58] J.T. Powell, L.C. Brown, and R.M. Greenhalgh. "The Rupture Rate of Large Abdominal Aortic Aneurysms: Is This Modified by Anatomic Suitability for Endovascular Repair?" In: *Journal of Vascular Surgery* 48.1 (2008), p. 247.

[59] W.H. Press, B.P. Flannery, S.A. Teukolsky, and W.T. Vetterling. *Numerical recipes*. 1989.

[60] P.P. Purslow. "Positional variations in fracture toughness, stiffness and strength of descending thoracic pig aorta". In: *Journal of biomechanics* 16.11 (1983), pp. 947–953.

[61] S.W. Rabkin. "Accentuating and opposing factors leading to development of thoracic aortic aneurysms not due to genetic or inherited conditions". In: *Frontiers in Cardiovascular Medicine* 2 (2015), p. 21.

[62] E.L. Ritman and A. Lerman. "The dynamic vasa vasorum". In: *Cardiovascular research* 75.4 (2007), pp. 649–658.

[63] S. Sarkar, K.M. Sales, G. Hamilton, and A.M. Seifalian. "Addressing thrombogenicity in vascular graft construction". In: *Journal of Biomedical Materials Research Part B: Applied Biomaterials* 82.1 (2007), pp. 100–108.

[64] Y. H. Shen, H.S. Lu, S.A. LeMaire, and A. Daugherty. "Unfolding the Story of Proteoglycan Accumulation in Thoracic Aortic Aneurysm and Dissection". In: *Arteriosclerosis, Thrombosis, and Vascular Biology* 39.10 (2019), pp. 1899–1901.

[65] E.K.W. Sim, S. Muskawad, C. Lim, J.H. Yeo, K.H. Lim, R.T. Grignani, A. Durrani, G. Lau, and C. Duran. "Comparison of Human and Porcine Aortic Valves". In: *Clinical Anatomy* 16 (2003), pp. 193–196.

[66] G.W. Snedecor and W.G. Cochran. *Statistical methods*. 1980.

[67] G. Sommer, S. Sherifova, P.J. Oberwalder, O.E. Dapunt, P.A. Ursomanno, A. DeAnda, B.E. Griffith, and G.A. Holzafpel. "Mechanical strength of aneurysmatic and dissected human thoracic aortas at different shear loading modes". In: *Journal of Biomechanics* 49.12 (2016), pp. 2374–2382.

[68] E.H. Stephens and J.K. Grande-Allen. "Age-related changes in collagen synthesis and turnover in porcine heart valves." In: *The Journal of heart valve disease* 16.6 (2007), pp. 672–682.

[69] P.C. Tang, M.A. Coady, C. Lovoulos, A. Dardik, M. Aslan, J.A. Elefteriades, and G. Tellides. "Hyperplastic cellular remodeling of the media in ascending thoracic aortic aneurysms". In: *Circulation* 112 (2005), pp. 1098–1105.

[70] J. Tong, A.J. Schriefl, T. Cohnert, and G.A. Holzapfel. "Gender Differences in Biomechanical Properties, Thrombus Age, Mass Fraction and Clinical Factors of Abdominal Aortic Aneurysms". In: *European Journal of Vascular and Endovascular Surgery* 45.4 (2013), pp. 364–372.

[71] L.R.G. Treloar. *The physics of rubber elasticity*. Oxford University Press, USA, 1975.

[72] V. Treska, B. Certik, M. Cechura, and M. Novak. "Ruptured abdominal aortic aneurysms – university center experience". In: *Interactive CardioVascular and Thoracic Surgery* 5.6 (2006), pp. 721–723.

[73] O.N. Tripathi, U. Ravens, and M.C. Sanguinetti. *Heart rate and rhythm: molecular Basis, pharmacological modulation and clinical implications*. Springer Science & Business Media, 2011.

[74] C.S. White, L.B. Haramati, J.J. Chen, and J.M. Levsky. *Cardiac Imaging*. Oxford University Press, 2014. Chap. 44.

[75] T.N. Wight. "A role for proteoglycans in vascular disease". In: *Matrix Biology* 71 (2018), pp. 396–420.

[76] A. Wineman. "Nonlinear viscoelastic solids—a review". In: *Mathematics and mechanics of solids* 14.3 (2009), pp. 300–366.

[77] H. Wolinsky and S. Glagov. "A lamellar unit of aortic medial structure and function in mammals". In: *Circulation research* 20.1 (1967), pp. 99–111.

[78] E. Yeung, T. Inoue, H. Matsushita, J. Opfermann, P. Mass, S. Aslan, J. Johnson, K. Nelson, B. Kim, L. Olivieri, et al. "In vivo implantation of 3-dimensional printed customized branched tissue engineered vascular graft in a porcine model". In: *The Journal of thoracic and cardiovascular surgery* 159.5 (2020), pp. 1971–1981.

[79] Z. Yosibash, I. Manor, I. Gilad, and U. Willentz. "Experimental evidence of the compressibility of arteries". In: *Journal of the mechanical behavior of biomedical materials* 39 (2014), pp. 339–354.